The effect of pressure gradient on the collapse of cavitation bubbles in normal and reduced gravity

THÈSE N^O 5674 (2013)

PRÉSENTÉE LE 1ER MARS 2013
À LA FACULTÉ DES SCIENCES ET TECHNIQUES DE L'INGÉNIEUR
LABORATOIRE DE MACHINES HYDRAULIQUES
PROGRAMME DOCTORAL EN MÉCANIQUE

ÉCOLE POLYTECHNIQUE FÉDÉRALE DE LAUSANNE

POUR L'OBTENTION DU GRADE DE DOCTEUR ÈS SCIENCES

PAR

Marc TINGUELY

acceptée sur proposition du jury:

Prof. M. Parlange, président du jury
Dr M. Farhat, directeur de thèse
Dr O. Minster, rapporteur
Prof. D. Obreschkow, rapporteur
Prof. J. R. Thome, rapporteur

EPFL

ÉCOLE POLYTECHNIQUE
FÉDÉRALE DE LAUSANNE

Suisse
2013

The most exciting phrase to hear in science, the one that heralds new discoveries, is not 'Eureka!' but 'That's funny...'

— Isaac Asimov

Remerciements

Cette thèse ne serait pas ce qu'elle est sans la contribution directe et indirecte de nombreux intervenants. Je profite de cette occasion pour leur exprimer toute ma gratitude.

Tout d'abord, je tiens à remercier sincèrement mon directeur de thèse, Dr. Mohamed Farhat, pour avoir eu suffisamment confiance en moi pour me confier un si beau sujet de thèse. Son enthousiasme contagieux pour la science en général a toujours été une grande source d'inspiration. Nos nombreuses discussions m'ont toujours poussé à aller au-delà de ce que nous connaissions déjà.

Je remercie également le directeur du Laboratoire des Machines Hydrauliques, Prof. Francois Avellan, pour m'avoir accepté dans son laboratoire, où je me suis épanoui durant ces quatre dernières années.

Ce travail n'aurait pas été possible sans le soutien financier du Fond National Suisse (FNS) pour la Recherche Scientifique (bourse No. 200020-116641). Je tiens également à remercier l'Agence Spatiale Européenne (ESA) qui nous a ouvert les portes des vols paraboliques. Ces vols m'ont permis d'obtenir de nombreux résultats originaux, présentés dans cette thèse, et publiés dans des journaux scientifiques.

Mes remerciements vont également aux membres du jury de ma thèse : Prof. Marc Parlange, Prof. John R. Thome, Dr. Olivier Minster, et Prof. Danail Obreschkow. Leurs questions et commentaires, tous intéressants, pertinents, et constructifs, ont permis l'amélioration de ce manuscrit.

Dans le cadre de ma thèse, j'ai eu la chance de pouvoir collaborer, quelques semaines par année, avec deux professeurs externes à l'EPFL. Ce fut un honneur de côtoyer chaque été, pendant une dizaine de jours, le Prof. John E. Field de l'Université de Cambridge, en Angleterre, sur l'apparition de cavitation dans un jet impacté à haute vitesse. Chaque automne, je me réjouissais de la visite du Prof. Sato de l'Université de Tohoku, au Japon, avec lequel nous étudions la formation d'hydrogène lors de la génération et du collapse de bulle de cavitation. J'ai appris énormément grâce à ces collaborations, qui ont d'ailleurs chacune abouti à la publication d'un papier dont je fus co-auteur.

Remerciements

Un moment important de ma thèse fut mon intégration à l'équipe Flash & Splash, composée de Danail Obreschkow, Philippe Kobel, Nicolas Dorsaz et Aurèle de Bosset. Les "flasheurs" avaient déjà effectués des vols paraboliques, et c'est donc avec cette équipe que s'organisèrent les deux campagnes de vols auxquelles j'ai participé. Les moments partagés à travailler le week-end au LMH, et surtout les semaines passées ensemble à Bordeaux sont des souvenirs inoubliables. Je remercie chacun d'eux non seulement pour leur contribution inestimable à cette thèse, mais surtout pour leur accueil chaleureux dans l'équipe, et pour la merveilleuse expérience que nous avons partagée.

Les dispositifs expérimentaux présentées dans cette thèse n'auraient jamais vu le jour sans le travail des mécaniciens du LMH. Sans Louis, Maxime, Raymond, Jean-Daniel, Victor, Mattias, Christian et David, les idées farfelues des doctorants ne peuvent pas devenir réalité. Leur travail acharné pour nous aider à construire l'expérience pour l'avion, en moins de quatre mois, fut tout simplement incroyable, et je les en remercie très sincèrement.

La raison principale pour laquelle ces années au LMH furent si agréables (sans tenir compte de la beauté du sujet scientifique que je traitais, évidemment) est l'ambiance parmi les doctorants du laboratoire. Pour la plupart d'entre nous, nous sommes devenus plus que des collègues, des amis. Je remercie tout d'abords les personnes avec qui j'ai paisiblement partagé mon bureau durant la plus grande partie de ma thèse: Amir Zobeiri et Francisco Botero. Nos petites pauses café et biscuits en milieu d'après-midi furent toujours un moment de détente bienvenu. Cette thèse n'aurait pas pu aboutir sans les fameux "working dinner" du mois de novembre. Un grand merci donc à Andres Mueller, avec qui je mangeais au LMH presque tous les soirs, lui écrivant un papier et moi ma thèses. Plusieurs de mes collègues doctorant furent tout d'abord mes collègues de classe à l'EPFL. Pour tous les bons moments (et raclettes du jeudi soir en salle de travail) partagés depuis toutes ces années, je remercie Steven Roth, Olivier Pacot et Martino Reclari. Merci également à Matthieu Dreyer, avec qui nous défendons les couleurs de Fribourg au LMH, et nous ressourcons les week-ends dans notre ville natale. Un grand merci (et bon courage pour la fin de thèse) à tous les autres actuels doctorants : Christian Vessaz, Christian Landry, Ebrahim Jahanbakhsh, Arthur Favrel, Julien Monge, et (post-doc) Pierre Bouillot. Je remercie également les anciens doctorants et post-doc qui ont tous à leur manière influencé mon approche de ce que c'est que faire une thèse : Vlad Hasmatuchi, Sebastien Alligné, Nicolas Ruchonnet, Stefan Berten, Philippe Ausoni, Olivier Braun, Ali Zobeiri, Cécile Muench, et Christophe Nicolet.

Je souhaite également remercier tous les collaborateurs du LMH. Tout d'abord Isabelle Stoudmann, pour le travail administratif inestimable qu'elle effectue au laboratoire. Merci au bureau d'étude pour m'avoir dépanné avec quelques plans du tunnel de cavitation, et quelques impressions de poster, et en particulier à Philippe Cerrutti pour tous les dépannages informatiques. Je remercie également les ingénieurs des plateformes d'essai, qui m'ont toujours gentiment accueilli lorsque j'étais à la recherche de thermomètres ou autres instruments qu'ils

pourraient éventuellement me prêter.

Je profite également de cette occasion pour remercie chaleureusement ma famille. Merci à mes parents qui m'ont poussé et soutenu durant mes études, et qui surtout m'ont donné l'éducation qui m'a permis d'en être là aujourd'hui. Les repas du dimanche soir en famille avec ma sœur et mon frère ont toujours été un petit moment de tranquillité et de joie, surtout durant les périodes difficiles de la thèse.

Je remercie également mes amis de Fribourg, grâce à qui je m'échappais des tracas de la thèse. C'est toujours un plaisir de revoir Marc, Philippe, Lionel, Julien, Freddy, Thierry, Claire, Christelle, Sandra et Joëlle, et de réaliser le bout de chemin qu'on a fait depuis l'adolescence. Je remercie également mon colocataire de longue date, Olivier Kneuss, pour les huit (!) paisibles années passé dans notre appartement d'Ecublens.

Finalement, je tiens à remercie Sara. Sans elle, je n'aurais probablement pas envisagé faire une thèse. J'ai toujours été impressionné par la quantité, et surtout la qualité du travail qu'elle abattait durant sa propre thèse. Sara fut une source d'inspiration, mais surtout un soutien sans équivalant durant ma thèse. Pour cela, et pour tout ce qu'on partage, merci.

Marc Tinguely

Abstract

When water flows through hydraulic turbomachines, the local pressure can become low enough to vaporize the water and create vapor cavities. This phenomenon is called cavitation. When the cavities collapse, shock waves and liquid jets traveling through the inclusions can erode nearby solid surfaces. The collapse of cavitation bubbles has been extensively investigated in the case of a single bubble in a liquid at rest. However, in the case of hydraulic machines, the bubbles collapse in a flowing liquid subject to strong pressure gradients. The objective of this thesis is thus to investigate the effect of the pressure gradient on the collapse of a spherical cavitation bubble.

We have performed a preliminary investigation of bubble dynamics in a flowing liquid with a pressure gradient. To this end, we have placed a Naca0009 hydrofoil in the test section of EPFL High Speed Cavitation Tunnel and used a high energy pulsed laser focusing technique to generate a single vapor bubble close to the hydrofoil's leading edge. We have observed a significant influence of the pressure gradient on the bubble dynamics. Particularly, if the collapse phase occurs near the minimum pressure point, the microjet is no more directed towards the solid surface but towards the lower pressure zone in the stream wise direction. We have also observed a peculiar feature of a cluster of bubble dynamics, which behaves almost similar to a single bubble, exhibiting a microjet during its collapse. These unprecedented results are of major importance for a better understanding of the cavitation erosion mechanism in hydraulic systems.

The qualitative results obtained in the cavitation tunnel led to the investigation of the effect of a constant pressure gradient on the collapse of the bubble. An experimental setup is built to observe the dynamics of the bubble in water, subject to the gravity induced hydrostatic pressure gradient, and to measure the pressure fluctuation due to the shock waves. The bubbles are generated with a high energy pulsed laser and recorded with a high speed camera. The experimental setup is taken onboard parabolic flights. The parabolic manoeuvres allow the gravity level to be varied in the plane, which modulates the intensity of the pressure gradient in the liquid. The high speed movies taken during the flights reveal that vapor jets appear with the rebound bubble. An empirical law for the prediction of the volume of the jet is deducted from the experimental results. The volume of the jet, normalized with the volume of the rebound bubble, is found to be proportional to a non dimensional parameter $\zeta = |\nabla p| R_{max} / \Delta p$, where ∇p is the pressure gradient, R_{max} is the maximal bubble radius and Δp is the driving pressure. This dependance is enforced by a theoretical development based on the concept of the Kelvin impulse. Moreover, we identify a threshold for the apparition of

Abstract

the vapor jet: $\zeta > 4 \cdot 10^{-4}$.

A new approach for the study of the bubble collapse is proposed: we look at how the energy in the initial cavitation bubble is partitioned between the collapse channels, namely the rebound, the shock wave, the jet, and the luminescence. The microgravity phases of the parabolic flights prevent the apparition of the jet. The collapse of the bubble, in this case, is perfectly spherically symmetric. Moreover, the energy dissipated through luminescence is negligible. Therefore, the study reduces to the energy partition between rebound and shock wave. The measurements uncover a systematic pressure dependence of the energy partition between rebound and shock. We demonstrate that these observations agree with a physical model relying on a first-order approximation of the liquid compressibility and an adiabatic treatment of the non-condensable gas inside the bubble. Using this model, we find that the energy partition between rebound and shock is dictated by a single non-dimensional parameter $\xi = \Delta p \gamma^6 / p_{g0}^{1/\gamma} (\rho c^2)^{1-1/\gamma}$, where γ is the adiabatic index of the non-condensable gas, p_{g0} is the pressure of the non-condensable gas at the maximal bubble radius, ρ is the liquid density, and c is the speed of sound in the liquid.

Keywords

Cavitation, bubble, collapse, pressure gradient, microjet, shock wave, luminescence, energy partition, bubble gas content.

Résumé

Dans les turbomachines hydrauliques, la pression locale dans le liquide peut s'abaisser à un tel point que l'eau se vaporise. Ce phénomène est appelé la cavitation. Lorsque ces cavités de vapeur implosent proche d'une surface solide, on peut observer la formation d'un jet de liquide dirigé vers la paroi, ainsi que la formation d'une onde de choc. L'implosion de la bulle a été largement étudiée dans le cas d'une bulle générée dans un liquide au repos. Cependant, dans le cas des machines hydrauliques, les bulles implosent dans un liquide soumis à de forts gradients de pression. L'objectif de cette thèse est d'étudier l'effet du gradient de pression sur l'implosion d'une bulle de cavitation sphérique.

Nous avons tout d'abord observé le cas d'une bulle soumise à un gradient de pression dans un écoulement. Une bulle est créée par focalisation d'un laser pulsé de forte énergie dans le liquide, proche d'un profil placé dans la veine d'essai du tunnel de cavitation de l'EPFL. L'écoulement autour du profil est représentatif de celui que l'on trouve dans une turbomachine hydraulique. Le gradient de pression affecte de manière significative l'implosion de la bulle. En effet, on observe notamment la formation lors de l'implosion d'un microjet, dont la direction est opposée à celle du gradient de pression.

Les résultats qualitatifs obtenus dans le tunnel de cavitation nous ont poussés à étudier l'effet d'un gradient de pression constant sur l'implosion de la bulle. Un dispositif expérimental a été construit afin d'observer la dynamique de la bulle dans de l'eau soumise à un gradient de pression hydrostatique, et de mesurer les fluctuations de pression liées au passage des ondes de choc. Les bulles ont été créées par focalisation d'un laser pulsé de forte énergie, et l'évolution de la bulle est enregistrée au moyen d'une caméra rapide. Le dispositif expérimental a été mis à bord d'un avion pour des vols paraboliques. Ces manœuvres aériennes permettent de faire varier le niveau de gravité à bord de l'avion, ce qui fait donc varier l'intensité du gradient de pression dans le liquide. Grâce à ces essais, nous avons observé l'apparition d'un microjet lors du rebond de la bulle. Nous en avons tiré une loi empirique qui permet de prédire le volume du jet en fonction des conditions expérimentales. Le volume du jet, normalisé par le volume du rebond, est proportionnel à un paramètre adimensionnel $\zeta = |\nabla p| R_{max} / \Delta p$, où ∇p est le gradient de pression, R_{max} est le rayon maximal de la bulle et Δp est la différence de pression entre l'intérieur et l'extérieur de la bulle. Finalement, le paramètre adimensionnel est validé par un développement théorique basé sur le concept de l'impulsion de Kelvin. De plus, nous avons identifié un seuil pour l'apparition du microjet : $\zeta > 4 \cdot 10^{-4}$.

Nous proposons une nouvelle approche pour l'étude de l'implosion de la bulle : On évalue comment l'énergie se trouvant initialement dans la bulle se partage lors de l'implosion entre

Abstract

les différents canaux que sont le rebond, l'onde de choc, le jet et la luminescence. Les résultats obtenus lors des phases de microgravité durant les vols paraboliques nous permettent d'étudier le cas d'un collapse parfaitement sphérique. En effet, les jets ne se forment pas en microgravité. De plus, l'énergie dissipée par la luminescence est si faible que l'on peut la négliger. Notre cas d'étude se réduit alors à la répartition de l'énergie de la bulle entre le rebond et l'onde de choc. Nos mesures nous ont permis de découvrir une dépendance de la répartition d'énergie à la pression dans le liquide. Ces résultats sont confirmés par un modèle physique basé sur une approximation de premier ordre de la compressibilité du liquide, et d'un traitement adiabatique du gaz se trouvant dans la bulle. Au moyen de ce modèle, nous développons un paramètre adimensionnel ξ qui permet de prédire la répartition de l'énergie à l'implosion. Le paramètre adimensionnel est défini comme $\xi = \Delta p \gamma^6 / p_{g0}{}^{1/\gamma} (\rho c^2)^{1-1/\gamma}$, où γ est l'indice adiabatique du gaz non-condensable, p_{g0} est la pression du gaz non-condensable lorsque le rayon de la bulle est à son maximum, ρ est la masse volumique du liquide, et c est la vitesse du son dans le liquide.

Mots-clés

Cavitation, bulle, implosion, gradient de pression, microjet, onde de choc, luminescence, répartition de l'énergie, composition du gaz dans la bulle.

Contents

Contents

List of Figures

1 Introduction

1.1 About cavitation

Cavitation is the phase change process through which vapor cavities form inside an initially homogeneous liquid when the pressure decreases [1, 2, 3]. Analogous to when water turns into vapor when the temperature reaches the boiling point, water turns into vapor when the pressure decreases below its vapor pressure (see water phase diagram in Fig. 1.1). The nucleation, i.e., the formation of the bubbles, is however quite complex, which makes cavitation a subtle process. Indeed, pure water is able to sustain pressure below the vapor pressure, and even tensile stress before the intermolecular bounds break, leading to the formation of cavities. In practice, the presence of impurities in the liquid, such as microscopic gas bubbles or solid particles, can create weak points in the liquid, where the gas cavities grow once the vapor pressure is reached. These impurities are called cavitation nuclei. The nuclei can have several origins, mainly from gas dissolved in the liquid, or gas trapped in small surface roughness. In flowing liquids cavitation occurs when the local pressure in the liquid becomes smaller than the vapor pressure, and activates the growth of the nuclei. The pressure decrease could be induced by the geometry of the boundaries around the liquid, by roughness on the boundary surfaces, or even by shear stresses. Cavitation occuring in a flowing liquid is called hydrodynamic cavitation, and can take several forms, commonly divided into three groups [2, 3]:

- Attached cavitation: A cavity or a vapor pocket that is attached to a solid boundary in the flow.
- Vortex cavitation: Cavitation that occurs at the core of a vortex.
- Transient cavitation bubbles: An isolated cavitation bubble that appears in a low pressure region and is carried away by the flow.
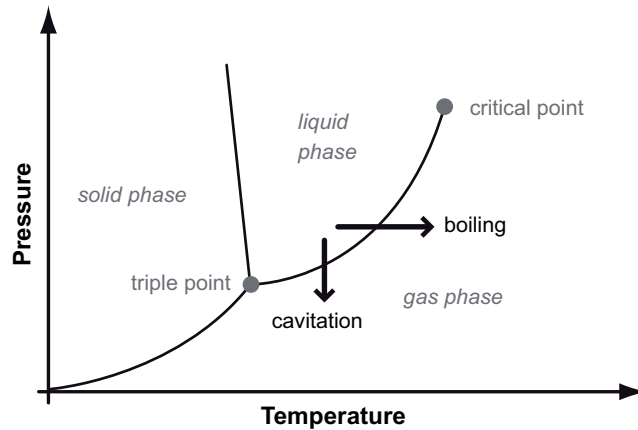
Figure 1.1: Sketch of the water phase diagram. Boiling is the phase change from liquid to gas by temperature increase, whereas cavitation is the phase change by pressure decrease.

Historically, experimental interest in cavitation arose in 1912 when Silberrad reported erosion due to cavitation on the propeller of large cruise boats [4]. The cavitation occurred on the blades of the propeller, due to low pressure zones generated by the high rotation speed. The same phenomenon occurs in hydraulic turbomachines. Low pressure zones are generated by the flow over the blades. If the local pressure is lower than the vapor pressure, cavitation develops on the blade. The hydraulic machines are not designed to operate with cavitation, which significantly modifies the flow. Therefore, cavitation can lead to a dramatic drop in performance. In addition to erosion, cavitation can also lead to vibrations and subsequent structural damages to the point where the turbine needs to be repaired or replaced. Since large hydraulic turbines can generate hundreds of megawatts of electricity, unexpected damages and early replacement of the equipment can result in huge economic costs.

Cavitation is not only restricted to water, but can occur in various fluids. In rocket engines, the liquid fuel and oxidizers are pumped by the inducers and injected into the combustion chamber. The inducers are designed to sustain cavitation erosion for the few minutes necessary to launch the spacecraft [5]. In artificial hearts, cavitation can not only damage the mechanical valves, but it can also critically alter the blood of the patient [6].

Despite a century of research, cavitation is still a major issue in various domains. At this point, efforts have been placed on preventing the initiation of cavitation, and, when cavitation cannot be avoided, minimizing the damages. However, effective prevention measures necessitate a good understanding of the fundamental physical phenomena involved in cavitation. This understanding has been notably sought by investigating the simplest form of cavitation, the single bubble.

Experimental methods have been developed to generate one single vapor bubble on demand, growing and eventually collapsing in a liquid at rest. These single bubbles can be generated by several means, most of them not implying a local pressure drop in the liquid. Nuclei can be excited by acoustic pressure waves, to the point where the bubble grows several times their initial volume. Energy deposition methods have been widely used to generate an explosively growing vapor bubble by local heating of the liquid. The bubble is obtained by focussing a laser, by an electrical discharge, or even by an explosion in water. The rise of high speed imaging contributed largely to the investigation of the dynamics of the bubble, because the lifetime of the cavitation bubble is so short that conventional recording methods do not allow the phenomena to be captured. With high speed imaging, it becomes possible to observe peculiar phenomena such as the formation of microjets at the collapse, or the propagation of shock waves in the liquid.

In parallel with experiments, theoretical models of the collapse of spherical cavitation bubbles have been developed. The first model, still widely used, is the Rayleigh equation [7]. This model describes the collapse of a perfectly spherical empty cavity in a uniform liquid. It was later improved by Plesset [8], to take into account surface tension, viscosity, and gas inside the bubble, resulting in the so-called Rayleigh-Plesset model. Later, this model was further developed to account for more physical aspects, such as the compressibility of the liquid [9, 10, 11, 12], or the chemical reactions occurring at the collapse [13, 14, 15]. Non-spherical collapses have to be treated differently, using numerical simulations such as the boundary integral method [16, 17].

Nowadays, cavitation is not only associated with erosion issues. It is increasingly considered for "beneficial" uses. Cavitation bubbles are now exploited as tools in surgery [18] and medical applications [19], microchip cleaning [20], water treatment [21], and microfluidics [22, 23]. However, even in the most simple form of cavitation, a thorough description of the physical processes is still lacking.

1.2 Goal and organization of the thesis

To date, most studies on collapsing cavitation bubbles have considered a bubble in a liquid at rest, with a uniform pressure field around the bubble. The characteristic features of the bubble collapse, namely the rebound, the formation of jets, the generation of shock waves, and the luminescence have been assiduously investigated. However, in the field of hydraulic machines, the cavitation bubbles occur in a flowing liquid, subject to strong pressure gradients. A few studies have already observed a non-negligible influence of a pressure gradient on the dynamics of the collapse of the cavitation bubble, in the form of the apparition of a jet at the rebound [24, 25]. But no systematic study of the effect of a pressure gradient on the different collapse channels has ever been conducted.

The goal of this thesis is to investigate the effect of the pressure gradient on the collapse of a spherical cavitation bubble.

To address this question, the work has been organized as follows.

We start with an introduction on single cavitation bubbles (Ch. 2). We describe the phenomena associated with the collapse of the bubble, and we detail different theoretical models. The methods for generating on demand single cavitation bubbles are also discussed.

The case of bubbles generated within a flow with a pressure gradient is first treated (Ch. 3). The pressure gradient is developed by putting a hydrofoil in the flow. The experimental conditions reproduce those typically found in hydraulic turbomachines. The bubble is generated with a high energy laser at different locations in the pressure field, in order to test the effect of the pressure gradient. Qualitative conclusions are drawn from the observations.

An experimental setup dedicated to the observation of single spherical cavitation bubbles is built (Ch. 4). The setup is designed to study the effect of the hydrostatic pressure gradient on the collapse of the bubbles. The setup is not only used in the laboratory, but also onboard an aircraft performing parabolic flights. During the parabolic flights, the gravity level experienced in the aircraft changes due to specific flight manoeuvres, as a result, the intensity of the hydrostatic pressure gradient in the liquid changes.

With the data obtained during the parabolic flights, the effect of the hydrostatic pressure gradient on the jetting phenomenon is investigated (Ch. 5). A parametric study leads to a scaling law for the volume of the jet as a function of the involved experimental parameters. The phenomenologic law is supported by an analytic treatment of the problem.

Lastly, the effect of the pressure gradient on the rebound, the shock and, to a lesser extent, the luminescence is investigated (Ch. 6). Unlike previous studies that examined each phenomenon individually, we adopt a global approach, which consists of studying all collapse channels at the same time. We first investigate how the energy of the initial bubble is partitioned between the different collapse channels in a perfectly spherical case. The partition and the major driving parameters are identified and discussed. Then, we look at how this partition varies when we apply a constant hydrostatic pressure gradient in the liquid.

2 An introduction to single cavitation bubbles

2.1 Phenomena occurring at the collapse of a single cavitation bubble

Regardless of how and where a cavitation bubble occurs, the bubble is bound to grow and eventually collapse. The collapse of the bubble is of particular interest, because of several peculiar phenomena that take place in a very short period of time. These phenomena, which we refer to as the collapse channels, are listed below. and illustrated in Fig. 2.1.

- **Rebound :** The collapse is followed by the reappearance of the rebound bubble, growing and collapsing several times again.
- **jet :** An asymmetrical collapse of the bubble can lead to the formation of a jet at the very last stage of the collapse, visible with the rebound bubble.
- **shock wave :** A shock wave is released at the last stage of the collapse of the bubble.
- **luminescence :** The gas inside the bubble at the collapse is compressed, and the temperature rise to a state where light is emitted. This phenomenon is called the luminescence.
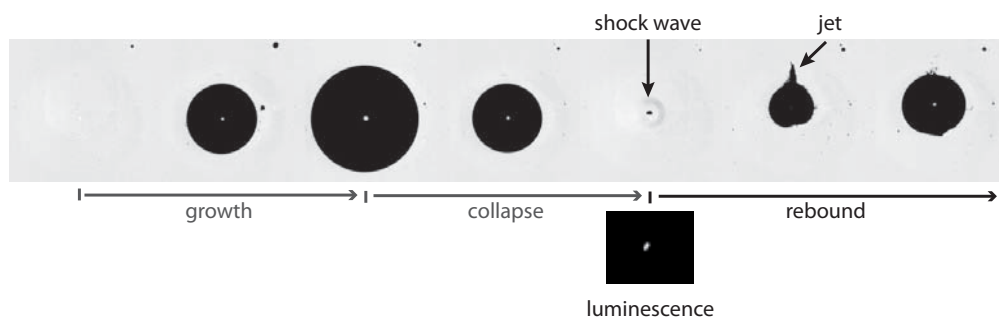
Figure 2.1: High speed images of a cavitation bubble growing, collapsing, and rebounding. The four collapse channels, namely the rebound, the jet, the shock wave and the luminescence are illustrated.

Each of these phenomena and their implications are described in the following paragraphs. The fundamental theoretical models for the dynamics of the collapse are then detailed in the next section, while the chapter ends with a discussion on the methods for the generation of single cavitation bubbles.

Rebound

After the collapse, the bubble reappears in the form of a rebound bubble of smaller size. The rebound is due to gas trapped in the bubble at the collapse. The cavitation bubbles are filled with a mixture of vapor and non-condensable gas. The origin of this gas is still unclear, but it is thought that it comes from a combination of gas dissolved in the water, and gas created at the generation for the energy deposition bubbles [26, 27]. At the very last stage of the collapse, the bubble interface moves fast towards the center of the bubble. Both non-condensable gas and vapor in the bubble are compressed, and the pressure in the bubble rises (can reach 1 GPa [2, 28]). Due to this high pressure in the bubble, the contraction of the bubble eventually slows down and stops, and the bubble starts to rebound. The quantity of non-condensable gas in the bubble influences the maximum radius of the rebound bubble. It has been demonstrated that a larger concentration of non-condensable gas leads to a larger volume of the rebound bubble [26, 29].

The shape of the rebound bubble is determined by the symmetry or asymmetry of the dynamics of the collapse. A perfectly spherical collapse produces a spherical rebound bubble. However, an asymmetry leads to the deformation of the bubble and, in some cases, the apparition of a jet emerging from the rebound bubble. The rebound bubble can also sometimes break into several bubbles. This phenomenon is called fission of the bubble. It is thought to be cause by either Rayleigh-Taylor instabilities on the bubble interface or by the re-entrant jet at the collapse of the bubble [30]. It has also been shown that when bubble fission occurs the resulting rebound bubble is smaller than expected because the process dissipates energy [31].

Jets

When the collapse of a cavitation bubble is not spherically symmetric, one side of the bubble will eventually reach the center of the bubble first at the very last stage of the collapse. On this side of the bubble, the liquid is advancing faster into the bubble than on the other location on the interface. Because of its characteristic shape, this advancing portion of liquid is called the microjet. The microjet can pierce the bubble, and go through the diametrally opposite interface of the bubble. This traversing flow entrains some vapor into the liquid, and a vapor jet grows outwards from the rebound bubble.

The presence of a solid boundary close to a collapsing bubble creates an asymmetry. The interface close to the solid surface tends to flatten, while the interface diametrally opposite moves fast towards the center of the bubble, creating the microjet. The microjet can reach

velocities of 100 m/s [32]. If the bubble is close enough to the surface, the microjet hits the solid surface. Because of the high velocity of the microjet, it is often considered as a potential source of cavitation erosion. The characteristics of the microjet are closely related to the standoff parameter, which is the ratio between the bubble radius and the distance between the bubble center and the wall [32, 33]. The shape of the solid surface also plays an important role in the jetting mechanisms. A convex solid surface tends to increase the velocity of the microjet [34].

When a bubble collapses close to a free surface, a microjet also appears. However, unlike for the solid surface, the microjet is in this case directed opposite to the surface. The velocity of the microjet is of the order of 100 m/s [35]. In addition to the microjet, a counterjet appears on the free surface after the collapse of the bubble. A column of liquid rises with velocities of 10 to 30 m/s [36, 37, 38]. The velocities and width of both the microjet and the counterjet are also influenced by the standoff parameter. The effect of the curvature of the free surface has also been investigated. Cavitation bubbles have been generated within cylindrical liquid jets [38] and in spherical drops [37]. The curvature changes the shape of the crown appearing around the counterjet. The increase of the curvature also broadens the counterjet.

A multitude of variations and combinations of these two basic case studies have been investigated. We can cite the case of a bubble between two solid surfaces, or a solid and a free surface [39, 35]. Moreover, cases of bubble collapsing close to elastic surfaces have also been carefully investigated [40]. Approaching boundaries to the bubble is not the only way to cause asymmetry in the collapse. When a bubble collapses in a liquid subject to a pressure gradient, the bubble symmetry is also broken. Observations of bubble traveling in the flow through a venturi tube have been reported [25]. The shape of the collapsing bubbles denotes the formation of a microjet. It has also been reported that the hydrostatic pressure gradient can also induce the apparition of the jets [24, 41].

Shock waves

During the collapse phase, the high velocity of the bubble interface and the compressibility of the liquid lead to the generation of shock waves into the water. The pressure peak can reach values of the order of 1 GPa, which is high enough to damage solid material located near the bubble. The shock waves are therefore considered, along with the microjet impinging the surface, as a mechanism causing the erosion at the bubble collapse. The fluctuation of pressure, when the shock propagates through the liquid, can excite nuclei [37]. It can even make bubbles collapse, which has been used to observe the formation of microjet within bubbles [42, 43, 19]. Depending on the shape of the boundaries around the bubble, the reflections of the shock waves can focus and generate secondary cavitation in the liquid [37, 38, 44, 45]. Note that when a cavitation bubble is generated by energy deposition, the explosive growth of the bubble generates a first shock wave, with a pressure peak amplitude of 1-10 GPa [46].

Luminescence

At the very last stage of the collapse, the pressure and temperature of the gas inside the bubble are so high that light is emitted. This phenomenon of light emission is known as luminescence. The contraction of the bubble at the collapse is so violent that the gas within the bubble is compressed to pressure as high as 1GPa [28]. The duration of high compression ($> 10^3 \times$ initial pressure) is so short (order of 1 ns) that the process can be considered as adiabatic. The temperature in the bubble increases dramatically. The maximum temperature is estimated at 5,000 to 15,000 K. By comparison, the surface of the sun is 5,778 K. The gas is so hot that it radiates light. The chemical species constituting the gas inside the bubble plays an important role in luminescence. For instance, luminescence can be "boosted" by the adjunction of inert gas within the bubble. The temperature reached is higher than for other gases, and the light emitted is more intense. Investigations have shown that asymmetry at the bubble collapse can decrease the intensity of the light emitted [47, 48, 49, 50]. This denotes a close relation between the "symmetry" of the compression motion and the temperature reached by the gas in the bubble. However, luminescence can still occur in highly non-spherical cavitation collapse, like in the case of attached cavitation [51]. Note that the high pressure and temperature reached within the bubble enhances chemical reactions within the trapped gas, and even allows reactions that could otherwise not occur [13, 14].

2.2   Theoretical models

In 1847, when George Stokes challenged his students to calculate the motion of an empty spherical cavity in water, he was not aware that he had just set down the equation that would become the most used in cavitation modeling. Indeed, in 1917, Lord Rayleigh modeled the collapse of cavitation bubbles as the motion of an empty spherical cavity in an infinite volume of water. This equation, nowadays known as the Rayleigh equation, reads

$$R\ddot{R} + \frac{3}{2}\dot{R}^2 = -\frac{p_\infty}{\rho},$$

(2.1)

where R is the radius of the spherical cavity as a function of time, p_∞ is the pressure in the water, and ρ is the density of water (997 kg / m^3 at 25 °C). Using this simple model, one assumes that:

- the motion is spherically symmetric
- the bubble is empty
- the bubble is located in an infinite volume of water
- the water is incompressible and irrotational
- gravity, surface tension, viscosity, and heat or mass transfer is neglected

In 1954, the Rayleigh equation is adapted by Plesset to model the more general case of the evolution of a spherical bubble in a viscous and incompressible liquid. The main assumptions are [7, 2]

- the liquid is incompressible, and either Newtonian or inviscid
- gravity is neglected
- the air content inside the bubble is constant, its inertia is neglected and no heat is transferred to the surroundings (i.e. adiabatic assumption)
- the bubble is saturated with vapor, whose partial pressure is the vapor pressure at the temperature of the liquid.

The resulting equation, known as the Rayleigh-Plesset equation, allows to determine the radius of the bubble, and the pressure in the bubble and around the bubble as a function of time. It reads

$$\rho \left[R\ddot{R} + \frac{3}{2}\dot{R}^2 \right] = p_v - p_\infty + p_{g0} \left(\frac{R_0}{R} \right)^{3\gamma} - \frac{2S}{R} - 4\mu \frac{\dot{R}}{R}, \tag{2.2}$$

where p_v is the vapor pressure of water, p_{g0} is the initial partial pressure of the non-condensable gas in the bubble, R_0 is the initial radius of the bubble, γ is the adiabatic index of the non-condensable gas inside the bubble (1.3 for air), S is the surface tension of water ($7.2 \cdot 10^{-2}$ N/m at 25 °C), and μ is the kinematic viscosity of water ($9 \cdot 10^{-7}$ N/m at 25 °C).

Surface tension and viscosity are found to play a negligible role in the collapse of cavitation bubbles [1, 2, 52], and are therefore often neglected. If we monitor each term Eq. 2.2 during the collapse of a bubble, we observe that the inertial terms (left hand side terms) and the pressure terms (first three terms of right hand side) dominate over the terms of surface tension and viscosity (fourth and fifth term of right hand side respectively). Note that this observation if valid for millimetric bubbles in water, which is what we consider in this thesis. For bubbles with a radius of the order of the micrometer, the effect of surface tension is not negligible anymore [2], whereas for bubbles in a very viscous fluid (more than thousands of time the viscosity of water), the viscosity would slow down the collapse process.

Authors have proposed different generalizations of the Rayleigh-Plesset equation to a compressible liquid [9, 10, 11, 12]. In 1987, Prosperetti and Lezzi [53, 54] showed that several of the equations can be derived from a unique one-parameter family of equations, called the general Keller-Herring equation [12]:

$$\left[1 - (\lambda + 1)\frac{\dot{R}}{c} \right] R\ddot{R} + \frac{3}{2} \left[1 - \frac{1}{3}(3\lambda + 1)\frac{\dot{R}}{c} \right] \dot{R}^2$$

$$= \frac{1}{\rho} \left(1 - (\lambda - 1)\frac{\dot{R}}{c} + \frac{R}{c}\frac{d}{dt} \right) (p_B - p_\infty) + O(c^{-2}) \tag{2.3}$$

where c is the speed of sound, p_B is the pressure inside the bubble, λ is an arbitrary parameter, and O denotes the order of the error. Note that, in the following work, we will use the formulation with $\lambda = 0$, which corresponds to the equation derived by Keller and Miksis [11].

The three models for the bubble collapse presented here have been further improved. Evaporation, condensation, and mass transfer can be taken into account [26]. The gas inside the bubble can be considered as a van der Waals gas rather than ideal gas [26]. It is also possible to model the chemical reactions occurring at the collapses of an oscillating bubble, and thus to monitor the evolution of gas concentration within the bubble [15]. However, all these models have been developed for the calculation of spherical collapses, even though, as already mentioned, the bubbles do not always collapse spherically. Benjamin and Ellis [24] were the first to realize that the concept of the Kelvin impulse could give a good insight of the dynamics of a non-spherical bubble collapse. The Kelvin impulse corresponds to the apparent inertia of the collapsing bubble, and can be used to determine the general motion of the bubble [55]. Precise prediction of the dynamics of a non-spherical bubble collapse can be achieved by numerical simulations, using methods such as the boundary integral method [16, 17].

2.3 Differences between "on demand" cavitation bubbles and hydrodynamic cavitation bubbles

Predicting accurately where and when a single cavitation bubble will occur in a flowing liquid is a difficult task. Moreover, the unsteady and short lived nature (could be $\ll$ 1ms) of the bubbles makes it difficult to observe. Therefore, experimental techniques have been developed in order to generate "on demand" one single cavitation bubble at a given time and location in a liquid. The "flaw" of these methods is that the bubbles are not generated by pressure drop in a flow, as for hydrodynamic cavitation, but by either a tension applied on the liquid or by local energy deposition, which leads to the rupture of the liquid and the formation of a cavity of vapor. By extension, these bubbles are also called cavitation bubbles. The main methods for generating bubbles are the following:

- **Acoustic cavitation**: Sound waves propagating into the liquid produce a tension that makes the nuclei grow, leading to the apparition of a bubble.
- **Laser-induced bubble**: A laser pulse is focussed into the water. At the focussing point, the water turns into a hot plasma. This phenomenon is called water breakdown. Eventually, the plasma turns into an expanding vapor bubble.
- **Spark bubble**: Two electrodes are placed into the water. An electric discharge between the electrodes creates a small plasma which, as for the laser method, eventually turns into a vapor bubble.

The acoustic method excites the bubble over several oscillation cycles. It is often used in the investigation of cavitation enhanced chemistry [56, 13, 14] or luminescence [57], where

the successive collapses help the observation. However, the energy deposition methods have the advantage to generate a single bubble that collapses under the sole influence of the pressure in the liquid, since the rebound is not affected by pressure waves traveling through the liquid. In addition, the prediction of the position of the generation of the bubble is also more precise than with the acoustic method. The acoustic bubble grows from a nuclei in the liquid, while with the energy deposition method, the bubble grows where the energy is focussed or released. Because of those advantages, the energy deposition methods are more adapted to the identification of the effect of a pressure gradient on the collapse of a single cavitation bubble, which is what we intend to do in this thesis.

The two main methods for the generation of cavitation bubble with energy deposition in a liquid are the spark method and the laser method. Figure 2.2 provides a sketch of how both bubble are generated, along with an image of a bubble at maximum radius generated with each method. The bubble is generated from a hot plasma created in the water. Due to the high pressure and temperature within the plasma, a vaporization of the liquid take place, and the bubble grows explosively. In the first instant of the bubble generation, the supersonic velocity of the interface and the large pressure inside the plasma creates a shock wave propagating in the liquid. The bubble grows and reaches a maximum radius. At this moment, the pressure in the surrounding liquid is larger than the pressure within the bubble (which is equal to the vapor pressure) and the bubble starts to collapse. The bubble interface accelerates radially towards the center of the bubble. The gas inside the bubble is compressed until the bubble reaches a minimum radius. At this moment, the pressure and the temperature of the gas inside the bubble are high, leading to emission of light, called luminescence. Due to the high pressure and temperature, a rebound bubble grows explosively. The supersonic interface velocity and the high pressure in the bubble generate a shock wave. The collapse-rebound cycle occurs again several times, until all potential energy of the bubble is dissipated, mainly through the shock waves.

The difference between the spark and the laser method lies in how the plasma is generated. In the spark method, the plasma is generated by an electric discharge between two electrodes. In the laser method, the plasma is generated with a high energy laser pulse focussed into the liquid. The phenomenon is called the water breakdown. The plasma occurs where the energy density of the laser beam is larger than the ionization threshold [38]. The main advantage of the laser compared to the spark is that the laser method is non-intrusive. The laser can be focussed from an optical system placed outside of the test chamber. Although it requires an optical access to the liquid, i.e. a transparent window, nothing is placed into the test chamber. In the case of the spark method, the electrodes are located within the liquid. The bubble forms at the tip of the electrodes. An interaction between the bubble and the electrodes cannot be avoided. For this reason, we decided to use the laser method for the generation of cavitation bubbles.
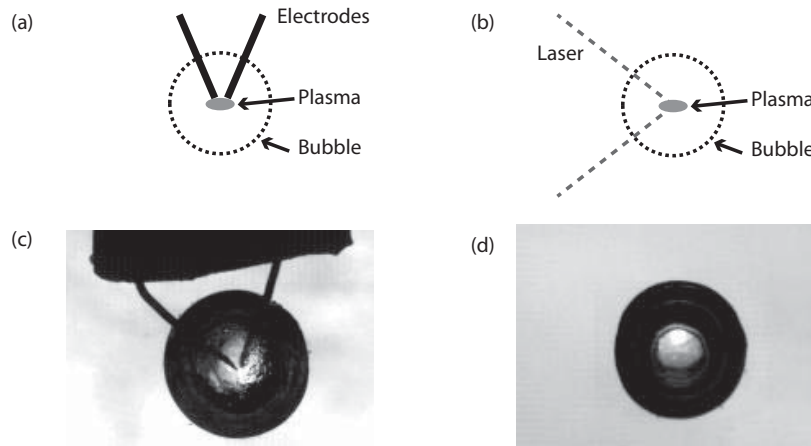
Figure 2.2: Sketch of the generation of a bubble with (a) an electrical spark discharge, and (b) a focussed laser pulse, along with an image of the bubble at maximum radius generated with (c) the spark, and (d) the laser.

One can reasonably wonder if the cavitation bubbles generated by energy deposition are similar to the hydrodynamic cavitation bubbles, i.e. bubbles generated by pressure decrease in the liquid. One way to evaluate it is to compare the dynamics of the collapse with a well-established and reliable theoretical model: the Rayleigh-Plesset model. This model allows to calculate accurately the evolution in time of the radius of a collapsing bubble, and has been proven to be an accurate model of the collapse of hydrodynamic cavitation bubbles. The normalized radius $R^* = R/R_{max}$, calculated with the Rayleigh-Plesset equation, is plot as a function of the normalized time $t^* = t/\tau_c$ in Fig. 2.3. R is the radius of the bubble as a function of time t, R_{max} is the maximum radius, and τ_c is the collapse time of the bubble. The points on the graph are experimental data of R^* as a function of t^*. We plot the values from one spark induced bubble, and from laser induced bubbles at three different liquid pressure. All the experimental data superpose well for the first growth and collapse phase of the bubble. However, the growth of the rebound varies from case to case, depending on both the pressure in the liquid and the method for bubble generation. The experimental data for the first collapse are consistent with the Rayleigh-Plesset curve. Furthermore, we notice that the growth phase is reasonably symmetric to the collapse phase. The dashed curve on the graph is the mirror (from $t^* = 0$) of the Rayleigh-Plesset curve. The similarity between the experimental data and the theoretical curve from to generation until the last stage of the collapse implies that the method for the generation of the bubble does not affect significantly the dynamics for these two phases. However, we note large variations in the rebounds.

According to Fig. 2.3, the dynamics of the rebound depends on both the pressure in the liquid and the method for the bubble generation. Comparing the laser cases, we observe that the rebound bubbles become larger when the pressure in the liquid decreases. This behavior is

deeply addressed in Ch. 6. However, the rebound obtain with the spark bubble at atmospheric pressure is as large as the laser bubble obtained at low pressure (10 kPa). This difference is thought to be caused by the gas inside the bubble. In the case of the bubble generated by energy deposition, non-condensable gas is formed by dissociation of water in the plasma at the generation of the bubble. This gas is trapped inside the bubble during the collapse phases, and eventually diffuses in the water. Sato *et al.* [27] measured the concentration of hydrogen in water after the collapse of a laser bubble and a spark bubble. The concentration of hydrogen after a spark bubble was three times larger than after a laser bubble, for the same potential energy in the initial bubble. A larger amount of gas inside the bubble at the collapse leads to larger rebound bubble.
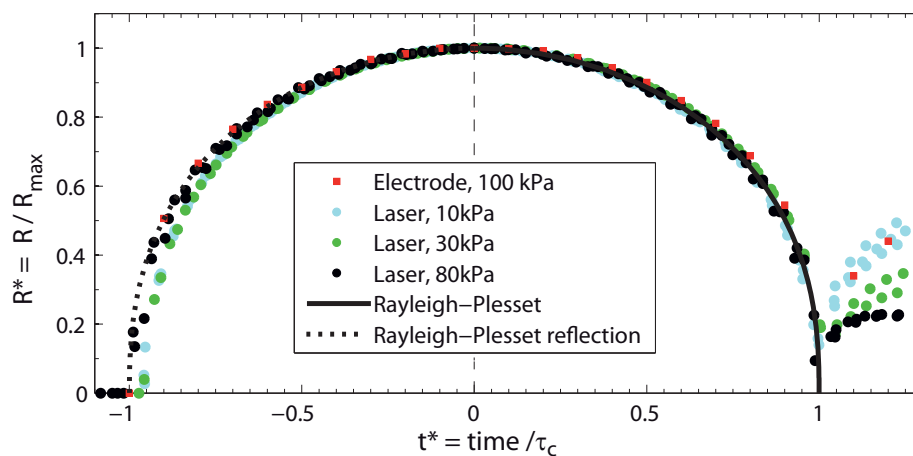
Figure 2.3: Plot of the normalized radius as a function of the normalized time calculated measured for laser induced bubbles at three different pressures in the liquid (dots) and for a spark induced bubble (square). The solid curve is the theoretical collapse of a bubble, calculated with the Raylei-Plesset model, and the dashed curve is the reflection of the curve across the axis t^*=0.

Are hydrodynamics bubbles and laser bubbles the same ? In fact, they are not the same. The bubble content is different. In consequence, the phenomena associated with the last stage of the collapse, when the gas inside the bubble is compressed, might be affected. However, the phenomena are qualitatively similar: apparition of a rebound bubble, microjet, shock waves, and luminescence. The conclusions drawn from the investigations on laser induced cavitation bubble can still be transposed to hydrodynamic cavitation bubbles, as long as we keep in mind the possible influence of the gas content.

2.4 The thermodynamic effect

The temperature of the liquid affects the dynamics of the cavitation bubble. Physical properties such as the vapor pressure, the density, the surface tension and the viscosity are function of the temperature of the fluid. The vapor pressure p_v as a function of the temperature T can be calculated with the Antoine equation 2.4. The variation of the other physical properties can be extrapolated from reference tables [58].

$$log_{10}(p_v) = A - \frac{B}{C - T}$$

(2.4)

with A = 5.4022, B = 1838.675, C = -31.737. The pressure is in bars, and the temperature in K.

The effect of the temperature on cavitation occurrence, called the thermodynamic effect, has been reported in the case of pumps. Although the variation of the vapor pressure is considered in the calculation of the cavitation number, we still observe that the breakdown cavitation number decreases when the temperature of the liquid increases. This phenomenon is not well understood, but it is thought to be due to the variation of the vapor density with the temperature, which implies variation of mass rate of evaporation for a given volume growth [59].

The influence of the temperature can also be observed in the case of laser-induced bubbles. Figure 2.4 shows the radius as a function of time for two bubbles generated with the same laser input energy, one in water at 3 °C, and the other at 44 °C. We observe that for a higher temperature, the rebound bubble is significantly larger (2.5 times larger in this case). However, the study of the thermodynamic effect is beyond the scope of this thesis. Therefore, we restrict ourselves to water temperature in the vicinity of 20 °C, which is what is the typical nominal temperature for hydraulic machine testing [60]. When the temperature varies over a small range, the discrepancies induced by the temperature differences become insignificant. To illustrate this, several movies were recorded at a water temperature of 19°C and 26°C respectively. Figure 2.5 plots the average radius of the bubble as a function of time for each temperature. The difference between the two cases is small, as summarized in Tab.2.1. The differences in the maximum radius (R_{max}) or maximum radius of the rebound (R_{reb}) from one case to the other are of the order of the standard deviation of the measurement(σ).

	$R_{max} \pm \sigma$:	$R_{reb} \pm \sigma$
19 °C :	1.653 ± 0.017	0.266 ± 0.060
26 °C :	1.674 ± 0.011	0.304 ± 0.024

Table 2.1: Maximum radius of the bubble and of the rebound bubble, along with the standard deviation, for two cases, at respectively 19 °C and 26 °C.
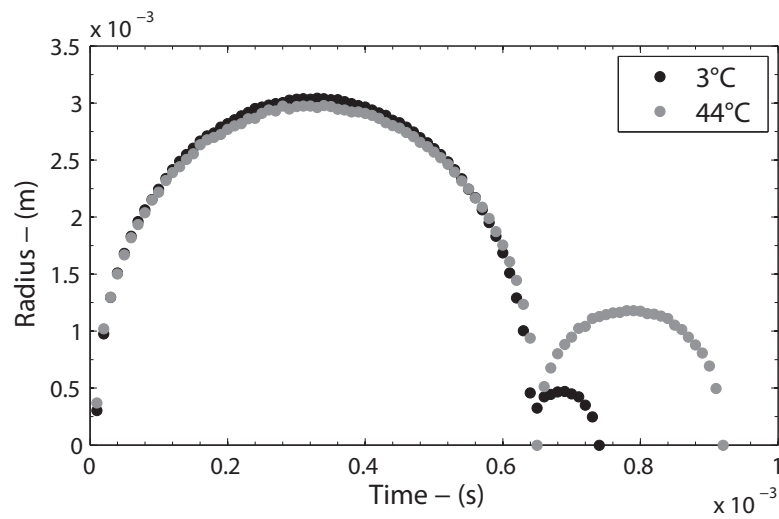
Figure 2.4: The radius as a function of time for a bubble in water at 3°C and 44°C respectively. The growth and collapse of the bubbles are similar, but the rebound bubble is 2.5 times larger at higher temperature.
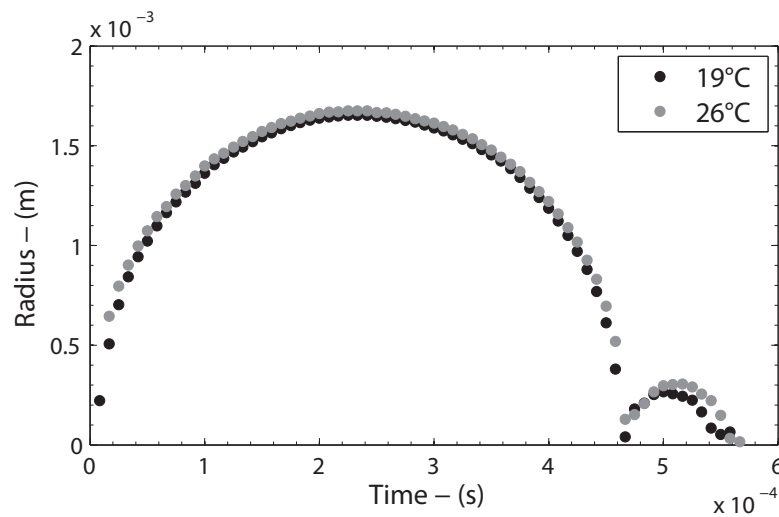
Figure 2.5: The radius as a function of time for a bubble in water at 19°C and 26°C respectively. Despite a difference of 7°C, the growth, the collapse, and the rebound of the bubbles are similar (within the standard deviation of the measurements).

3 Effect of the pressure gradient around a hydrofoil on the collapse of a bubble

3.1 From the turbine to the cavitation tunnel: simplification of the problem

Despite decades of research on the subject, cavitation remains a major issue in hydraulic machines. In the particular case of hydraulic turbines for instance, the design of the turbine and the nominal operating point are adapted in order to avoid cavitation. However, with new global energetic challenges, hydraulic turbines are not expected to run only at one nominal point. Most hydraulic power plants are expected to adapt their production to meet the requirement of complex electric network including , even more in the future, the unsteady renewable energy sources. Under these conditions, cavitation occurrence in the turbine might not be avoidable. Cavitation is not only a source of performance losses. Cavitation is a source of damages on the turbine. The collapse of cavitation bubbles on the blade of the turbine induces erosion which, for serious cases, leads to the replacement of the turbine, at very high costs.

A first step to simplify the problem of cavitation within hydraulic turbine is to investigate what happens when one blade (a hydrofoil with a standard geometry) is placed in a flow with a uniform inlet (the flow within the test section of the cavitation tunnel). The experimental condition at the inlet of the test section, namely the velocity of the flow and the pressure in the liquid, and the geometry and angle of attack of the hydrofoil can then be modified to obtain different types of hydrodynamic cavitation on the profile, among which, cavitation bubbles collapsing on the blade.

Investigations on cavitation bubbles traveling along a hydrofoil have already been performed both at the LMH [61, 62], and elsewhere [63, 64]. The innovation of the present study stands on the use of a laser to generate the cavitation bubble. With this technique, the bubbles can be generated (on demand) at any location within the flow around the hydrofoil. This allows to probe the behavior of the cavitation bubble generated at different distances from the hydrofoil and, more important, for different pressure gradient intensities. Indeed, for a liquid flow

around such a solid profile, the pressure gradient is highly space dependant. Therefore, the pressure gradient acting on the bubble during the growth and collapse varies with the location of the bubble generation.

3.2 Experimental setup

3.2.1 The EPFL high speed cavitation tunnel

The experiments take place in the EPFL high speed cavitation tunnel [65]. The test facility, shown in Fig. 3.1, is a closed loop circuit providing a rectangular test section of 150 x 150 x 750 mm. The honey comb located in the contraction upstream to the test section reduces the turbulence intensity in the flow to less than 2 % [66]. A double suction pump produces a pressure head of 36.5 m for 1.125 m^3/s at 885 rpm. The maximum flow velocity at the test section inlet is 50 m/s. The transit time for a fluid particle to complete the loop at this maximum flow rate is 98 s. The long pipe with a large diameter, located at the middle of the tunnel acts as a bubble resorber. It reduces the flow to 3 % of the test section inlet velocity. The bubbles can rise to the top of the pipe, where they are trapped and removed.
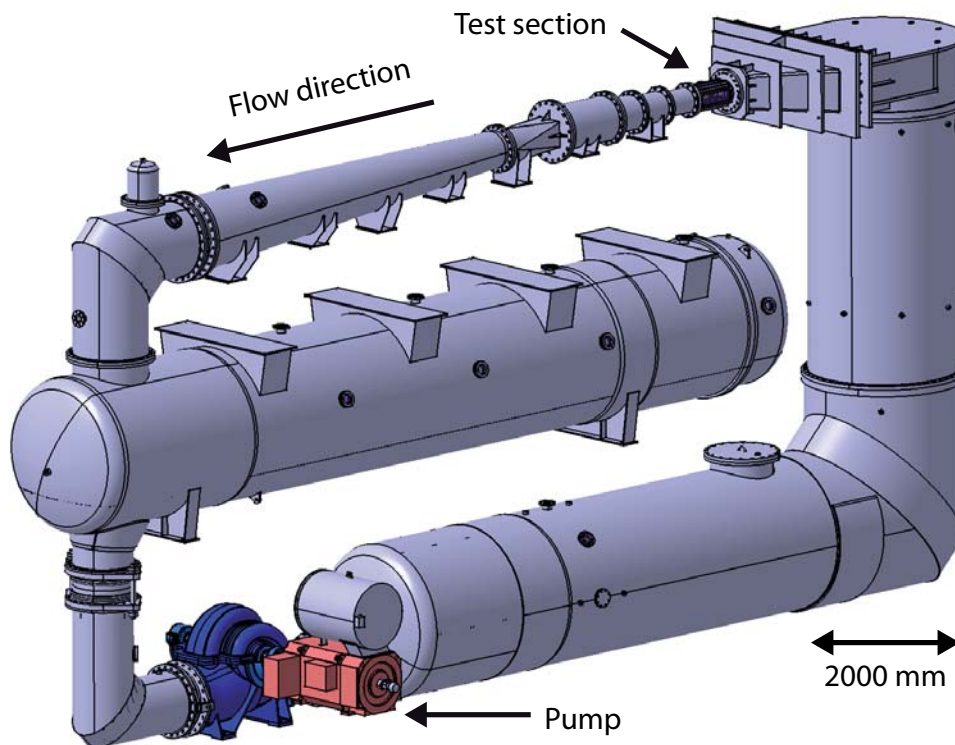
Figure 3.1: The EPFL high speed cavitation tunnel

3.2.2 The hydrofoil

We place in the test section a stainless steel hydrofoil (geometry drawn in Fig. 3.2). This Naca 0009 profile has a span of 150 mm and a maximum thickness of 9 % located at 45 % of the chord length. The geometry is defined by the Eq. 3.1, using L = 110 mm for the chord length. The hydrofoil is then truncated at 100 mm, resulting in a 3.22 mm thick trailing edge.

$$
0 \le \frac{x}{L} \le 0.5 \qquad \frac{y}{L} = a_0 \left(\frac{x}{L}\right)^{1/2} + a_1 \left(\frac{x}{L}\right) + a_2 \left(\frac{x}{L}\right)^2 + a_3 \left(\frac{x}{L}\right)^3
$$

$$
0.5 \le \frac{x}{L} \le 1 \qquad \frac{y}{L} = b_0 + b_1 \left(1 - \frac{x}{L}\right) + b_2 \left(1 - \frac{x}{L}\right)^2 + b_3 \left(1 - \frac{x}{L}\right)^3
$$

$$
\begin{aligned}
a_0 &= +0.1737, & a_1 &= -0.2422, & a_2 &= +0.3046, & a_3 &= -0.2657 \\
b_0 &= +0.0004, & b_1 &= +0.1737, & b_2 &= -0.1898, & b_3 &= +0.0387
\end{aligned}
$$

(3.1)
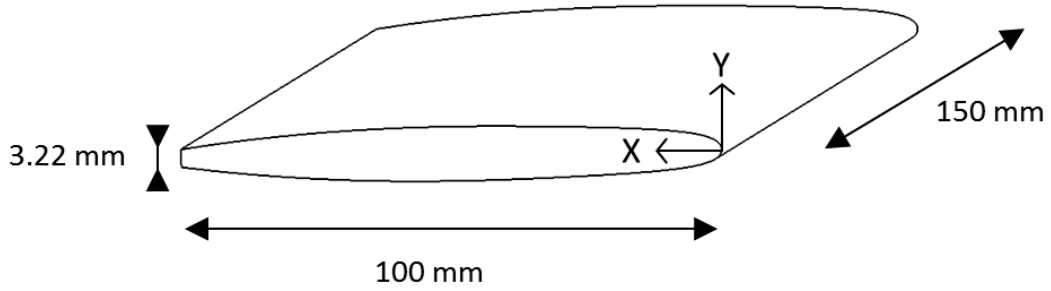
Figure 3.2: The truncated NACA 0009 hydrofoil

For our experiment, we restrain ourself to one flow condition. The water pressure and the flow velocity at the inlet of the test section are respectively 0.45 bar and 15 m/s, with a constant angle of attack of 1°. These conditions correspond to a coefficient of cavitation $\sigma = 0.39$ (Eq. 3.2). The pressure distribution on pressure and suction sides of the hydrofoil for an angle of attack of 1° is plotted on Fig. 3.3. Note that the X axis direction goes from the right to the left, to be consistent with the flow direction on the high speed images. The experimental conditions were chosen to reconcile the following requirements:

- The flow velocity should be high enough to allow the bubble to travel a significant distance in the pressure field before collapsing.
- Meanwhile, the velocity should not be too high, otherwise the bubble is washed away from the observation area in the flow.

19

- The inlet pressure has to be low to favor the generation of large bubbles, which are easier to observe.
- However, the minimum pressure on the hydrofoil surface should be above the vapor pressure to avoid hydrodynamic cavitation.

$$\sigma = \frac{p_{ref} - p_v}{\frac{1}{2}\rho C_{ref}^{2}} \qquad (3.2)$$

$$c_p(x) = \frac{p(x) - p_{ref}}{\frac{1}{2}\rho C_{ref}^{2}} \qquad (3.3)$$

p_{ref} is the pressure at the test section inlet, p_v the vapor pressure of water, C_{ref} the flow velocity at the inlet, $p(x)$ the pressure on the hydrofoil surface as a function of the chord position x, and ρ the water density.
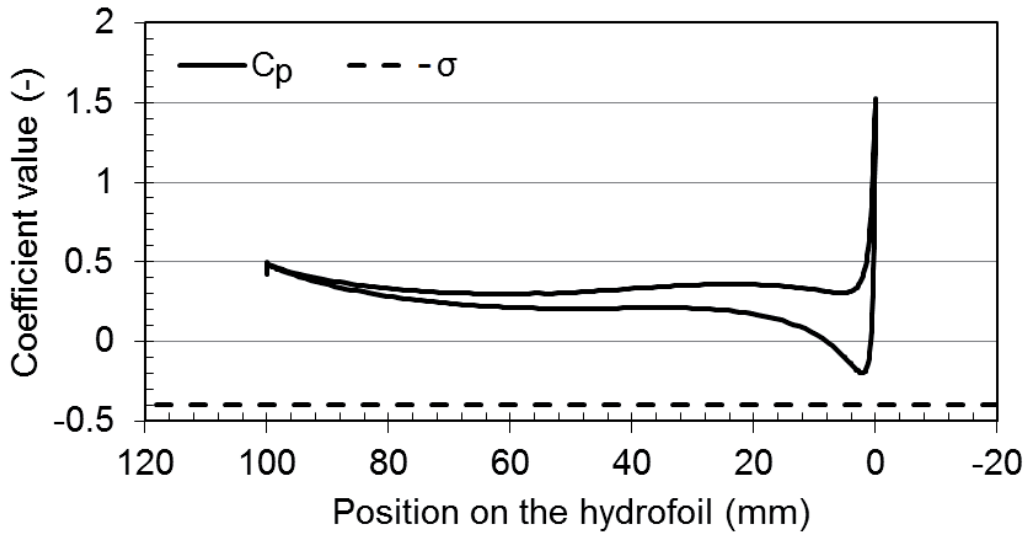
Figure 3.3: Pressure coefficient c_p as a function of the distance on the chord of the truncated NACA 0009 hydrofoil, for an angle of attack of 1°. The dashed line is the cavitation coefficient σ for the experimental conditions.

3.2.3   Generation and observation of a bubble

The bubbles are obtained by focussing a laser pulse in the test section through the plexiglass front window, as illustrated in Fig 3.4. The laser is a Q-switched Nd:YAG laser (New Wave Minilase III) delivering pulses up to 11 mJ and 5 ns at a wavelength of 532 nm. The laser

beam of 3.5 mm is expanded 12 times with a set of one diverging and one converging lens, then focussed into the water, through the plexiglas, by a converging lens. To be able to reach the water breakdown threshold, the energy of the laser pulse has to be focussed into a small volume of liquid. To optimize the focalization, the laser beam has to be focussed with a largest possible convergence angle. The focussing system used is sketched in Fig. 3.5. The whole bubble generation system is mounted on a computer comtrolled traverse system. This allows to generate a bubble anywhere around the hydrofoil, within the vertical plane 30 mm behind the front plexiglas window.
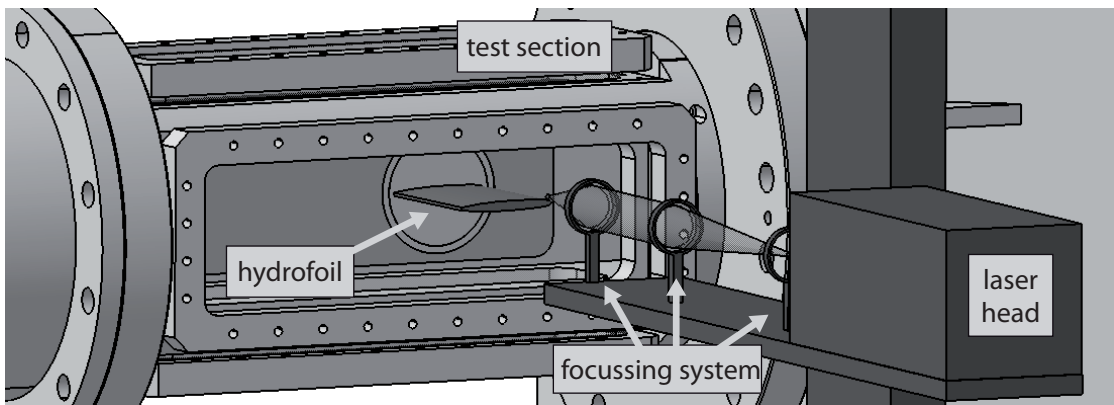
Figure 3.4: Sketch of the test section of the EPFL high speed cavitation tunnel with the laser and the focussing system for bubble generation. One diverging and one converging lens expand the laser pulse, while the converging lens close to the plexiglas focuses the pulse into the water.
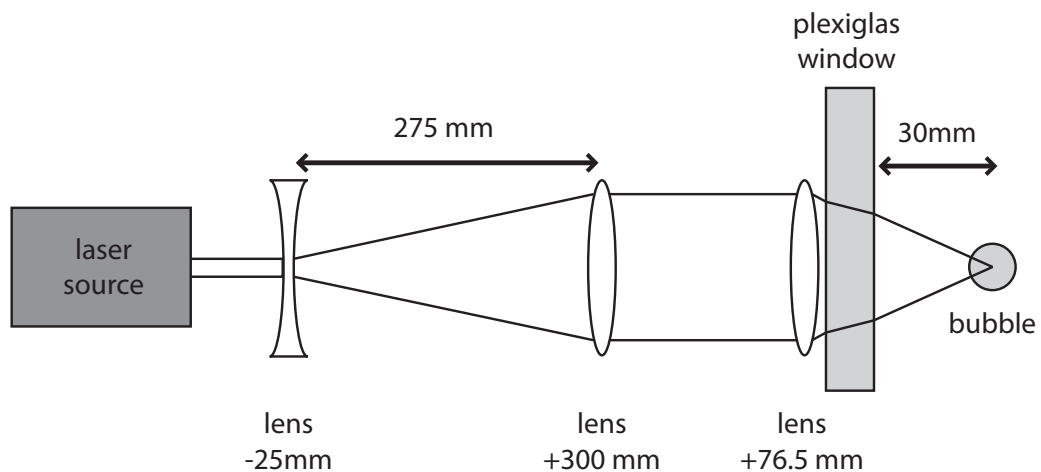
Figure 3.5: Sketch of the laser focussing system used to generate bubbles in the cavitation tunnel.

Movies of the laser-induced bubbles are recorded with a high-speed camera (Photron Fastcam SA1.1). To obtain sharp images, it is necessary to have a lot of light in order to reduce the exposure time on the camera. We use two xenon flashes (Cordin Model 359) delivering a maximum energy of 1100 J during 11 ms. The synchronization of the laser-camera-flashes is controlled by the high-speed camera. When the experimenter starts the recording from the camera software on a computer, two TTL signals are sent from the camera. One triggers the flashes, and the other the optical pumping of the YAG rod, leading to the emission of the laser pulse. The flashes are fixed, respectively, on the top and on the front of the test section, allowing to observe the interface of the bubble. Fig. 3.6 shows a typical example of the images we have recorded. It is a superposition of high speed images taken for one cavitation bubble. Note that some "parasite" cavitation appears on the hydrofoil, at the corner edge close to the plexiglas. The sub-millimetric gap between the edge of the hydrofoil and the plexiglas generates a local pressure drop that induces tiny cavitation bubbles, entrained by the flow. The value for the conversion of the pixels on the movie in millimeters is calculated using a reference object of known dimensions placed on the hydrofoil. The spatial resolution is 6.85 pixels per millimeters and the temporal resolution, given by the frame rate set on the camera, is 20 μs.
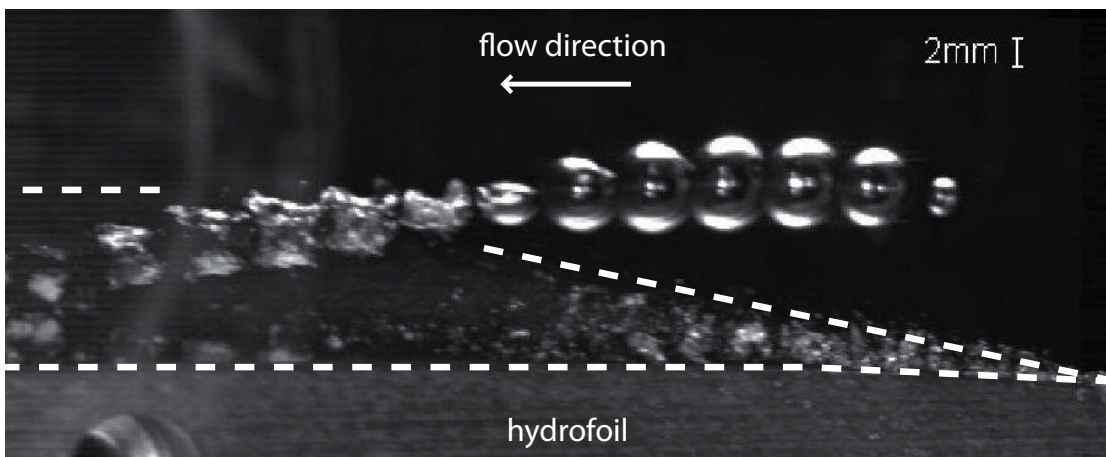
Figure 3.6: Superposition of the images from a typical high speed movie of a laser-induced bubble generated above the hydrofoil. The bubble travels in the flow above the hydrofoil, growing and collapsing. The rebound bubble appears like a cluster of microbubbles. Interframe time: 200 μs

3.2.4 Presentation of the four case studies

We will analyse four case studies. The coordinates of the position of the generation of each bubble are given on both Figs. 3.7 and 3.9. In the cases 1 and 2, the interaction between the bubble and the pressure gradient is weak. The bubbles collapse downstream to the leading edge, where the pressure is low. In the cases 3 and 4, the interaction between the bubble and the pressure gradient is strong. The bubble collapses in the vicinity of the leading edge, where

the intensity of the pressure gradient is high. In the cases 1 and 4, the bubble, respectively the rebound bubble, travels on the surface of the hydrofoil. In the case 2 and 3, the bubble moves in the flow above the hydrofoil.

The Navier-Stokes equations for our flow configuration has been solved with ANSYS CFX, considering a two-dimensional flow. This numerical simulation leads to a solution for the flow and the pressure field around the hydrofoil, which allows to estimate the trajectory of the bubble and the pressure experienced by the bubble. The system of coordinates giving the position of the generation of the bubble is defined as follow. The origin is given by the leading edge of the hydrofoil when the angle of attack is 0 °. The X direction is the horizontal direction and the Y direction is the vertical. Figure 3.7 shows the isobar lines around the hydrofoil, calculated numerically (details in appendix A.1).
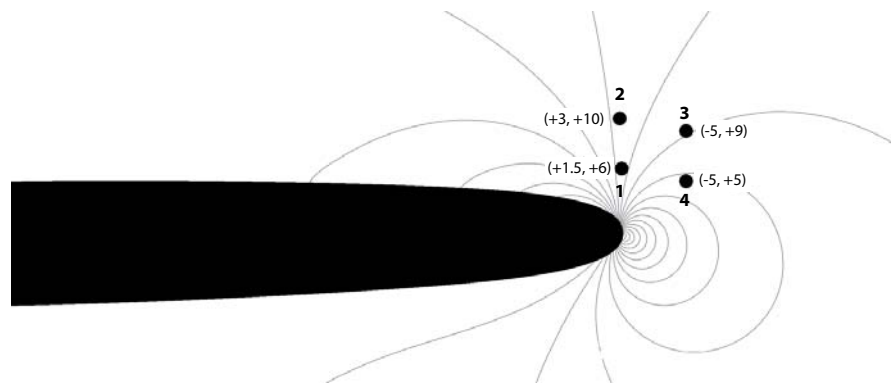
Figure 3.7: Pressure field around the hydrofoil, with the position of the generation of the bubbles for the four case studies treated in the chapter. The minimum pressure on the hydrofoil is 13 kPa, and the maximum, at the leading edge, is 207 kPa. There is 10 kPa between two isobares.
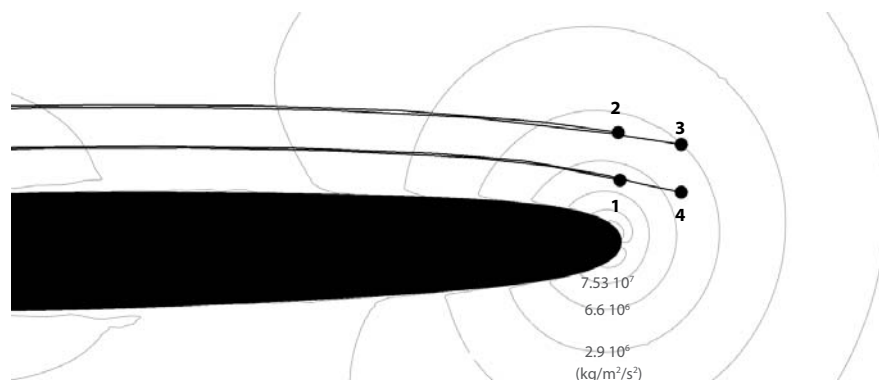
Figure 3.8: Pressure gradient isolines around the hydrofoil, together with the streamlines for the four case studies treated in the chapter. Note that the isolines are logarithmically spaced.
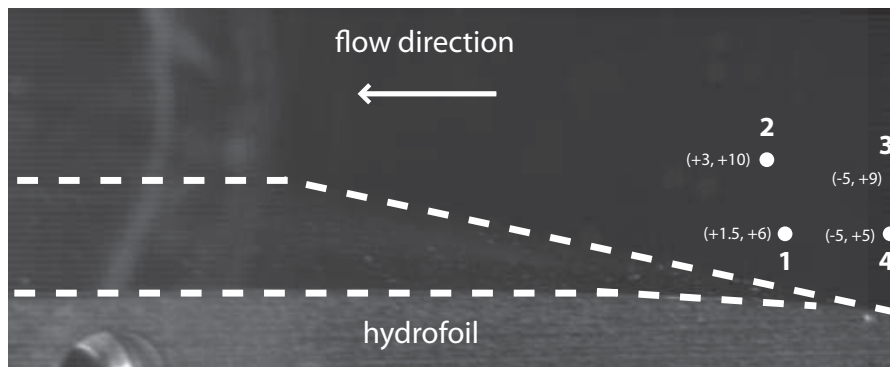
Figure 3.9: Coordinates of bubble initiation sites. The coordinates are given in millimeters, according to the axis defined in Fig. 3.2.

3.3 Weak interaction between a bubble and the pressure gradient

3.3.1 Bubble traveling on the surface of the hydrofoil

The case 1 treats the bubble traveling on the surface of the hydrofoil. The laser is focussed above the leading edge of the hydrofoil, as shown in Fig. 3.10. Figure 3.11 is a superposition of high-speed images of the bubble. The bubble grows downstream from the leading edge. Once the bubble reaches its maximum radius, the collapse process starts. The top of the bubble becomes flat, and advances into the the bubble. The bubble eventually takes the shape of a "donut" and collapses. This type of collapse is called a toroidal collapse. The portion of liquid going through the bubble and impacting the bottom of the bubble is the microjet. Figure 3.12 shows the formation of the microjet and the toroidal collapse for the same bubble, viewed from the top of the test section.

Figure 3.10: The isobars around the hydrofoil, and the streamline starting from the position of the generation of the bubble, at (+1.5, +6).

24

Figure 3.11: Case 1: The bubble traveling on the surface of the hydrofoil. The grey dash lines are the axis perpendicular to the flap top of the bubble and passing through the center. Interframe time: 400 μs, maximum diameter: 7 mm, bubble lifetime: 3.1 ms.
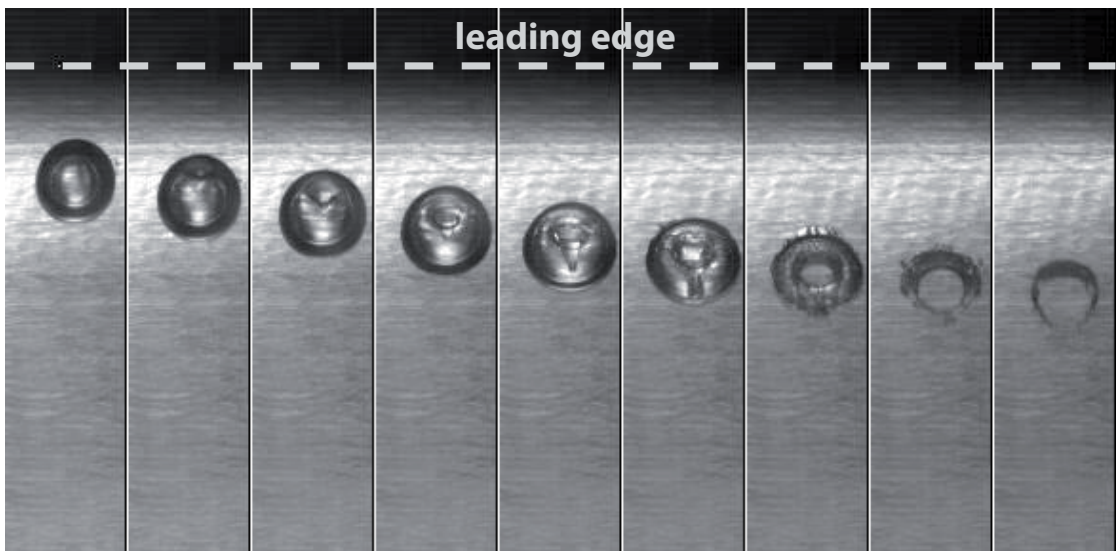
Figure 3.12: Case 1: High speed images of the collapsing bubble taken from the top of the test section. Interframe time: 60 μs, maximum diameter: 7 mm, bubble lifetime: 3.1 ms.

The microjet and the toroidal collapse are characteristic for collapse of a bubble on a solid surface in a liquid at rest [32, 67, 39]. Figure 3.13 shows the collapse of a cavitation bubble near a solid surface (just below the bubble) in a liquid at rest. During the collapse process, we observe that the bubble interface diametrally opposite to the solid wall flattens. A liquid jet, the microjet, pierces and advances through the whole bubble from the top. The microjet eventually hits the bubble interface and the solid surface, and the bubble takes the shape of a flat thorus. This high speed liquid microjet is thought to cause erosion. The high pressure reached locally, where the microjet hits the surface, damages the surface. The repetition of

this phenomenon leads to the formation of pits on the surface.
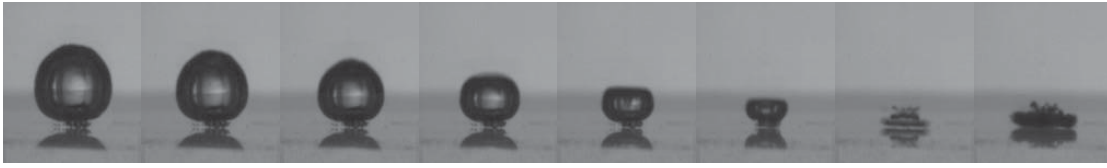
Figure 3.13: High speed images of the development of the microjet at the last stage of the collapse of a cavitation bubble near a solid surface. The interval between the numbered frames is 8 μs and the frame width is 3 mm.

The bubble traveling on the hydrofoil takes a particular shape just before the last stage of the collapse. The top of the bubble is flat and inclined towards the downstream side. Interestingly, this shape is similar to the shape of hydrodynamic bubbles traveling on a hydrofoil surface. Previous observations [61, 63, 64] report bubble shapes changing from hemispherical to a so called "wedge" shape, i.e., a bubble with triangular vertical section. The laser-induced bubble generated here also take this particular shape, as shown in Fig. 3.14. As this shape is similar for both laser and hydrodynamic bubbles, we assume that it results from the flow over the hydrofoil.
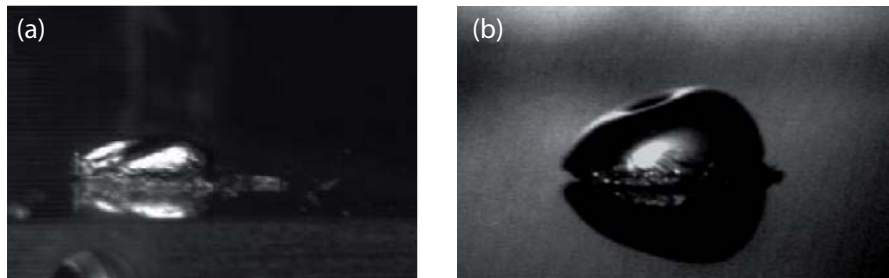
Figure 3.14: Traveling bubbles observed in two different studies. Despite of different generation methods,(a) is generated by laser while (b) is "hydrodynamic" cavitation, the same shape is observed. (b) from [61].

We observe on the high speed images that the inclination of the flat top of the bubble is changing while the bubble moves along the hydrofoil. The top is first inclined towards the upstream side, and finishes inclined towards the downstream side. We found two possible explanations for this phenomenon. It could be a rotation of the bubble on itself, as suggested by the variation of the angle between the vertical and the axis perpendicular to the flat top in Fig. 3.11. The other explanation could be that the shrinking of the top downstream side of the bubble that catches up and overtakes the shrinking of the upstream side. It is actually difficult to confirm one rather than the other possibility with the images of the bubble. In any case, this phenomenon does not occur in the case of a bubble in a liquid at rest, where the flat part of the bubble remains parallel to the solid surface. Therefore we conclude that this phenomenon is caused by the flow.

3.3.2 Bubble collapsing above the hydrofoil

In the case 2, the bubble is generated above the profile, so that a significant gap of water (> 3× the maximum radius of the bubble) is kept between the bubble and the solid surface until the first collapse. The position of the generation of the bubble, and the streamline starting from this point are plotted in Fig. 3.15. The high speed images of the growth, collapse, and rebound of the bubble are shown in Fig. 3.16. As in the case 1, we observe that the top of the bubble flattens during the collapse. In contrast, the bottom half of the bubble shrinks quite spherically until the last moment of the collapse. The rebound appears as a cloud of microbubble.

Figure 3.15: The isobars around the hydrofoil, and streamline starting from the position of the generation of the bubble, at (+3, +10).

Figure 3.16: Case 2: Collapse of a bubble above the hydrofoil. The collapse is not spherical, it is initiated at the top of the bubble. Interframe time: 200 μs, maximum diameter: 7 mm, bubble lifetime: 1.28 ms.

Studies of collapsing bubbles in water at rest concluded that the influence of a solid surface is negligible when the standoff is > 3. However, in our case, the standoff parameter is > 3 during

the first growth and collapse of the bubble, and we still observe a non-spherical collapse. We conclude that the asymmetric collapse is not induced by presence of the solid surface, but by the flowing liquid. To identify the cause of the asymmetry, we consider the pressure field around the hydrofoil and the trajectory of the bubble. Because of the pressure gradient in the liquid, the top of the bubble experiences a higher pressure than the bottom of the bubble. The result of this unbalance favors a faster collapse of the upper half of the bubble than the lower half, which actually match our observation. Therefore, we postulate that a pressure gradient in the liquid is sufficient to initiate a non-spherical collapse of the bubble, and ultimately to the generation of a microjet. To confirm this, we present in the next section the cases of bubble generated upstream to the leading edge, in the region where the intensity of the pressure gradient is the highest.

The trajectory of the bubble is well represented by the superposition of the images in Fig. 3.16. However, the trajectory does not follow the streamline drawn in Fig. 3.15. The bubble migrates towards the hydrofoil, while the streamline shows that a fluid element would flow over the hydrofoil keeping an almost constant distance with the solid surface. We explain this difference as being an effect of the microjet at the collapse of the bubble. We assume the asymmetric collapse and the formation of the microjet to put the bubble into motion in the direction of the microjet. In our particular case, the microjet is directed towards the solid surface. This downwards motion combines with the flow, leading to the trajectory observed. Note that one can wonder if the downwards motion is not due to the buoyancy effect on the bubble, i.e. the bubble being attracted towards the hydrofoil, where the pressure is lower. We excluded this possibility because the buoyancy forces would move the bubble much slower than what we observe.

3.4   Strong interaction between a bubble and the pressure gradient

3.4.1   Apparition of a microjet parallel to the direction of the pressure gradient

In the case 3, the bubble is generated in the area upstream to the leading edge, where the intensity of the pressure gradient is high, see Fig. 3.17. We investigate the influence of the pressure gradient on the dynamics of the bubble, and in particular on the generation of a jet.

Figure 3.18 shows a superposition of high speed photographs of this bubble. The high speed movie reveals peculiar bubble dynamics, quite different from what presented in the previous section. In this case, we do not observe the toroidal collapse and the microjet directed towards the solid surface. More details about the collapse are visible in Fig. 3.20, where all the frames of the high speed movie are presented. The bubble remains quite spherical until the end of the first collapse (frame (d)). The rebound of the bubbles appears like a compact cloud of microbubbles (frame (f)). But on the following frame, we observe the growth of a jet of vapor at the rear of the rebound (frames (g) to (i)). The jet then disappears and the rebound becomes quite spherical (frames (k) to (l)). The apparition of a jet of vapor actually denotes

that a microjet pierces the bubble during the collapse. The microjet entrains some vapor while going through the bubble, and the vapor jet grows outside of the bubble following the stream.
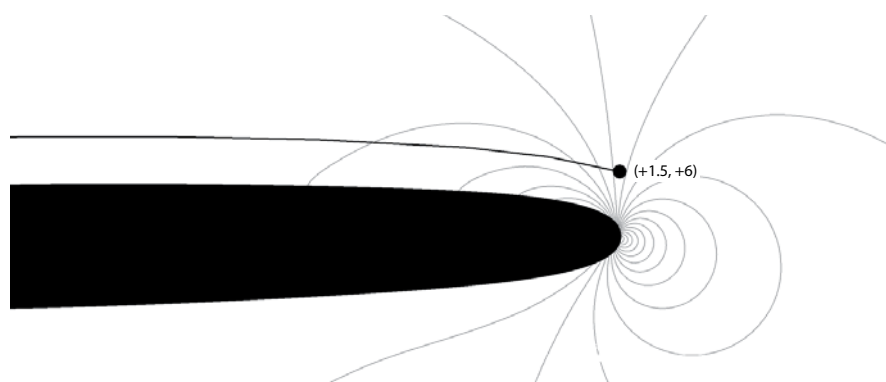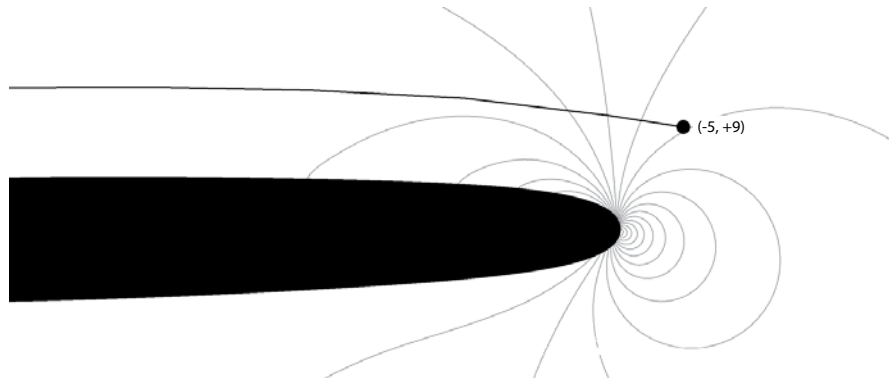

Figure 3.17: The isobars around the hydrofoil, and streamline starting from the position of the generation of the bubble, at (-5, +9).

The puzzling question is: Why, in this case, the jet takes this direction ? The answer becomes clear when we superpose the trajectory of the bubble with the isobar lines around the hydrofoil (see Fig.3.19). We see on the figure the jet perpendicular to the isobar lines, which means by definition that the jet has the same direction as the pressure gradient. Actually, to be correct, the jet develops in the direction opposite to the pressure gradient. This observation implies that in this case the influence of the pressure gradient in the liquid is stronger than the influence of the solid surface.

Figure 3.18: Case 3 : Superposition of the high speed images of the collapse of a bubble generated at (-5, +9). The bubble bubble has a microjet not towards the solid surface. Interframe time: 180 μs, maximum diameter: 5 mm, bubble lifetime: 440 μs.
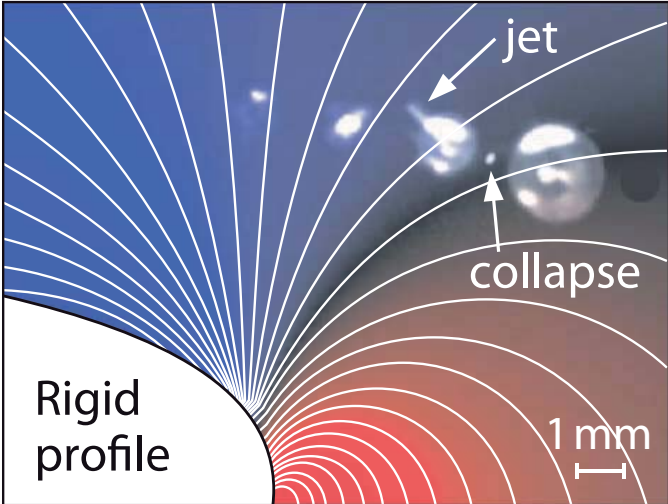
Figure 3.19: Case 3 : Superposition of the isobars on the high speed images of the collapse of a bubble with a strong interaction with the pressure gradient. A jet, perpendicular to the isobars, appears on the rebound bubble. [41]
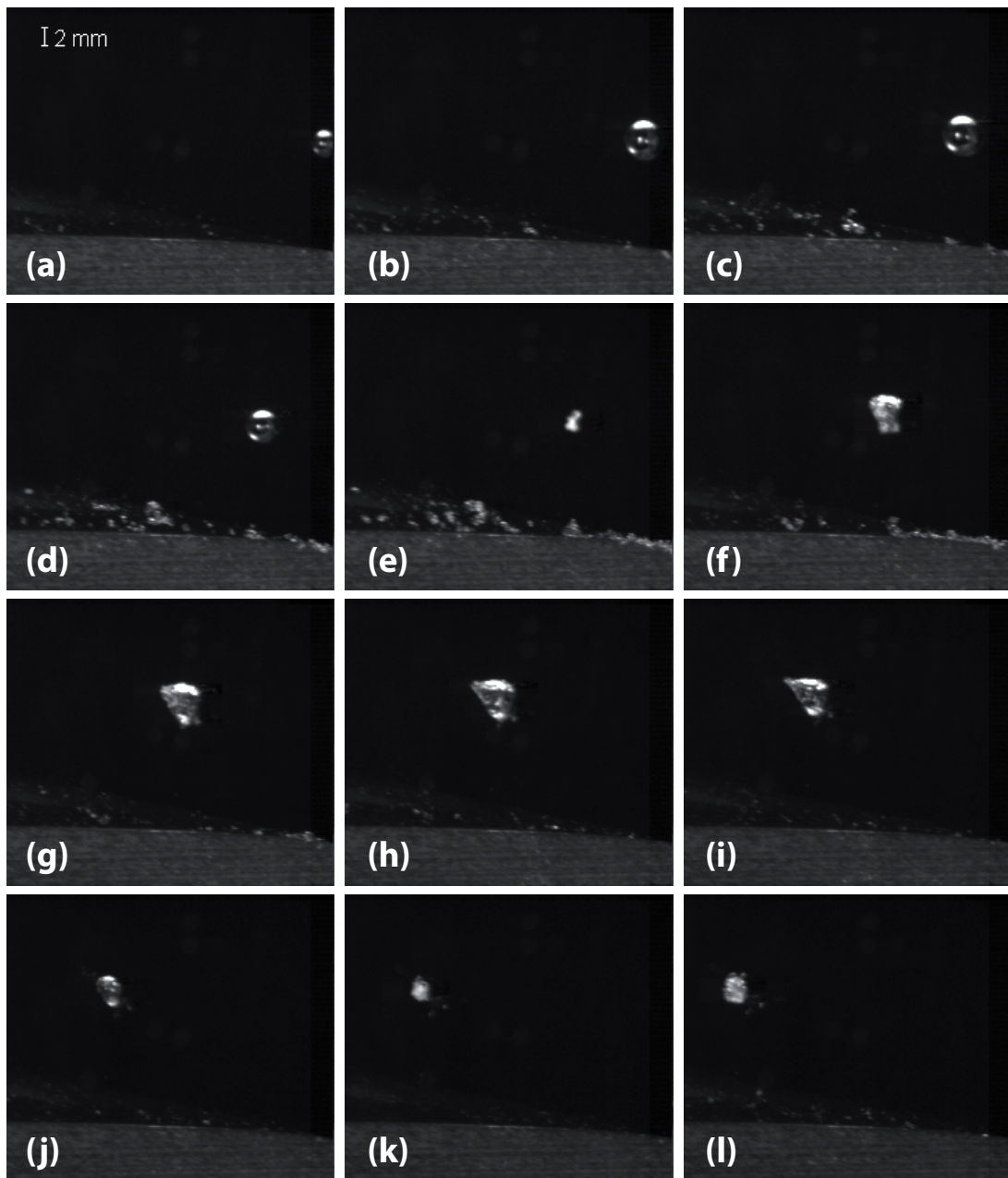
Figure 3.20: Case 3 : High speed images of the collapse of a bubble generated at (-5, +9). The microjet and its direction, parallel with the flow, clearly visible. Interframe time: 100 μs, maximum diameter: 5 mm, bubble lifetime: 440 μs.

3.4.2 Cloud of microbubbles traveling on the surface of the hydrofoil

In the case 4, we generate a bubble upstream to the leading edge (see Fig. 3.21) so that the rebound bubble flows along the hydrofoil, like the traveling bubble presented in the case 1. Because the bubble collapses in the region of strong pressure gradient, we observe the apparition of a jet in the direction opposite to the local pressure gradient rather than in the direction of the solid surface. The interesting feature with this bubble is its rebound, as shown in Fig. 3.22. The collapse happens such that fission occurs on the rebound bubble [30]. The rebound bubble takes the shape of an expanding, vertically elongated, cloud of microbubbles. As the rebound advances over the hydrofoil, the microbubbles at the bottom of the cloud, close to the hydrofoil, start to coalesce, forming one large bubble. Meanwhile, the microbubbles at the top of the cloud move towards the solid surface, and start to collapse. This motion induces a stream of liquid flowing through the cloud of microbubble, towards the hydrofoil, like a microjet. At the last stage of the collapse, the bubble becomes toroidal. Its shape is similar to the shape of the traveling bubble described before, as shown in Fig. 3.23. We observe in both cases the "wedge" shape and the hole induced by the microjet.

It is interesting to note that the microbubbles in the cloud do not behave independently to each other after the first collapse. The microbubbles close to the hydrofoil coalesce and generate one bigger bubble that behaves like a traveling bubble along the hydrofoil. Meanwhile, the microbubbles at the top of the cloud collapse in a methodic matter: from the top towards the bottom. This behavior is thought to be caused by the configuration of the pressure field around the hydrofoil. The low pressure near the hydrofoil favors the coalescence of the microbubbles. The further from the hydrofoil, the larger the pressure is. We thus expect the collapse to start at the top of the bubble. However, it is still surprising to observe the formation of a microjet, piercing the whole elongated rebound bubble and provoking the toroidal collapse of what was, just after the first collapse, a shapeless could of microbubbles.
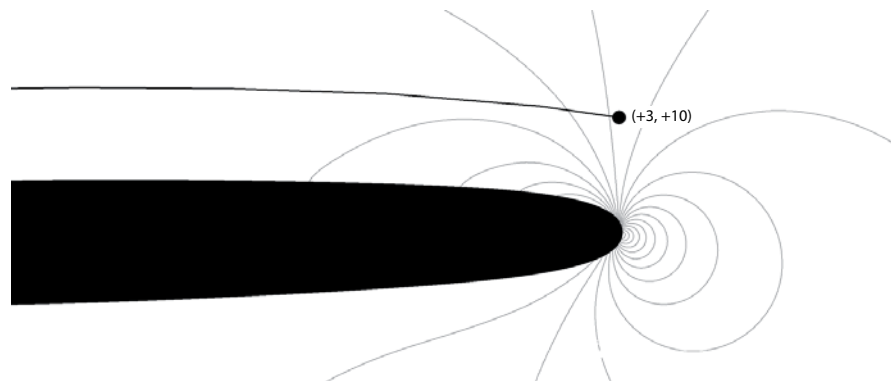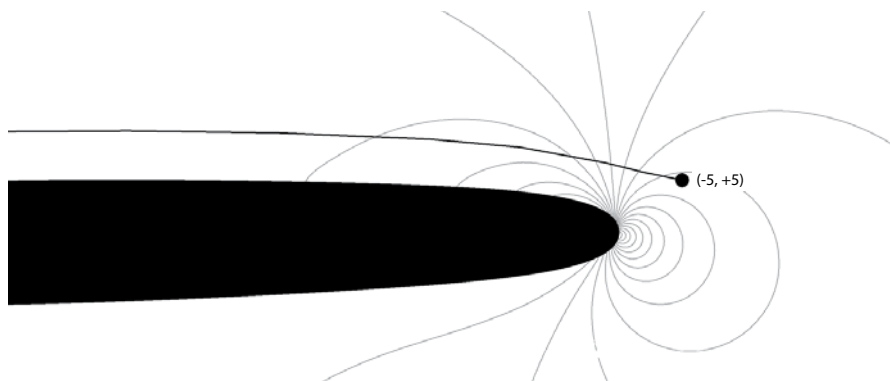

Figure 3.21: The isobars around the hydrofoil, and streamline starting from the position of the generation of the bubble, at (-5, +5).
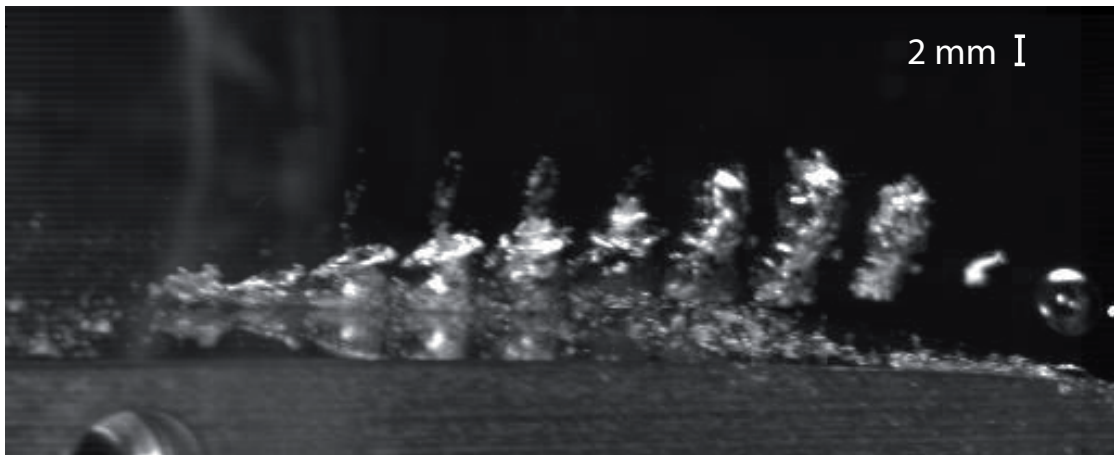
Figure 3.22: Case 4 : Superposition of the high speed images of the collapse of a bubble generated at (-5, +5). The bubble collapses upstream to the leading edge. The rebound, a cloud of microbubbles, travels and collapses on the surface of the hydrofoil. Interframe time: 200 μs. Initial bubble maximum diameter: 5 mm, lifetime: 380 μs. Rebound bubble maximum diameter: 6 mm, lifetime: 2 ms.
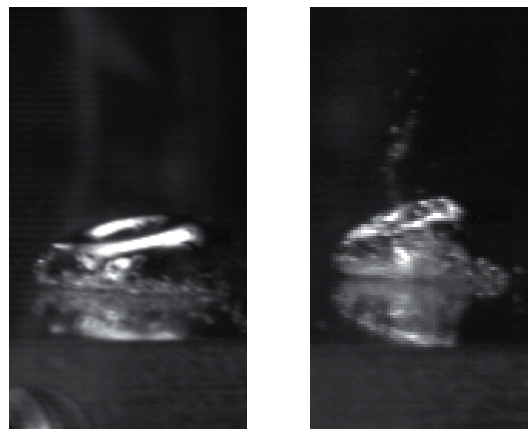
Figure 3.23: Comparison of the shape of the collapsing bubble in: (a) case 1, where the bubble experiences its first collapse, and (b) case 4, where the rebound bubble, a cluster of microbubbles, collapses. In both cases we observe the similar wedge shape.

3.5 Discussion

The observations of laser-induced cavitation bubbles around the hydrofoil reveal a tight relation between the pressure gradient in the liquid and the dynamics of the bubble. In particular, we observe that the jet takes the direction of the pressure gradient. This statement is reasonable when looking at the pressure forces applied on the bubble. The pressure gradient makes one side of the bubble experience a stronger force than the other. One interface would collapse faster towards the center. This loss of symmetry is thought to lead to the apparition of the microjet.

The small turbulence intensity in the flow does not affect the dynamics of the bubble. The formation of Rayleigh-Taylor instabilities at the collapse of bubbles is sometimes mentioned [1, 68, 30, 69, 31]. However, in the cases presented here, the bubble interface is smooth during the growth and collapse phase, which denotes the absence of instabilities developing on the interface.

Although we were able to highlight the effect of the pressure gradient on the collapse of a cavitation bubble in a typical flow, the results remain qualitative. The pressure field is estimated with a numerical simulation of the flow without bubble. The influence of the bubble on the flow is not known. The pressure experienced by the bubble interface is not necessarily the pressure calculated in the liquid for the case of the flow without a bubble. A calculation of the pressure on each point of the bubble interface as a function of time is thus not possible.

The observations show that, unlike in the case of a bubble collapsing close to a solid surface in water at rest, the microjet is not directed towards the solid surface, but take the direction opposite to the pressure gradient. This might be a clue for understanding the erosion potential of cavitation in the hydraulic machines. Indeed, the occurrence of cavitation in a machine does not systematically imply severe erosion. We could imagine that if the microjet developing at the collapse is deviated and does not hit the solid surface perpendicularly, the pressure on the surface is decreased. Therefore, the erosion potential would depend on the pressure gradient at the location of the collapse of the bubble. This effect could even be considered during the design of the machine, in order to minimize the potential erosion issues.

These encouraging results reveal the need for a quantitative investigation of the effect of the pressure gradient on the collapse of a bubble. Therefore, we had to think about a new experimental setup, where a bubble is subject to a constant pressure gradient, whose intensity can be modified at will. The solution we adopted is to generate a bubble in a liquid at rest, subject to a hydrostatic pressure gradient, whose intensity is modified by changing the gravity level experienced by the liquid. This allows a systematic investigation of the effect of the pressure gradient on all the collapse channels, namely the rebound, the microjet, the shock waves, and the luminescence. The setup is described in the next chapter, and the results are presented in the remaining part of the thesis.

4 Experimental setup for the collapse of a bubble in a hydrostatic pressure gradient

4.1 Spherical symmetry broken by the hydrostatic pressure gradient

Although many studies on cavitation consider bubbles as spherical, it is impossible to generate a perfectly spherical cavitation bubble in a liquid at rest subject to gravity. Gravity induces a hydrostatic pressure gradient in the liquid which influences the dynamics of cavitation bubbles. When the bubble grows and collapses in such a pressure field, the top of the bubble experiences a lower pressure than its bottom due to the difference of liquid height above the two locations on the bubble. From the generation until the maximum radius of the bubble is reached, the expansion of the bubble is more refrained on the lower half of the bubble than the upper half of the bubble. The shape of the bubble is therefore not perfectly spherical at maximum radius. The bottom of the bubble is flattened close to the bubble center compared to the top, as sketched in Fig. 4.1 (a). The same process occurs during the collapse of the bubble. As the bubble shrinks, the lower half of the bubble moves faster than the upper half. The bottom of the bubble reaches the center of the bubble first, as in Fig. 4.1 (b). The asymmetry of the pressure forces during both the growth phase and the collapse phase leads to a collapse that is not spherically symmetric.
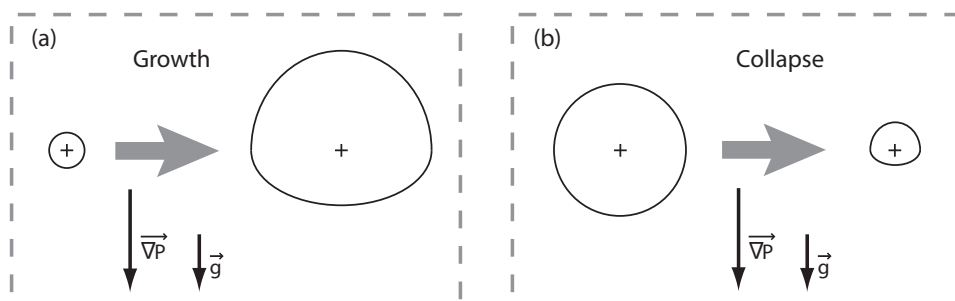
Figure 4.1: Sketch of the shape of an initially spherical bubble after (a) growing, and (b) collapsing in a liquid subject to a hydrostatic pressure gradient.

For our experimental purpose, we would like to vary or remove the intensity of the hydrostatic pressure gradient in order to identify and quantify its effect on the collapse of a bubble. Such conditions can be obtained in principle by varying the gravity level acting on the liquid, to the limit of canceling the own weight of the liquid, which results in the situation of weightlessness. One way of doing that is to run the experiment onboard a special aircraft performing parabolic flights. This aircraft follows parabolic trajectories, with the result of generating different stable levels of gravity during 20 s, from 1.8 g to 0 g. In consequence, one can study cavitation bubbles generated in "normal" gravity, hyper gravity (gravity between 1g and 1.8g), and microgravity ($\simeq$ 0g). Note that in microgravity, the pressure in the liquid is uniform, thus the pressure forces on the bubble are spherically symmetric. The situation is of particular interest since most theories strictly apply to perfectly spherical bubble collapses.

4.2   Parabolic flights

One way to vary the gravity level experienced by an object is to apply accelerations in addition to the gravitational acceleration. It is this principle that is used in parabolic flights. An aircraft performs specific manoeuvres in order to produce a vertical acceleration to counterbalance or accentuate the gravitational acceleration. It is then possible to run experiences at different levels of gravity. For our experiment, we generate laser-induced bubbles with an experimental setup placed in an aircraft performing those parabolic flights. Bubbles were observed in microgravity (acceleration of 0g), hypergravity (acceleration $\in$ [1.2g; 1.8g]), and earth gravity (acceleration of 1g). The results allow to identify the effect of the variation of the intensity of the pressure gradient on the collapse of the bubbles.

The parabolic flights are organized by the European Space Agency (ESA). A specially modified aircraft (Airbus A300-zeroG) performs the parabolic manoeuvres to provide weightlessness to the experiments onboard. Figure 4.2 shows one parabolic manoeuvre. After 120 seconds of horizontal flight, the aircraft smoothly climbs and pulls up its nose to an angle of 47 degrees. This phase lasts around 20 seconds during which the aircraft experiences an acceleration of 1.8g in the direction perpendicular to the trajectory. The thrust is then suddenly reduced to the minimum needed to compensate the drag of the aircraft. The aircraft is meticulously piloted to follow as closely as possible a free-fall ballistic trajectory, i.e., a parabola, for 20 seconds. During this phase, all forces applied on the aircraft compensate, and no forces are exerted on the content of the aircraft. The sensation of weightlessness is achieved. The parabolic manoeuvre ends with a pull out phase where the nose of the aircraft is lifted from an angle of 42 degrees back 0 degree, and thus to horizontal flight. The pull out phase lasts 20 seconds during which an acceleration of 1.8g is experienced. During a typical flight day, the parabolic manoeuvre is repeated 31 times. Longer breaks are planned every five parabolas, as illustrated on Fig. 4.3. At the end of the 31 parabolic manoeuvres, the aircraft performs six steep turns during which stable hypergravity is achieved. 15 to 20 seconds are usually needed to stabilize the aircraft from the horizontal flight. The hypergravity phases last about 60 seconds and the gravity level reached are 1.2g, 1.4g, and 1.6g. The results presented in this thesis were obtained

during the 53rd ESA parabolic flight campaign. One campaign offers three consecutive days of flight.
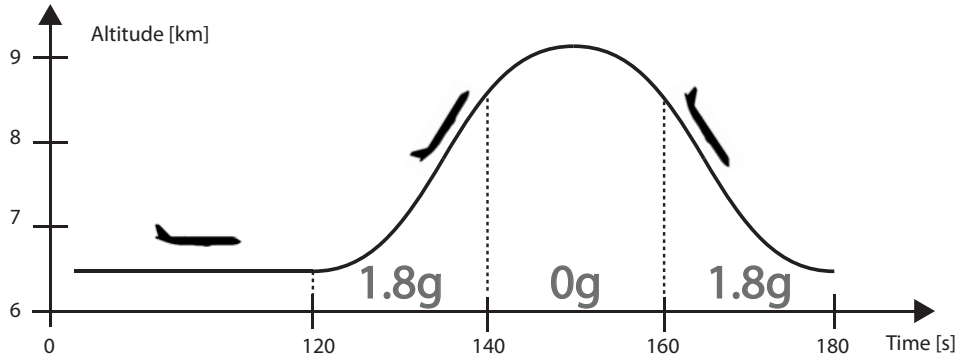
Figure 4.2: The typical parabolic manoeuvre, during which weightlessness is achieved.
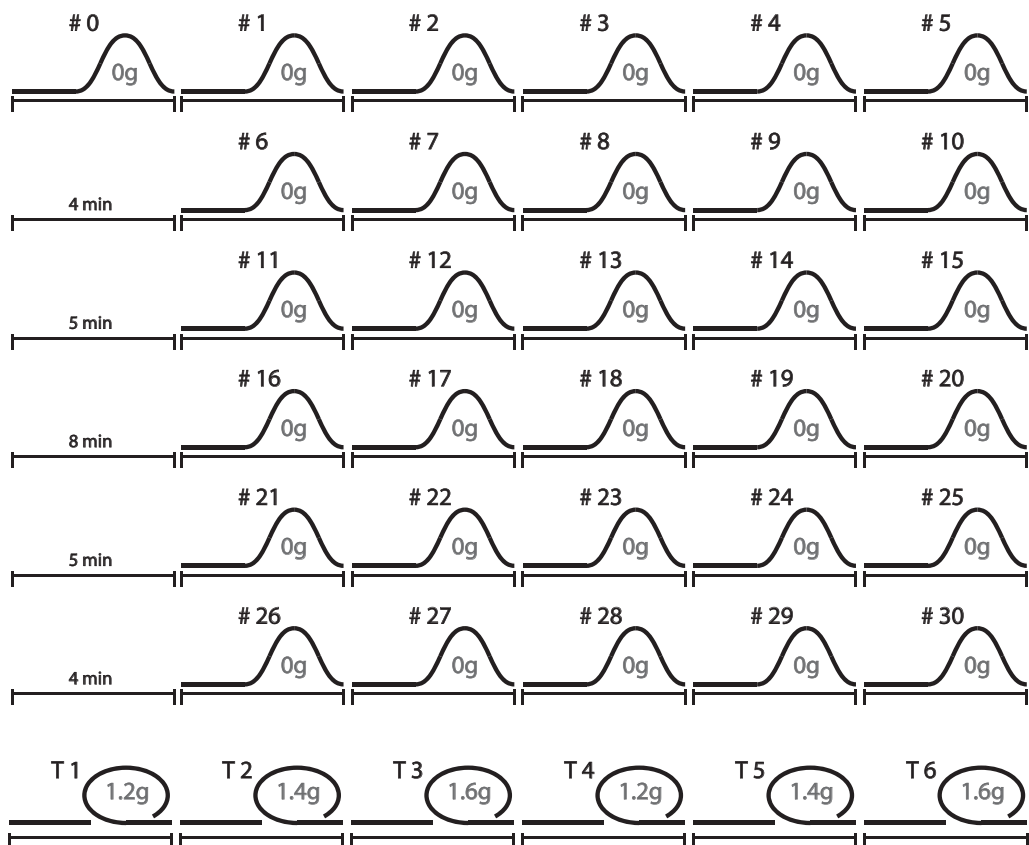
Figure 4.3: The Typical flight profile for one day of flight: a succession of 31 parabola, with breaks every five parabolas, concluded with six turns.

Chapter 4. Experimental setup for the collapse of a bubble in a hydrostatic pressure gradient

Figure 4.4 shows (a) the flight altitude of the aircraft, and the g-level in (b) the vertical direction $\overline{g_z}$ and the two horizontal directions (c) $\overline{g_x}$, and (d) $\overline{g_y}$. Each curve is the average over the 31 parabolas of one typical parabolic flight. The shaded area around the curves is the standard deviation σ. Note that the mean altitude during the stationary flight (during the first 60 s.) might change from one parabola to another. The pilots adapt the altitude to avoid turbulence zones. Therefore, we calculate the σ for the altitude relatively to the initial altitude of the stationary flight of the parabola. The fluctuation of the mean g-level in the vertical direction during the microgravity period is small: $\overline{g_z} \in [-0.01g, +0.02g]$ with a maximum standard deviation of 0.02g. The typical g-jitter for one parabola is < 0.03g at typical frequencies of 1-10 Hz. The duration of the phenomena we observe are of the order of the millisecond. The fluctuations of the g-jitter are thus too slow to affect our observations. Regarding to the values of the fluctuation of $\overline{g_z}$, we could argure that what is called "microgravity" phases should actually be called "centi-gravity" phases.

The g-levels, recorded for each turn of the campaign, are shown in fig. 4.4: (f) is g-level in the vertical direction $\overline{g_z}$, (g) in the horizontal directions $\overline{g_x}$, and (h) in the horizontal directions $\overline{g_y}$. The mean duration of a turn is 60 seconds. However, we observe that the duration can vary from one case to another, from 44 seconds for the shortest, to 120 seconds for the longest. The mean g-level and its standard deviation for each turn is given in tab. 4.1. All the standard deviations are < 0.03g.

	g_z:	g_x:	g_y:
1.2g turn :	1.220 ± 0.011	0.029 ± 0.003	0.014 ± 0.003
1.4g turn :	1.418 ± 0.013	0.057 ± 0.006	0.018 ± 0.003
1.6g turn :	1.612 ± 0.022	0.063 ± 0.009	0.019 ± 0.003

Table 4.1: The mean g-levels recorded during the stabilized hypergravity turns, along with the standard deviation.
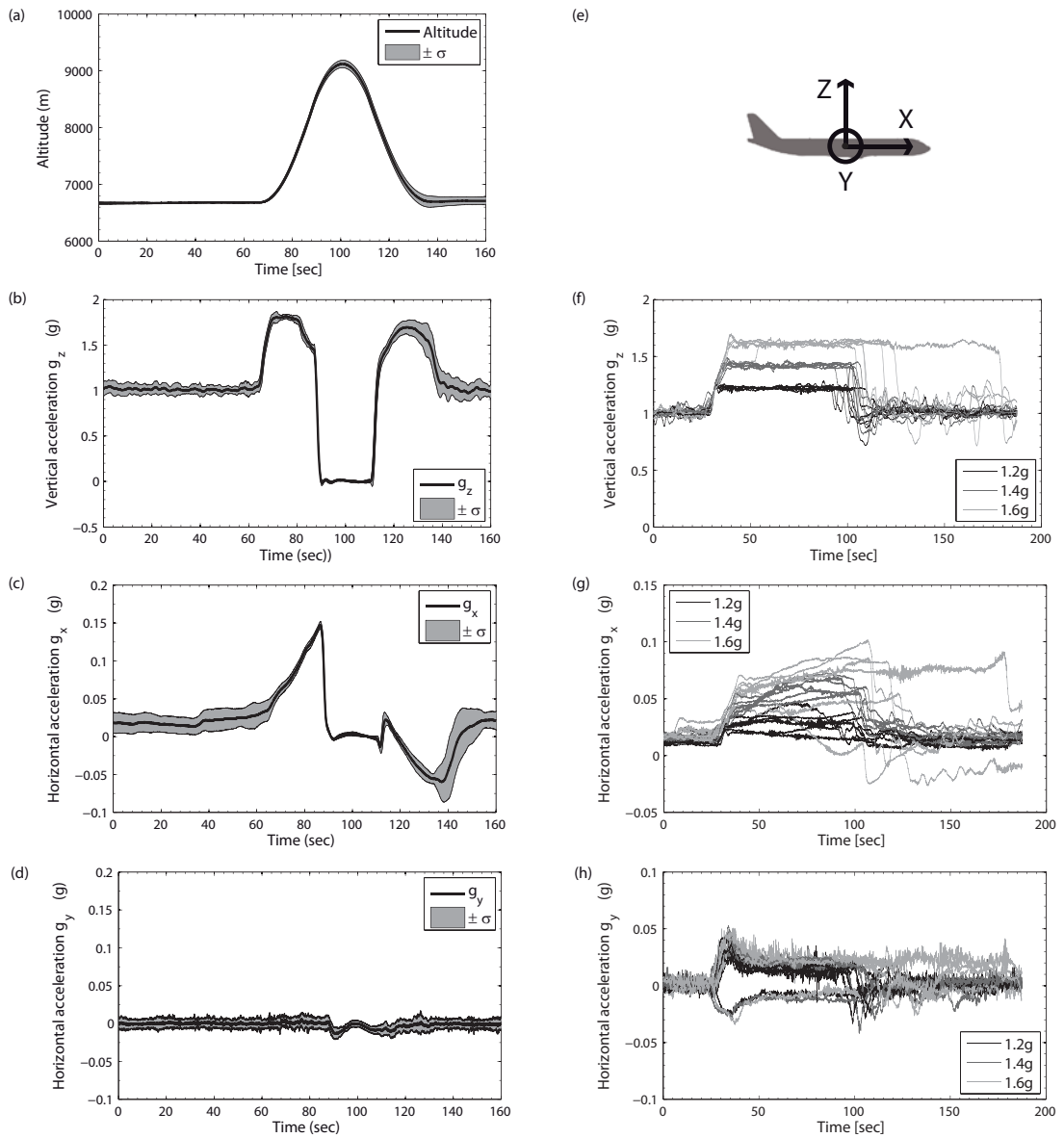
Figure 4.4: Plots of (a) the flight altitude of the aircraft, and the g-level on three directions (b) $\overline{g_z}$, (c) $\overline{g_x}$, and (d) $\overline{g_y}$, averaged over the 31 parabolas of one typical parabolic flight. The shaded area around the curves is the standard deviation σ. (e) The direction of the reference axis in the plane. (f)-(h): Measurements of the accelerations during the hypergravity turns in the three directions (f) g_z, (g) g_x, and (h) g_y.

4.3   Experimental bench

4.3.1   Design of the experimental bench

A new experimental setup has been built for the observation of bubbles onboard the zero-g aircraft. The science of the bubble generation has been acquired through tests in water at rest, and from the experiments in the cavitation tunnel. The knowledge on microgravity experimentations has been brought by the input of collaborators having experience on parabolic flights. A first experimental setup from the LMH had participated in parabolic flight campaigns in 2005 and 2006 [37, 70]. The experimental bench has been designed, mounted and tested at the LMH in less than four months. It has been specially designed to be used both in the laboratory on earth, and in the aircraft during the parabolic flights, for the observation of the collapse of laser-induced cavitation bubbles in a liquid at rest. What we expect from the experimental bench is (1) to record high speed movies of the bubble dynamics, (2) to measure the pressure fluctuations in the liquid due to the propagation of the shock waves, (3) to vary the pressure in the liquid, and (4) to measure the experimental condition at the moment of the generation of the bubble. The equipment needed to fulfill these requirements has to be fixed on an experimental bench that satisfies all the security constrains imposed for the parabolic flight. Note that a thorough description of the setup can also be found in [71].

Most design decisions are dictated by practical and security constraints. The width of the experimental bench is fixed to 780 mm, which allows the bench to go through standard doors when moved form the lab to the plane. The experimental bench is fixed on the floor of the plane on seat track fittings. The limit on the linear load for one seat track is 100 kg/m. As the weight of our experimental is 250 kg, the bench had to be fixed on three seat tracks. In consequence, the length of the base plate of the bench is set to 1580 mm. The bench is separated in two levels, as shown in Fig. 4.5. On the first level, all the electric and electronic components are fixed. The second level is a box containing all the experimental equipment. The height of each level is fixed at 400 mm. A laptop and the control box for the laser are fixed on the top of this box. In case of hard landing, the experimental bench and any equipment fixed on it are designed to support the accelerations listed in Tab. 4.2. The sections of the beams constituting the structure of the bench and all the fixation systems for the component have to be chosen in consequence. Mechanical calculations for the structure are performed, taking into account the weight and the position of each component on the bench.

Aircraft axis :	+X	-X	+Y	-Y	+Z	-Z
Hard landing load :	9 g	1.5 g	3 g	3 g	4.2 g	7.3 g

Table 4.2: Maximum acceleration, for each direction, to be supported in case of hard landing of the aircraft. All the equipment fixed on the plane or on the experimental bench has to stand these accelerations without breaking or detaching.

The main experimental components to be placed on the bench are:

- a vessel for the liquid
- a laser
- a high speed camera
- a dynamic pressure sensor
- an oscilloscope
- a set of sensors to measure the experimental conditions

The experimental equipment in the second level of the bench is arranged as shown in Fig. 4.6, in order to optimize the spacing on the bench. We put a box around the second level in order to satisfy two constrains: (1) the laser has to be confined, and (2) the liquid has to be double confined. (1) For security reasons, the laser has to be confined and secured. By putting all the experiment in the box, we ensure that no laser light will be emitted or reflected outside of the box. The lid of the box is connected to a switch so that the laser is shut off when the box is open. There is thus no risk for the laser to reach somebody or something outside of the box. (2) When large quantity of liquid is used (>0.5 L), the liquid has to be double-confined. If the first container breaks, the second prevents the liquid to float through the plane in microgravity phases. The liquid could reach other experiments in the plane, causing all sort of damages such as undesired chemical reactions or electric malfunctions. In our experiment, the first container is the vessel, and the second container is the level two box, around all the equipment.
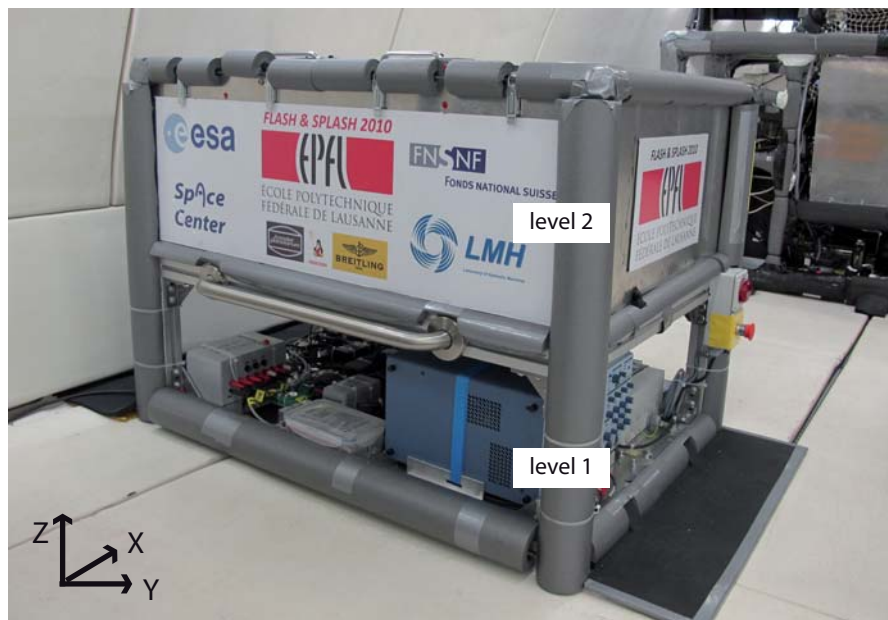
Figure 4.5: Picture of the experimental bench onboard the A300 zero-g aircraft. The two levels are shown, together with the XYZ axis of the plane.
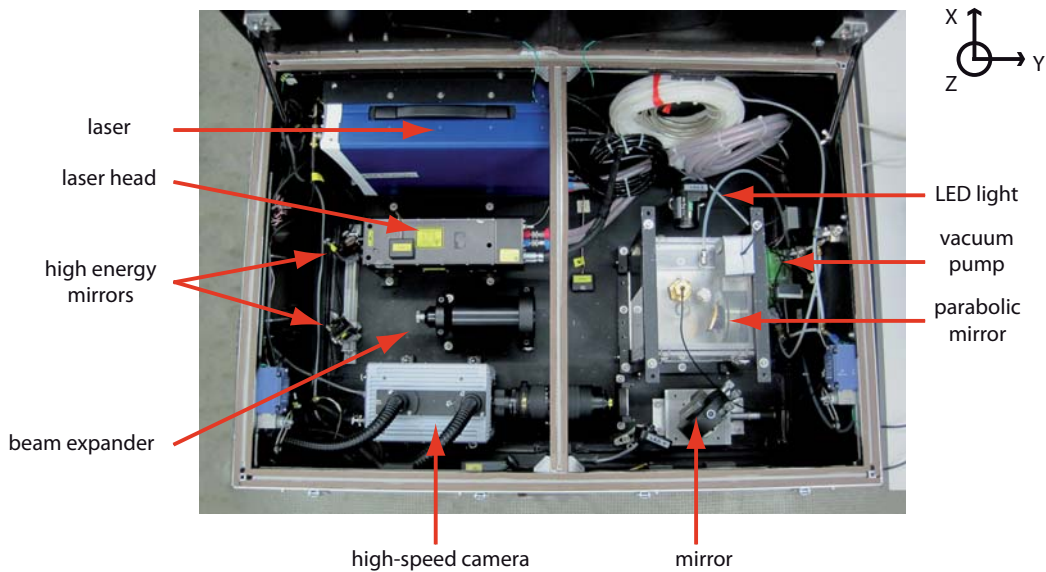
Figure 4.6: Picture of the equipment inside the experimental bench.

4.3.2   Control and automatization of the experimental bench

Once in microgravity, it is almost impossible for the experimenters to interact with the experiment. They are floating around the experimental bench, trying not to drift too far. Therefore, it is necessary to have a setup able to detect the beginning of the microgravity phases, and able to run a sequence of experiments and acquisitions during one parabola without any interaction with the experimenters. In the case of our experiment, we want to generate laser-induced bubbles during the microgravity phase, the hypergravity phase and the earth gravity phase within one parabola cycle. The dynamics of the bubble will be recorded with the high speed camera, and the shock waves monitored with the dynamic pressure sensor. In addition, for each bubble, we also want to know the exact experimental conditions such as the gravitational acceleration, the static pressure in the liquid, the temperature in the liquid, or the energy of the laser. All these data have to be saved on the laptop between two parabolas, classified in one folder per cavity generated. The control and the synchronization of all measurements are performed with a Labview program, from the laptop fixed on the top of the experimental bench.

The two "dynamic measurements" that lead to the largest files to handle are the high-speed camera movies and the dynamic pressure measurements. The high speed movies are recorded using a software (Photron Fastacm Viewer) edited by the manufacturer of the camera (Photron). During one parabola, the necessary movies are recorded and stored on the memory of the camera. At the end of the parabola, one experimenter saves these movies, transferring them from the camera to the laptop through an ethernet connexion. For the pressure measurements, one signal per bubble is acquired with the oscilloscope (Lecroy). Each signal is transferred and

saved automatically on the laptop through an ethernet connection. The rest of the information on the experimental conditions, gathered by static pressure sensors placed on the bench, is saved within one log file, and the log file for each bubble is saved in the same folder as the one containing the file of the pressure signal.

The Labview program for the control of the experimental bench has two distinct parts: an acquisition part, and a control part. The first part is to gather information about the general state of the experimental bench, and to acquire data about the experimental conditions from static sensor. The following static sensors are placed on the experimental bench. All the sensors are calibrated by the manufacturer. The experimental conditions are within the calibration validity range, except for the static pressure sensor in the vessel. This sensor is therefore tested and calibrated to be used in our whole range of conditions (see appendix A.2). The sensors are listed below:

- one accelerometer, for g-level (Phidget #1059)
- one static pressure sensor, for ambiant pressure (Phidget #1112)
- one static pressure sensor, for pressure in the vessel (Phidget #1112)
- one thermometer, for ambiant temperature (Phidget #1124)
- one thermometer, for temperature on the surface of laser head (Phidget #1124)
- one thermometer, for temperature in the water (Redfish, DirecTemp DTU6024C)
- two light sensors, for light or laser leakage (Phidget #1115)
- one proximity sensor, for the position (open/close) of the the lid (Phidget #3562)
- one current sensor, for the electrical current provided to the setup (Phidget #3500)

The second part of the program is written as to control the pressure in the vessel and to start an acquisition sequence when the program detects the beginning of a parabola. Before each parabola, the experimenter has to enter in the Labview program: the pressure in the vessel, the number of bubbles to generate in 0g, 1.8g and 1g, the energy set on the laser and the type of lighting used. The pressure in the vessel is then controlled by a vacuum pump (Parker BTC-IIS, Brushless Motor) connected to the vessel. The pump is switched on and off such as to adjust the pressure in the vessel with the prescribed pressure. The acquisition for one bubble works as follow. The program controls a relay that sends a TTL signal to the laser and the laser pulse is generated. When the laser pulse is released, a TTL signal is sent from the laser to the high-speed camera and to the oscilloscope, and the recording and acquisition begin. At the same time, the values of the static sensors about the experimental conditions, i.e. the temperature in the liquid, the pressure in the vessel, and the gravitational acceleration are saved in one log file. The program recognizes the different phases of the parabola. It starts the 0g acquisitions when the vertical acceleration is zero for 2 seconds. Once the 0g acquisition is performed, it waits until the vertical acceleration exceed 1.2g for two seconds, which means the plane is in the pull out phase. After the pull out phase, when the vertical acceleration becomes equal to 1g for two seconds, the 1g acquisition starts and followed by the end of the

sequence. Back to 1g, the experimenters can now adjust the experimental parameters for the next parabola. The electrical schematic in Fig. 4.7 gives an overview of how the different components are connected and controlled.
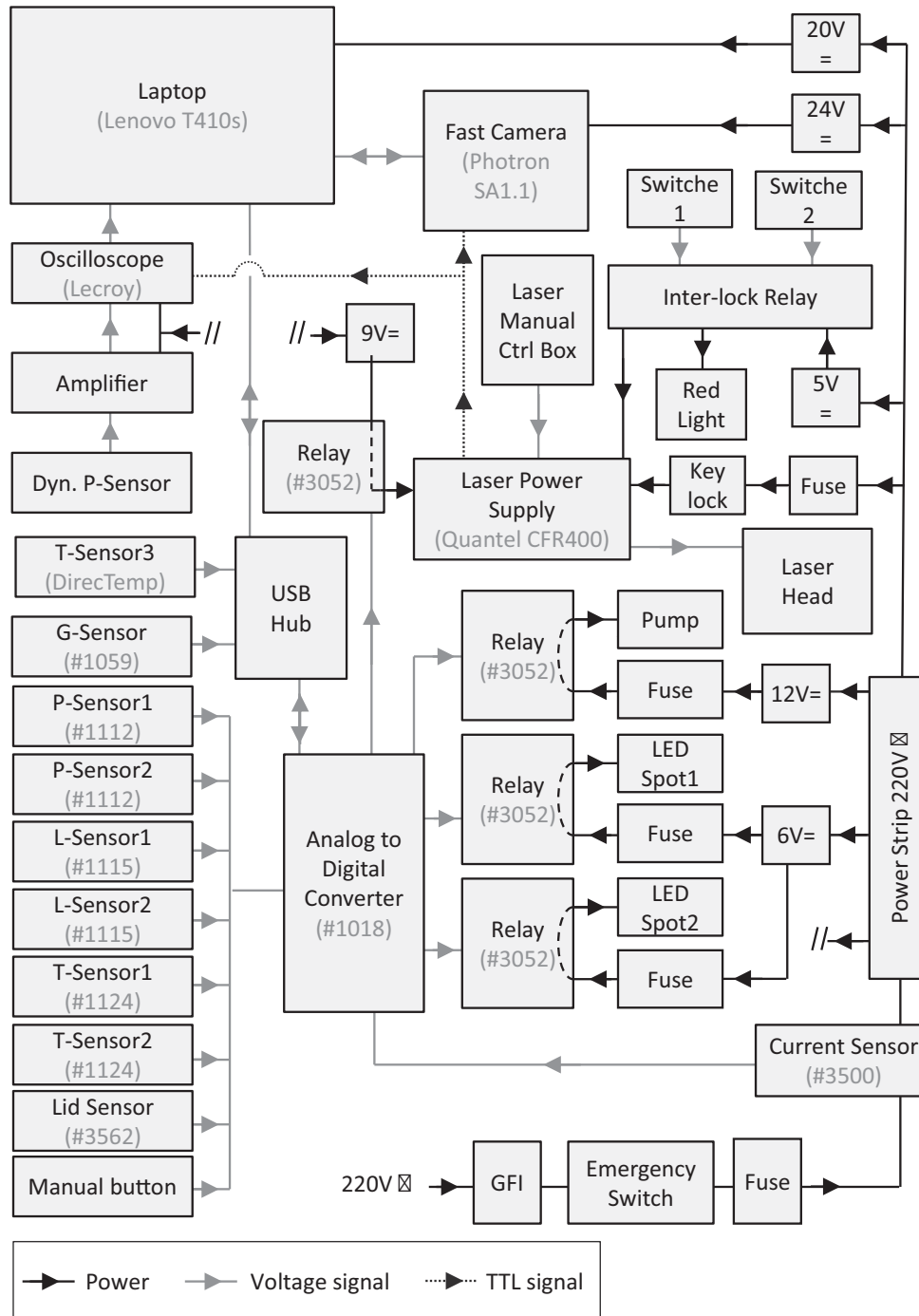
Figure 4.7: Electrical schematic of the experimental setup.

4.4 Laser technique with innovative optics

The experimental bench is developed to generate highly spherical cavitation bubbles in order to identify and quantify the faint effect of gravity on the collapse of the bubble. The effect of gravity on the cavitation bubble is supposed to slightly deform the bubble, leading to an asymmetric collapse. Therefore, it is primordial to avoid any source of asymmetry, except gravity, when the bubbles are generated. In particular, attention has to be pay on the focussing of the laser into water. The key to obtain spherical cavitation bubbles with a laser is the shape of the initial plasma. The vapor bubble grows from the plasma. Therefore, an asymmetry of the plasma leads to an asymmetric bubble. Even if this asymmetry might not be visible during most of the bubble lifetime, due to the large expansion of the radius, it still affects the last stage of the collapse. This mechanism has actually already been used to obtain specific non-spherical collapse geometries by tuning the shape of the initial plasma [17]. Under these circumstances, it becomes obvious that we need to generate a small, spherical, compact plasma in order to obtain highly spherical cavitation bubbles. The best way to generate such a plasma is to focus the laser with a large convergence angle. Indeed, with the large angle, the volume where the energy density of the laser exceeds the breakdown threshold is small.

The cavitation bubbles are obtained by focussing a high energy laser in water (Fig. 4.10). The water is contained in a $228.6 \times 228.6 \times 241.3$ mm acrilic vessel (Terra universal vacuum chamber type C). The laser source is a Q-switched Nd:YAG laser (Quantel CFR 400) delivering pulses up to 230 mJ and 8 ns duration at a wavelength of 532 nm. The laser pulse of 7 mm in diameter is increased 10 times through a galilean beam expander before being focussed. The energy of the laser pulse is controlled by changing the delay between the beginning of the flash lamp pumping and the release of the pulse by Q-switching. We call this delay the Q-switch delay. The mechanism is the following: As long as the flash lamp is pumping, the energy in the laser head cavity is increasing. When pumping stops, the energy is slowly absorbed by the YAG rod in the cavity. If Q-switching happens before all energy is absorbed, the energy in the cavity is released in the form of a short laser pulse. For the laser used in our experiment, the nominal Q-switch delay, leading to the highest energy, is 170 μs. If this delay is increased, more energy is absorbed, and the output energy is lower. The conversion from Q-switch delay to laser energy output is non-linear. Figure 4.8, shows measurements of the laser energy as a function of the Q-switch delay. The energy of the laser is measured inside the vessel, without water. One can wonder how much of the laser energy is transferred into the bubble. Figure 4.9 shows the calculated potential energy in the generated bubble E_{pot} as a function of the energy of the laser pulse, $E_{pot} = 4/3\pi R_{max}^3 (p_\infty - p_v)$, where R_{max} is the bubble maximum radius, p_∞ is the pressure in the liquid, and p_v the vapor pressure. The least square linear regression on the data gives a fraction of 8.7 % of the energy transferred from the laser into the bubble. In comparision, Robert *et al.* [38] found 7.3 %, while Vogel *et al.* [72] found fractions between 11 % and 30 %, depending on the characteristics of the laser used. The rest of the energy is transferred into light reflection, scattering, and transmission, plasma radiation, water evaporation and shock wave formation [72].
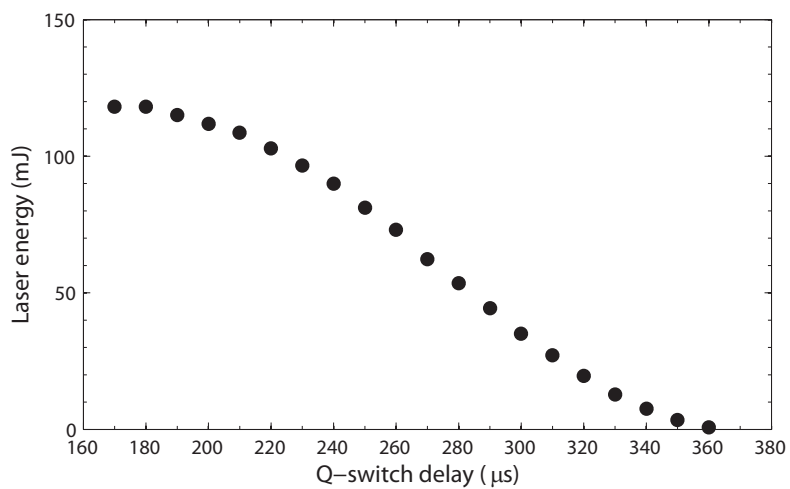
Figure 4.8: Measurements of the energy of the laser pulse as a function of the Q-switch delay.
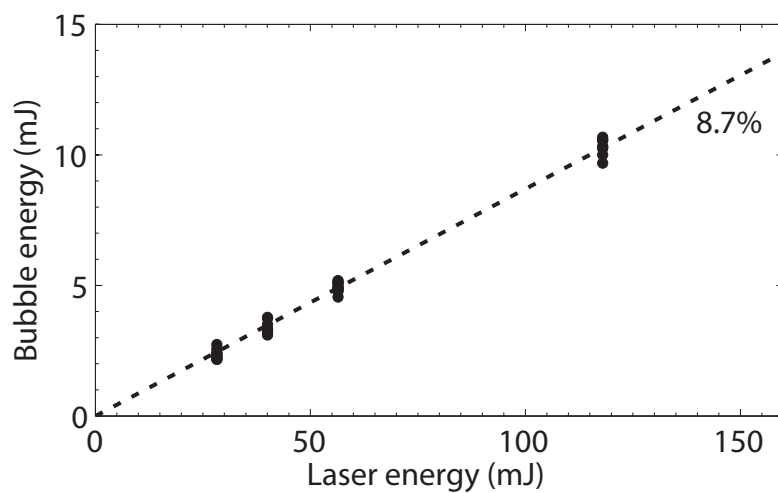
Figure 4.9: The potential energy of the bubble as a function of the energy in the laser pulse.
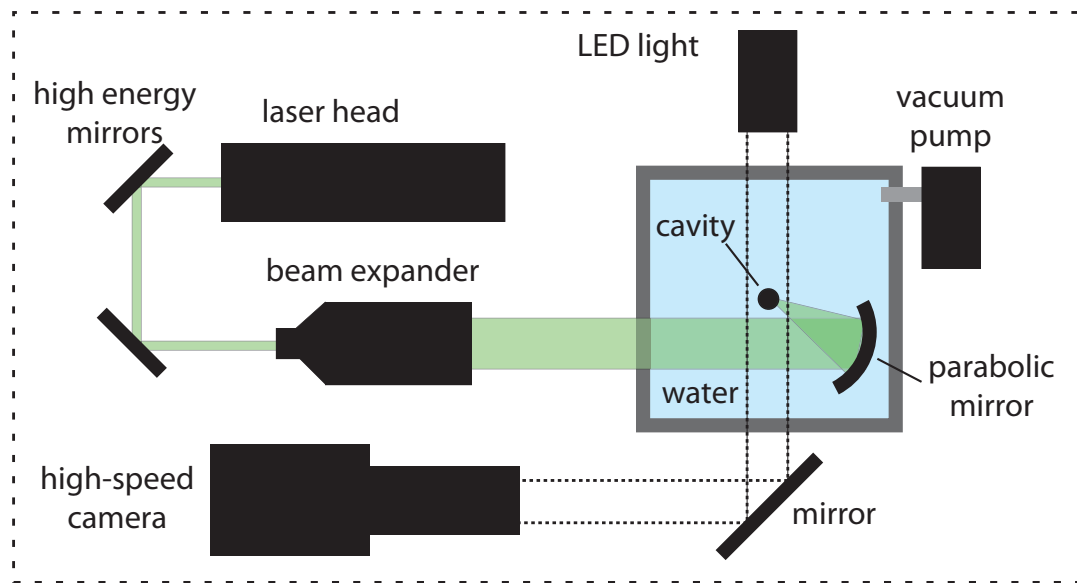
Figure 4.10: Sketch of the arrangement of the experimental setup on the second level of the bench.

The innovation in our the setup lays in the use of a parabolic mirror to focus the laser beam. To our knowledge, in all studies on optical cavitation (i.e. cavitation generated with a laser), a lens is used to focus the laser into the water. However, lenses are subject to refraction and spherical aberration issues. With a lens, the convergence is achieve by refraction when the beam travels through interfaces of a different refractive index. Since most lenses are designed to focus beams in the air rather than in water, the beam is not well focussed into water. The use of a parabolic mirror minimizes these issues of refraction and spherical abberation because the focussing is achieved by reflection on the surface of the mirror. The quality of the focussing is thus improved compared to what is achieved with a lens. Figure 4.11 shows the plasma obtained using: a) 54.5 mm parabolic mirror, b) 76.5 mm converging lens and c) 100 mm converging lens. The plasma looks indeed more spherical and compact with the mirror than with the lenses. In addition to these physical considerations, we note that the manufacture of mirrors with a large diameter and a short focal distance (which leads to large convergence angle) is more common than lenses with the same characteristics.
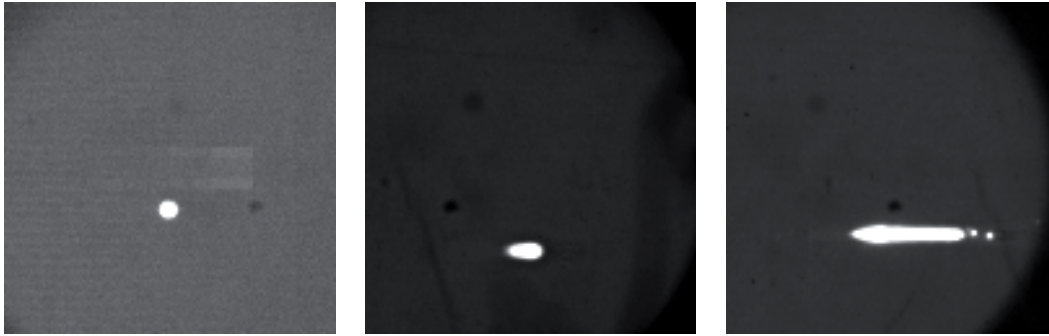
Figure 4.11: Images of the plasma generated using: a) 54.5 mm parabolic mirror, b) 76.5 mm converging lens and c) 100 mm converging lens.

After debating the benefits of the parabolic mirror, it is legitimate to wonder why we do not use a mirror to focus the laser pulse in the case of the bubbles in the cavitation tunnel. Two reasons arise. First, it is simply not possible to place a mirror in the test section without disturbing the flow. Second, we did not found how we could reach such flexibility for the location of the bubble generation with a design using a focussing mirror outside the test section. The concession on the sphericity of the bubble is therefore counterbalanced by the flexibility of the system. In any case, in our experiments in the cavitation tunnel, the pressure field in the flow has a significant influence on the dynamics of the bubble. The slight non-sphericity induced by the focussing of the laser through the lens is then negligible.

4.5   High-speed imaging and image processing

The collapse of cavitation bubble is a short event. The lifetime of the bubbles we observe is between a few microseconds and a few milliseconds. There is impossible to record a sharp movie of the bubble dynamics using a standard camera. In consequence, we observe the bubble with a high-speed camera (Photron Fastcam SA1.1). The camera records at a rate of up to 675,000 frames/s with a minimal exposure times as short as of 370 ns. With short exposure times, the light needed to observe the phenomenon is important, and special care has to be taken to obtain good images. Two methods were used to illuminate the bubble. The first method was to illuminate the bubble from the back and to visualize it by shadowgraphy. A compact 3W LED lamp with a small opening angle of 6° is used to illuminate the bubble from the back. The light reaches almost perpendicularly the CCD sensor of the camera. The bubble appear in black on a clear background (figure 4.12 a)). With this method, shock waves can also be observed when the exposure time is short enough (i.e. camera set at 370 ns). The drawback of this method is that, as we see the shadow of the bubble, the detail of the bubble-liquid interface are not visible. The second method is to use two 800 W halogen lamps, one on the front and one on the top of the water reservoir. With this method, the details of the bubble interface become visible as shown on figure 4.12 b). In this configuration, a lot of light is

needed to have a clear picture. The exposure time has to be longer than with the shadowgraphy method. The images when the interface is moving fast (i.e. frames of the generation and the very last stage of the collapse) are not as sharp as with backlight illumination, but irregularities and instabilities on the interface are visible. As the halogen lamps dissipate a lot of heat, this second method was not appropriate for the experiment in the plane because of fire or plastic melting issues.
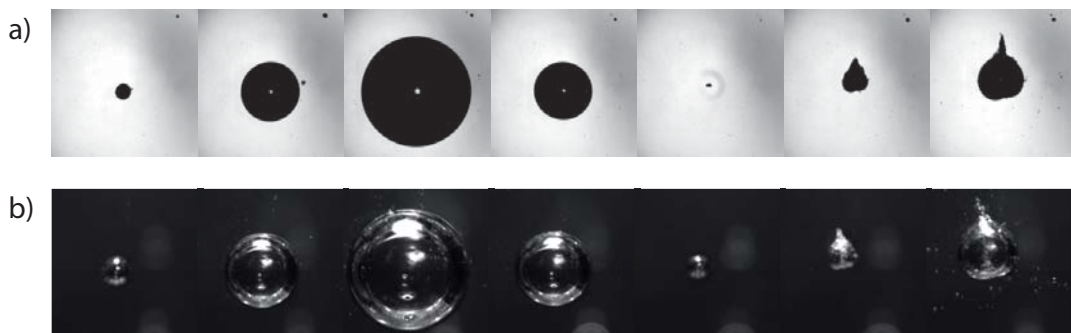
Figure 4.12: High-speed images of the growth, collapse and rebound of a cavitation bubble. The bubble is illuminated a) from the back, i.e. shadowgraphy, b) from the front and the top. Note the apparition of the gravity-induced microjet at the rebound.

During the course of the flights, movies are taken with the high speed camera and the shadowgraphy illumination. The radius as a function of time is then extracted by an image processing detailed in figure 4.13. The image is binerized using a threshold function adapted to separate the bubble from the background. If there are parasite microbubbles on the frame, we suppress them by selecting only the bubble located at the center of the frame, where the bubble is generated. The volume of the bubble on the frame is calculated as the volume generated by the silhouette of the bubble on the frame when rotating around the vertical axis going through its center of gravity. The value for the conversion of pixels in milimeters is obtained by putting a reference object (a ruler, as shown in fig.4.14) at the location of the bubble generation. The volume in cubic pixels is then converted into cubic meters. By processing each image of the high-speed movie, and knowing the time between each frame of the movie, we obtain a measure of the radius as a function of time for the observed bubble. We obtained a spatial resolution of 69 μm per pixel, and a temporal resolution of 10 μs.
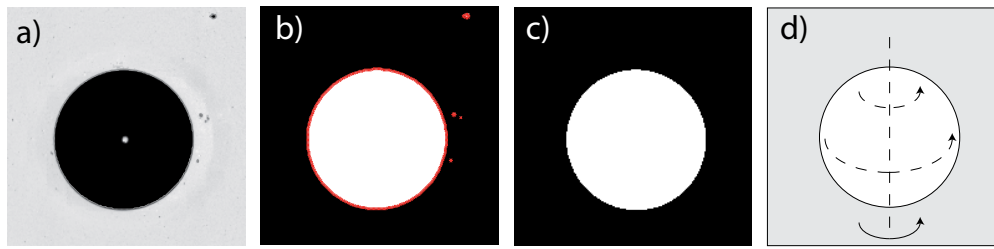
Figure 4.13: Processing of the high speed images to extract the volume of the bubble: a) original image, b) binerized image and contours detected, c) selection of the cavitation bubble, d) calculation of the volume by revolution of the 2D silhouette of the bubble.
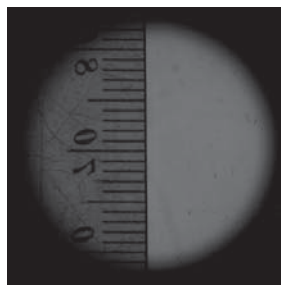
Figure 4.14: Picture of the ruler placed at the location of the bubble generation. The number of pixels per millimeter (14.5) is measured from this image.

For the analysis of rebound bubbles exhibiting a microjet, we are not only interested in the total volume of the bubble, but also in the volume of the microjet. Thus, for each of these bubble, the rebound bubble is decomposed into a disk and the microjet, as shown in figure 4.15 d). The contour of the disk, i.e. the spherical part of the rebound, is determined using a χ^2 fit of a circular function on the contour of the bubble. The limit between disk and jet (grey line on d)) is the top horizontal tangent on the frame. The volume of both the spherical part of the bubble V_{disk} and the volume of the jet V_{jet} are calculated as volume of revolution of the surface respectively below and above the limit.
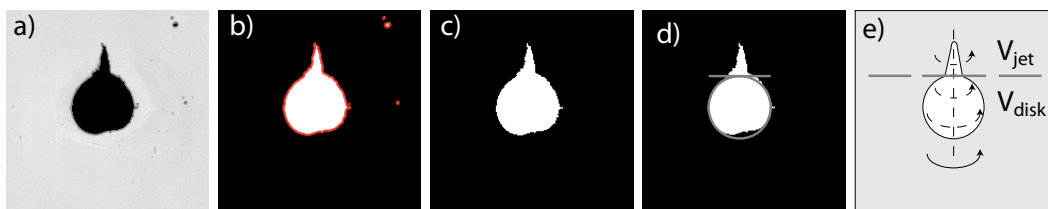
Figure 4.15: Processing of the high speed images to extract the volume of a rebound bubble with a microjet: a) original image, b) binerized image and contours detected, c) selection of the cavitation bubble, d) separation between jet and e) calculation of the volumes by revolution of the 2D silhouette of the bubble.

5 Gravity induced jets due to the hydrostatic pressure gradient

5.1 Simple model for the effect of gravity on the collapse of a bubble

The effect of gravity on the collapse of a cavitation bubble manifests itself as the presence of a hydrostatic pressure gradient in the liquid around the bubble. The pressure at one point on the bubble interface is a function of the depth in the liquid, as expressed in Fig. 5.1. The top of the bubble experiences the smallest pressure, while the bottom experiences the largest. In most studies, gravity is neglected. However, we demonstrate in this chapter that gravity can have a non-negligible effect. We exploit the hydrostatic pressure gradient to build case studies for the investigation of the effect of a pressure gradient on the bubble dynamics.

The effect of gravity can be illustrated with the following simplistic theoretical case study. We assume a perfectly spherical cavity in a liquid subject to earth gravity. We assume that the interface between the cavity and the liquid moves exclusively in the radial direction, and that the radial position of each point on the interface is given by the Rayleigh equation (Eq. 5.1), without interaction of one point on the other.

$$R\ddot{R} + \frac{3}{2}\dot{R}^2 = -\frac{p_\infty}{\rho} \tag{5.1}$$

where R is the radius of the cavity as a function of time, p_∞ is the pressure in the liquid, and ρ is the water density.

When the initial system is released from the initial conditions (given maximum radius R_{max} and initial interface velocity $\dot{R}(t=0)=0$) at a time t = 0, we observe the collapse of the cavity. However, because of the gravity, the cavity does not collapse symmetrically. The bottom of the bubble reaches the center of the bubble first. At this moment the cavity looks like an empty cardioid in the middle of the liquid. Figure 5.2 shows the result of such a calculation in two dimensions. The shape of the cardioid depends on the initial radius of the cavity, on the value of the gravitational acceleration, and on the pressure considered inside the liquid.

The shape of the cardioid is given by the position of the cavity interface at the time t = $\tau_{c,bottom}$,

where $\tau_{c,bottom}$ is the collapse time of the point at the bottom of the interface. As the position of each point is derived from the Rayleigh equation, the shape of the cardioid is the set of solution for $R = R(t = \tau_{c,bottom})$, where R(t) is the radial position, calculated for every interface point. The general form of the collapse time τ_c for a cavity of initial radius R_{max} is

$$\tau_c = 0.915 R_{max} \left(\frac{\rho}{p_\infty} \right)^{1/2} \tag{5.2}$$

In our case study, we consider a different pressure p_∞ for every point on the cavity interface. p_∞ becomes a function of the depth in the liquid. It is given by

$$p_\infty(\alpha) = p_{\infty,c} - \rho g R_{max} cos(\alpha) \tag{5.3}$$
$$\text{with} \quad p_{\infty,c} = p_{air} + \rho g h$$

where α is the angle between the vertical direction and the radial direction for the considered point, $p_{\infty,c}$ the pressure at the depth of the center of the bubble, p_{air} is the pressure in the air above the water, and h is the depth of liquid between the surface and the bubble center.
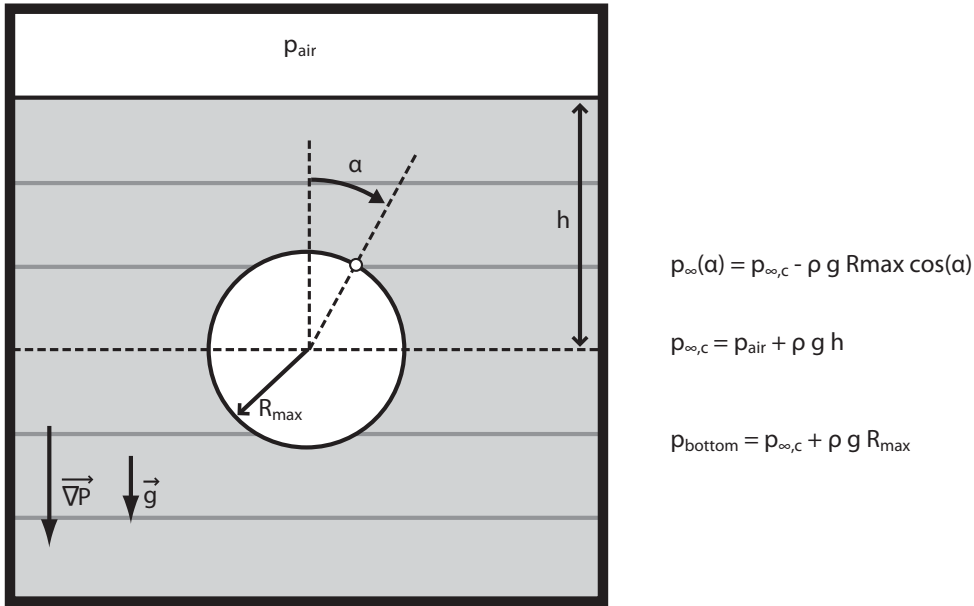
Figure 5.1: Sketch of a bubble within a vessel full on liquid subject to a hydrostatic pressure gradient.

Instead of solving numerically the Rayleigh equation to obtain R(t) for each point of the interface, we use the approximation for the Rayleigh collapse proposed by Obreschkow *et al.* [73], expressed in Eq. 5.4. This approximation provides a simple and explicit equation for the

normalized radius of the bubble R^* (radius divided by maximum radius) as a function of the normalized time (time divided by collapse time).

$$R^* = \frac{R(t)}{R_{max}} = \left(1 - \left(\frac{t}{\tau_c}\right)^2\right)^{0.4} \tag{5.4}$$

From Eq. 5.2, we obtain the collapse time $\tau_{c,bottom}$:

$$\tau_{c,bottom} = 0.915 R_{max} \left(\frac{\rho}{p_{bottom}}\right)^{1/2} \tag{5.5}$$

where $p_{bottom} = p_\infty(\alpha = 2\pi) = p_{\infty,c} + \rho g R_{max}$.

Considering Eqs. 5.3, 5.4, and 5.5, the normalized positions $R^*(\tau_{c,bottom})$ become

$$R^*(\tau_{c,bottom}) = \frac{R(\tau_{c,bottom})}{R_{max}} \quad = \quad \left(1 - \left(\frac{0.915 R_{max}\left(\frac{\rho}{p_{bottom}}\right)^{1/2}}{0.915 R_{max}\left(\frac{\rho}{p_\infty(\alpha)}\right)^{1/2}}\right)^2\right)^{0.4} \tag{5.6}$$

$$= \quad \left(1 - \left(\frac{p_\infty(\alpha)}{p_{bottom}}\right)\right)^{0.4} \tag{5.7}$$

$$= \quad \left(1 - \left(\frac{p_{\infty,c} - \rho g R_{max} cos(\alpha)}{p_{\infty,c} + \rho g R_{max}}\right)\right)^{0.4} \tag{5.8}$$

$$= \quad \left(\frac{\frac{\rho g R_{max}}{p_{\infty,c}}}{1 + \frac{\rho g R_{max}}{p_{\infty,c}}}\right)^{0.4} (1 + cos(\alpha))^{0.4} \tag{5.9}$$

$$\stackrel{Z = \frac{\rho g R_{max}}{p_{\infty,c}}}{=} \quad \left(\frac{Z}{1 + Z}\right)^{0.4} (1 + cos(\alpha))^{0.4} \tag{5.10}$$

$$\tag{5.11}$$

As long as the experimental conditions lead to a same value for Z, the normalized cardioid at the collapse is the same. Figure 5.2 (a) shows the cardioid obtained with $\rho = 1000 \text{ kg/m}^3$, $g = 9.81 \text{ m/s}$, $R_{max} = 1 \text{ mm}$, and $p_{\infty,c} = 100 \text{ kPa}$. (b) shows the cardioids obtained when g is multiplied by 2, when R_{max} is multiplied by 2, and when $p_{\infty,c}$ is divided by 2 with respect to the conditions taken in (a). The three cardioids superpose perfectly. We observe that when the value of the parameter Z increases, the size of the cardioid increases too, which suggests a larger asymmetry, and possibly a stronger microjet.
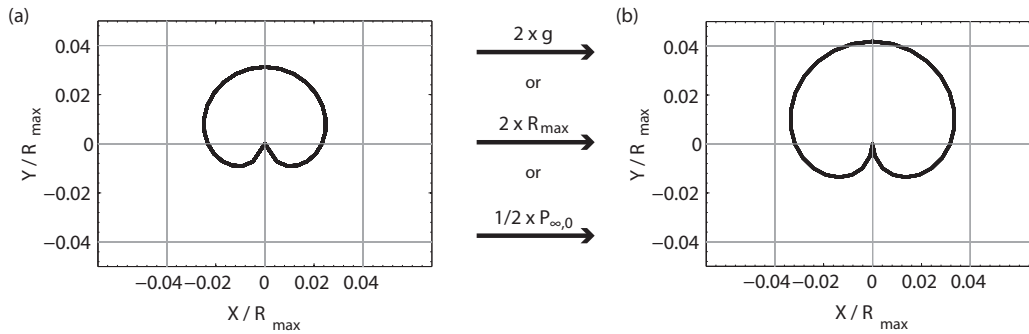
Figure 5.2: Theoretical shape of a spherical bubble collapsing in a liquid subject to a hydrostatic pressure gradient. (a) The reference case: $\rho = 1000$ kg/m^3, $g = 9.81$ m/s, $R_{max} = 1$ mm, and $p_{\infty,c} = 100$ kPa. (b) Superposition of the results where g is multiplied by 2, R_{max} is multiplied by 2, and when $p_{\infty,c}$ with respect to the reference case.

If we transpose this observation to the case of a laser-induced cavitation bubble, we expect the bottom of the bubble to reach the center of the bubble before the top. The liquid arriving from the concave bottom would advance into the bubble until it collides with the top interface of the bubble. Depending on the initial condition, if this asymmetry is large enough, this situation could lead to the formation of the microjet. Therefore, we suppose the microjet to scale with $Z = \rho g R_{max}/p_{\infty,c}$.

5.2 Effect of the experimental conditions on the gravity induced jets

In the course of the parabolic flights, bubbles are generated during the zero gravity, the hypergravity, and the normal gravity phases. With this three different levels of gravity, we can identify the effect of gravity by comparing the observations performed with gravity with the observations performed without gravity. We can also quantify the influence of the value of the pressure gradient using the two levels of none-zero gravity.

Figure 5.3 shows three bubbles of similar maximum radius $R_{max} \approx 5$ mm, generated in water at a pressure of $p_{\infty,c} \approx 10$ kPa, for three different gravity level: (a) 1g, (b) 1.6g, and (c) 0g. We observe, in agreement with the simple theoretical model presented in the previous section, the apparition of a vertical jet growing from the top of the rebound bubble in (a) and (b). However, no jet appears in microgravity (c). The disappearance of the jet in microgravity is a major result. It confirms that the jet we observe is caused by gravity. Indeed, the only difference in the physics of the collapse with or without gravity is a constant vertical pressure gradient applied on the bubble in the case with gravity, whereas in microgravity there is no pressure gradient in the liquid. Two main conclusions are drawn from this observation. First, under appropriate conditions, the gravity can cause the apparition of microjet at the collapse of a bubble. And second, that the microjet goes in the direction opposite to the pressure gradient. Although it is not the first time that a gravity-induced microjet is observed [24], the investigation performed

during the flight campaign provides the first systematic observations of the phenomenon.
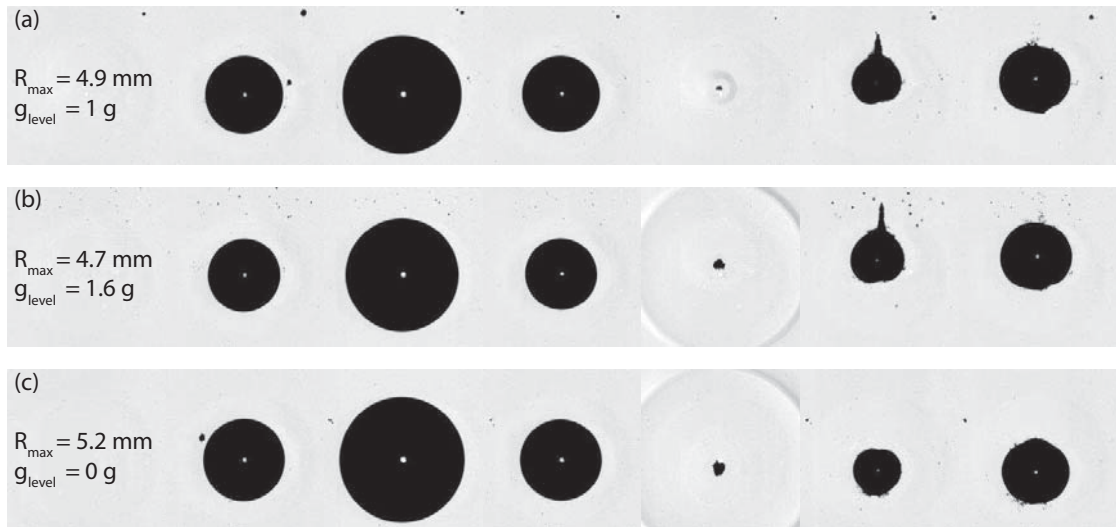
Figure 5.3: Three bubbles generated with the same laser energy, in a liquid with the same pressure on its surface, but at three different gravity levels g.
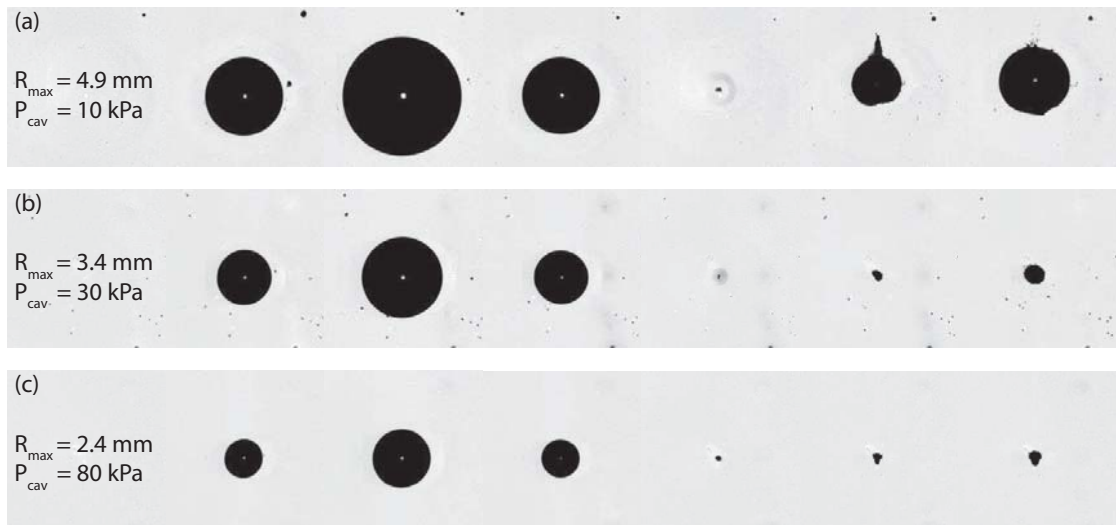
Figure 5.4: Three bubbles generated with the same laser energy, in normal gravity, but at three different pressures in the liquid p_∞.

Figure 5.4 shows three bubbles generated in normal gravity, with the same laser energy, at three different liquid pressures: 80, 30 , and 10 kPa. The pressure refereed here as the liquid pressure is the pressure at the depth of the bubble center $p_{\infty,c}$. Note that from now on, we will simply refer $p_{\infty,c}$ as p_∞, because $p_\infty(\alpha) \in p_{\infty,c} \pm 0.1\%, \forall \alpha$. In the case $p_\infty = 10$ kPa, we observe the apparition of a jet, growing vertically at the top of the rebound bubble. However, for $p_\infty = 30$ or 80 kPa, no jet is visible. The apparition of the jet is thus not systematic, which

implies the existence of a threshold for the apparition of the jet. We can already suspect p_∞ and R_{max} to be involved in the definition of the threshold.

We observe that the maximum radius of the initial bubble is different for each p_∞. This is explained by considering the energy in the bubble. The energy in the laser pulse is the same for each cases. The potential energy of the bubble, given by $E_{pot} = 4/3\pi R_{max}^3 (p_\infty - p_v)$, where p_v the vapor pressure, is actually also the same in the three cases. Therefore, a variation in the pressure p_∞ leads to a different bubble radius R_{max}. Note that the maximum radius of the rebound bubble, when normalized with R_{max}, also dependents on the pressure p_∞.

To determinate the effect of the pressure versus the effect of the maximum radius, we show on Fig. 5.5 three bubbles generated in normal gravity at the same pressure $p_{\infty,c} \approx 10$ kPa. We observe that the jet is longer and wider when the bubble maximum radius is larger.
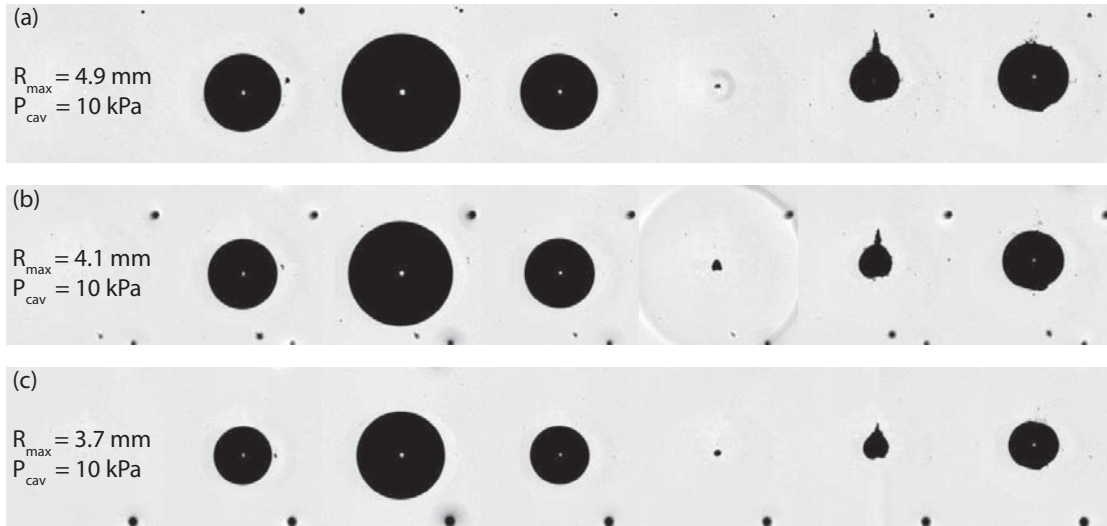
Figure 5.5: Three bubbles generated in normal gravity, with the same pressure in the liquid, but with three different laser energies, leading to three different bubble maximum radii R_{max}.

From these experimental observations, we draw the following conclusions:

- under appropriate conditions, gravity can induce the apparition of a jet at the collapse of the bubble
- the size of the jet increases when the gravity level increases
- the size of the jet increases when the maximum radius of the bubble increases
- the size of the jet increases when the pressure in the water decreases

The last three conclusions can be summarized as follow: The size of the jet increases when the value of $Z = \rho g R_{max}/p_{\infty,c}$ increases, independently of the cause for the variation of Z.

5.3 Scaling law for the volume of the jets

The high speed movies reveal a variation of the size of the jet when the experimental conditions are changed. We will show here that we can scale the size of the jet with the experimental conditions, using a phenomenological approach. To quantify the variation of the size of the jet, we first need to define what we mean by "size". The representation of the different constituents of the jet, and the corresponding variables, is given in Fig. 5.6. The rebound bubble is decomposed, as explained in section 4.5, into a disk of radius R_1, and a jet (vapor + liquid) of volume V_{jet}^*. Since the microjet starts at the bottom of the bubble, we extend the volume V_{jet}^* into the bubble to obtain an effective jet V_{jet}. The relation between V_{jet}^* and V_{jet} depends on the angle of the conical jet ϕ. This angle is measured along the edges of the jet when its volume is maximum V_{jet}^{*max} from the high speed movies taken during the parabolic flights. We obtain $\phi \approx 4°$ for all jets. By trigonometry, Eqs 5.12 - 5.13, we obtain the extended jet volume V_{jet}^{max} as a function of the jet volume $V_{jet}^*{}^{max}$ and the radius of the bubble R_1. Finally, the "size" of the jet is defined as the "normalized jet volume" ϵ_{jet} in Eq. 5.14.

$$V_{jet}^{*max} = \frac{\pi}{3}\left(d\,tan(\phi/2)\right)^2 d = \frac{\pi}{3}tan^2(\phi/2)d^3 \tag{5.12}$$

$$V_{jet}^{max} = \frac{\pi}{3}tan^2(\phi/2)(d+2R_1)^3$$

$$= \left(V_{jet}^{*max1/3} + \underbrace{\left(\frac{\pi}{3}tan^2(\phi/2)\right)^{1/3}2R_1}_{\approx 0.2}\right)^3$$

$$V_{jet}^{max} \approx \left(V_{jet}^{*max1/3} + 0.2R_1\right)^3 \tag{5.13}$$

$$\epsilon_{jet} = V_{jet}^{max}/\left[(4\pi/3)R_1{}^3\right] \tag{5.14}$$
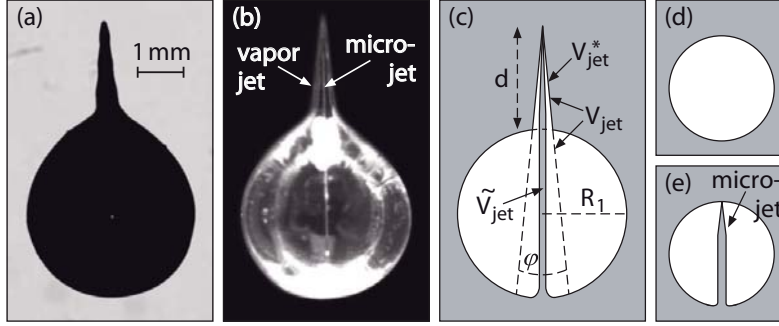
Figure 5.6: (a),(b) Observations of the gravity-driven jet of a rebounding cavitation bubble (R_{max} = 3 mm, ΔP = 10 kPa) in normal gravity: (a) using a back-illumination, (b) using a front-illumination and adaptive overlaying of different exposures to increase the dynamic range of sharpness. The vapor jet envelops a narrow microjet. (c) Definition of the variable used in the equations. (d)-(e) Two cases where no vapor jets are visible. (d) A bubble with no microjet, (e) A bubble with the longest microjet not leading to a visible vapor jet. [41].

In order to find an empirical relationship between the experimental conditions and the normalized jet volume, we define a non-dimensional parameter ζ, and assume that we can find a linear relationship between ζ and ϵ_{jet}. ζ is defined as a power law for the experimental parameters R_{max}, ρ, g, $\Delta p = p_\infty - p_v$, η, and c, where η is the viscosity, and c is the speed of sound in water. The general non-dimensional form of ζ is:

$$\zeta = (R_{max}^{a_1}\rho^{a_2} g\Delta p^{a_1-a_2-1} c^{-a_1+2a_2-1}\eta^{-a_1+1})^{a_3} \tag{5.15}$$

were a_1, a_2, a_3 are free parameters. To determine the values of a_1, a_2, a_3, a χ^2 fit is performed over the experimental data in order to minimize the rms of the ratios ϵ_{jet}/ζ. The experimental data used are the data collected during the flight campaign, plus measurements of bubble collapses in three liquids of different viscosity. The three liquids are water-glycerol mixture, of following composition: (1) pure water, η_1 = 1 mPa s, (2) 25% glycerol mass, η_2 = 2 mPa s, and (3) 75% glycerol mass, η_3 = 30 mPa s. Note that the variation of p_v, ρ, and c due to the addition of glycerol is taken into account when performing the χ^2 fit. The surface tension σ is deliberately neglected because we consider relatively large bubbles. Indeed, the terms of pressure in the Rayleigh equation $\Delta p + 3/2\rho\dot{R}(t)$ exceed term of surface tension $2\sigma/R(t)$ by a factor $> 10^2$ during the whole collapse for the bubbles considered for the χ^2 fit.

The χ^2 fit leads to: $a_1 = 1.04 \pm 0.03$, $a_2 = 1.05 \pm 0.20$, , and $a_3 = 0.98 \pm 0.10$. As $a_1 = a_2 = a_3 = 1$ is consistent with the results of the χ^2 fit, this solution is adopted in a effort of simplicity. Considering the hydrostatic pressure gradient $|\nabla p| = \rho g$, the non-dimensional parameter ζ becomes:

$$\zeta = \frac{|\nabla p| R_{max}}{\Delta p}. \tag{5.16}$$

The values of ϵ_{jet} as a function of ζ are plotted in Fig. 5.7. The points align along one straight line, which justify a posteriori the use of a power law for the construction of ζ, and the linear relationship between ϵ_{jet} and ζ. The linear regression between ϵ_{jet} and ζ leads to:

$$\epsilon_{jet} = 5.4\,\zeta. \tag{5.17}$$

Note that in certain cases, it is possible that the microjet forms into the bubble, but it does not reach the opposite interface. No vapor jet becomes visible. The critical case of the longest "invisible" microjet, see Fig. 5.6 (e), defines the threshold of apparition of the jet. In this critical case, we have $V_{jet}^{*\ max} = 0$ and $V_{jet}^{max} = (0.2\,R_1)^3$. From Eq. 5.14, we obtain $\epsilon_{jet} = \epsilon_{jet}^{min} = 0.2/(4\pi/3) \approx 0.002$, which corresponds to $\zeta_c \approx 4 \cdot 10^{-4}$. Therefore, we conclude that the threshold for apparition of a visible jet is $\zeta > \zeta_c \approx 4 \cdot 10^{-4}$. The shaded area on Fig. 5.7 represents the cases where no jet are visible.
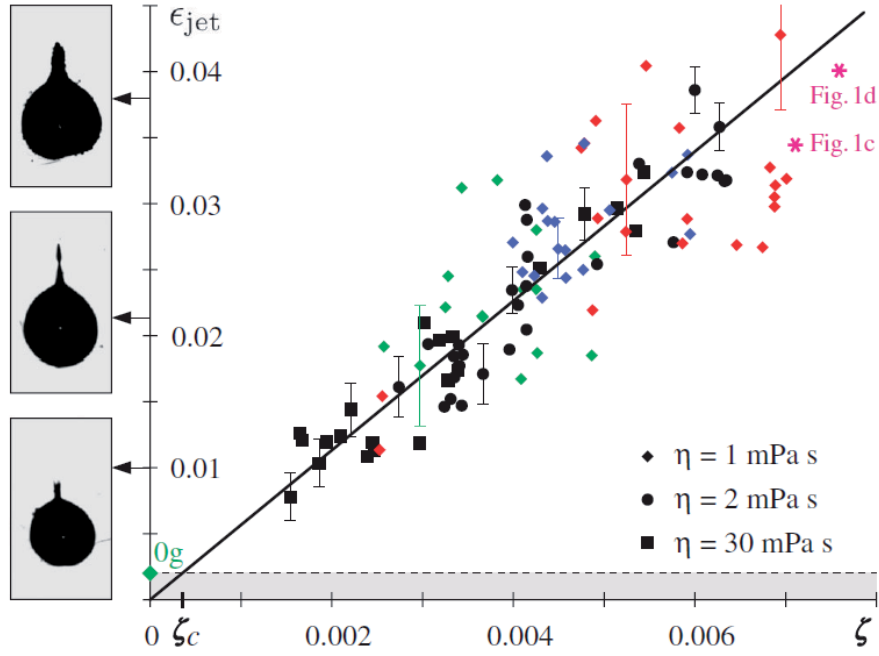
Figure 5.7: Normalized jet volume ϵ_{jet} as a function of the non-dimensional parameter ζ. Black points are data at varying R_{max}, p_0, η and fixed $g = 9.81\,ms^{-2}$. Grey points are data at varying R_{max}, p_0, g and fixed $\eta = 1\,mPa\,s$. Some 67% measurement uncertainties are shown by the error bars. The solid line is the weighted regression. [41].

5.4 Theoretical model for the volume of the jets

The proportional relationship between ϵ_{jet} and ζ deducted from the experiments can also be derived from theoretical principles [41]. By conservation of the momentum, the momentum of the microjet is equal to the integral of the momentum accumulated by the liquid during the growth and collapse of the bubble. This momentum is called the "Kelvin impulse" [24, 55], and is calculated as

$$I = \int_{-T_c}^{T_c} dt \int_{S(t)} d\vec{F} \qquad \text{with} \qquad d\vec{F} = -p\,d\vec{S} \tag{5.18}$$

where T_c is the collapse time, S is the surface of the bubble (assumed spherical), and $d\vec{F} = -p\,d\vec{S}$ the force acting on the surface of the bubble.

The spherically symmetric terms in the pressure field vanish with the integration over S. Therefore, we only consider the anisotropic terms, given by the constant hydrostatic pressure gradient $\vec{\nabla}p$. In addition to the pressure in the liquid, an additional pressure gradient forms because of the motion of the bubble interface [2]. This gradient is dependant on the normalized time $t^* = t/T_c$, and contains a spherically symmetric term, and a linear term proportional to $\vec{\nabla}p$ caused by the motion of the bubble center. Neglecting the spherically symmetric terms that vanish in the integral, we obtain

$$d\vec{F} = -f(\tau)(\vec{\nabla}p\,d\vec{R})dS \tag{5.19}$$

where $f(\tau)$ is a scalar function associated with the additional pressure gradient induced by the bubble, and $\vec{R}$ is the vector going from the center of the bubble to a surface element of the bubble.

Using the spherical coordinates (R, ϕ, θ), where θ is the angle between $\vec{\nabla}p$ and $d\vec{R}$, we calculate

$$\vec{\nabla}p \cdot \vec{R} = |\vec{\nabla}p|\,R\,cos(\theta) \tag{5.20}$$

and insert into Eq. 5.19:

$$\int_{S(t)} d\vec{F} = -f\,R^3\,\vec{\nabla}p \int_0^{2\pi} d\phi \int_0^{\pi} sin(\theta)\,cos^2(\theta)\,d\theta = -\frac{4\pi}{3}\vec{\nabla}p\,f\,R^3 \,. \tag{5.21}$$

The microjet momentum defined in 5.18 becomes:

$$I = \int_{-T_c}^{T_c} dt \int_{S(t)} d\vec{F} = \frac{4\pi}{3}\vec{\nabla}p \int_{T_c}^{T_c} f(\tau)\,R^3\,dt. \tag{5.22}$$

According to Rayleigh theory, the evolution of the radius of the bubble during the collapse can be expressed as $R(t) = R_{max}\tilde{R}(\tau)$, where $\tilde{R} = R(t)/R_{max}$ is a unique function. Finally, we obtain the folloing relationship for the microjet momentum I:

$$I = -\frac{4\pi}{3}\,\vec{\nabla}p\,R_0^3\,T_c\int_{-1}^{1}f(\tau)\,\tilde{R}^3(\tau)\,d\tau \propto -\vec{\nabla}p\,R_0^3\,T_c. \tag{5.23}$$

In analogy to the Kelvin impulse, a kinetic "Kelvin" energy E can be defined:

$$E = 2\int_0^{R_{max}}\int_{S(t)}|d\vec{F}\cdot d\vec{R}| \tag{5.24}$$

Using the spherical coordinates, we calculate

$$\int_{S(t)}|d\vec{F}\cdot d\vec{R}| = 2\pi|\vec{\nabla}p|fR^3\,dR. \tag{5.25}$$

Since f, referring the bubble collapse, can be written as a function of $\tilde{R}$ we have

$$\int_0^{R_{max}}fR^3\,dR \propto R_0{}^4. \tag{5.26}$$

Combining Eqs. 5.24-5.26, we link the kinetic Kelvin energy to:

$$E \propto |\vec{\nabla}p|R_{max}^4. \tag{5.27}$$

We define m and v the mass and the spatially averaged velocity of the fully developed microjet. We obtain the following relationships for the Kelvin impulse I and the Kelvin energy E:

$$I = mv \qquad \text{and} \qquad E \propto mv^2. \tag{5.28}$$

Using Eqs. 5.28, and the relationship for the Rayleigh time $T_C \approx 0.915R_{max}\sqrt{\rho/\Delta p}$ we find

$$v \propto -\sqrt{\Delta p/\rho}\,\vec{e} \tag{5.29}$$

and

$$m \propto |\vec{\nabla}p|R_{max}^4\rho/\Delta p. \tag{5.30}$$

where $\vec{e} = \vec{\nabla}p/|\vec{\nabla}p|$.

Now we assume that the effective volume of the vapor jet scales with the volume of the microjet, at an efficiency $\epsilon \propto R_{reb}^3 / R_{max}^3$. We justify this approximation by the fact that the vapor jet grows out of the rebound bubble, and thus consumes a fraction of the volume which is proportional to R_{reb}^3. We can finally derive a relationship for the normalized jet volume ϵ_{jet}:

$$\epsilon_{jet} \propto \frac{|\vec{\nabla}p|R_{max}}{\Delta p} = \zeta. \tag{5.31}$$

In conclusion, we find the same relationship $\epsilon_{jet} \propto \zeta$ form both the experiment and the theory.

5.5 Discussion

Previous studies have already observed the apparition of a gravity induced jet at the collapse [24, 74], and mentioned the usefulness of the concept of Kelvin impulse for the jets developing at the bubble collapse [24, 55]. However the results shown here represent the first systematic investigation of the effect of the gravity on the apparition of the jet at the collapse of a cavitation bubble. The systematic parametrical study results in the construction of a phenomenological law linking the volume of the jet with the experimental conditions ($\epsilon_{jet} \propto \zeta$). This phenomenological law is supported by theoretical considerations, issued from the concept of Kelvin impulse.

We found that a microjet appears if $\zeta > 4 \cdot 10^{-4}$. To give an order of magnitude, this means that in a liquid at atmospheric pressure and normal gravity, a bubble with a minimum radius of 4 mm is necessary to observe the gravity induced jet. We achieved a maximum radius of 3.2 mm ($\equiv$ 14 mJ) with our 230 mJ laser. Therefore, the best way to investigate the effect of gravity on the jet is to generate bubbles at reduced pressure. Indeed, with a pressure of 25 kPa, the jet appears on bubble with maximum radius of 1 mm. Note that the experimental conditions investigated here are limited to $\zeta < 0.008$. To obtain $\zeta > 0.008$ at atmospheric pressure and normal gravity, it would require a bubble with a maximum radius > 82 mm. Such large bubbles at atmospheric pressure would probably require other methods to generate the bubble than the laser method.

It is interesting to point out that the key parameter ζ can be reduced to a ratio of pressures. ζ is the ratio between the difference in the pressure between the top and bottom of the bubble, and the difference in the pressures between the inside and the outside of the bubble. The apparition of a microjet can thus be regarded as a problem of non-uniform pressure on the bubble surface.

$$\zeta = \frac{|\vec{\nabla}p|R_{max}}{\Delta p} = \frac{1}{2}\frac{\left(p_{bottom} - p_{top}\right)}{\left(p_{outside} - p_{inside}\right)}. \tag{5.32}$$

Neither the viscosity nor the surface tension appear in the definition of ζ, which might seem counterintuitive. The independence on viscosity is verified experimentally by varying the value of viscosity by a factor 30 without a significant effect on the results. The surface tension is neglected here, but could be indirectly taken into account in the definition of the collapse time T_c, leading to Eq. 5.29. With the surface tension, the collapse time of the bubble would vary by around 1% for the order of magnitude of the bubbles we consider. The effect on the volume of the jet is thus insignificant.

In this chapter, we demonstrate that a pressure gradient in the liquid can induce the formation of a microjet at the collapse of a bubble. However, the jet is only one of the four collapse channels we identified. The next step is thus to investigate what is the effect of the pressure gradient on the rebound, the shock wave, and the luminescence. This is undertaken in the next chapter. We take advantage of the microgravity phases to investigate the case of a perfectly spherical collapse, i.e., without jet. The results are then compared with those obtained in normal and hypergravity.

6 Energy partition at the collapse of a spherical bubble

6.1 Energy partition: a new approach of the bubble collapse

So far, studies on the collapse of cavitation bubbles have examined on one collapse channel at a time, namely the rebound, the jetting, the shock waves or the luminescence. It has been observed that the dynamics or the intensity of each of these phenomena is closely dependant on experimental conditions such as the type of liquid, the pressure in the liquid, or the presence of a boundary. However, we still poorly understand how the variation of one collapse channel might affect the others. The original approach proposed here is to look at how the energy available initially in the cavitation bubble is partitioned at the collapse between all the different channels.

The energy partition approach is first applied to the simplest case study: the collapse of a spherical cavitation bubble. Thank to the microgravity, and the innovative focussing system, we were able to generate what we consider the "most spherical" cavitation bubble. Indeed, we avoid the deformation of the bubble due to the hydrostatic pressure gradient, resulting in the formation of the microjet. Also, we note that the energy involved in the thermal process leading to luminescence is usually negligible with respect to the energy in the rebound or in the shock [75]. Therefore, we reduce the problem to the partition of the energy in the initial cavitation bubble into the shock and the rebound. Another advantage of considering the spherical collapse is the availability of simple theoretical model for the bubble dynamics. The energy partition can thus be modeled, and the accuracy of the model tested with the experimental results. In a second phase, we study the effect of the hydrostatic pressure gradient, by comparing the experiments performed in microgravity with those in normal and hypergravity. This comparison allows us to estimate the contribution of the gravity induced microjet studied in Ch. 5 to the partition of the initial bubble energy.

6.2 Experimental results for the collapse in microgravity

6.2.1 Rebound bubble

In the course of the flights, the bubble dynamics at three distinct water pressures p_∞ (10 kPa, 30 kPa and 80 kPa) is observed. For each pressure, the laser pulse energy is varied from 55 to 230 mJ, resulting in maximal bubble radii R_{max} from 2 to 5.6 mm. Figure 6.1 shows three laser-induced bubbles generated in microgravity, with a laser energy of 67 mJ, at a pressure in the water of respectively 10, 30, and 80 kPa. We observe that the maximum radius of the bubble R_{max}, and maximum radius of the rebound bubbles R_{reb} are different in each case. The variation of the maximum radius of the bubble is explained by considering the potential energy of the bubble $E_{pot} = 4/3\pi R_{max}^3(p_\infty - p_v)$, as detailed in section 5.2. The fraction of energy transferred from the laser pulse into the bubble potential energy is constant. Therefore, when the pressure in the liquid decreases, the bubble maximum radius increases in order to keep the same value of the potential energy at bubble maximum radius in each case.

The variation of the maximum radius of the rebound bubble is more puzzling. In Fig. 6.2, we show cavitation bubbles generated at water pressure of (a) $p_\infty = 30$ kPa and (b) $p_\infty = 10$ kPa. The images in the case (a) are enlarged so the the maximum radius appears to be identical to case (b) on the figure. The maximum radius of the rebound is larger in the case (b) $p_\infty = 10$ kPa than in the case (a) $p_\infty = 30$ kPa. The maximum radius of the rebound bubble, normalized by the maximum radius of the bubble, is larger when the pressure in the liquid is lower.

(a)

R_{max} = 5.2 mm
P_{cav} = 10 kPa

(b)

R_{max} = 3.6 mm
P_{cav} = 30 kPa

(c)

R_{max} = 2.5 mm
P_{cav} = 80 kPa
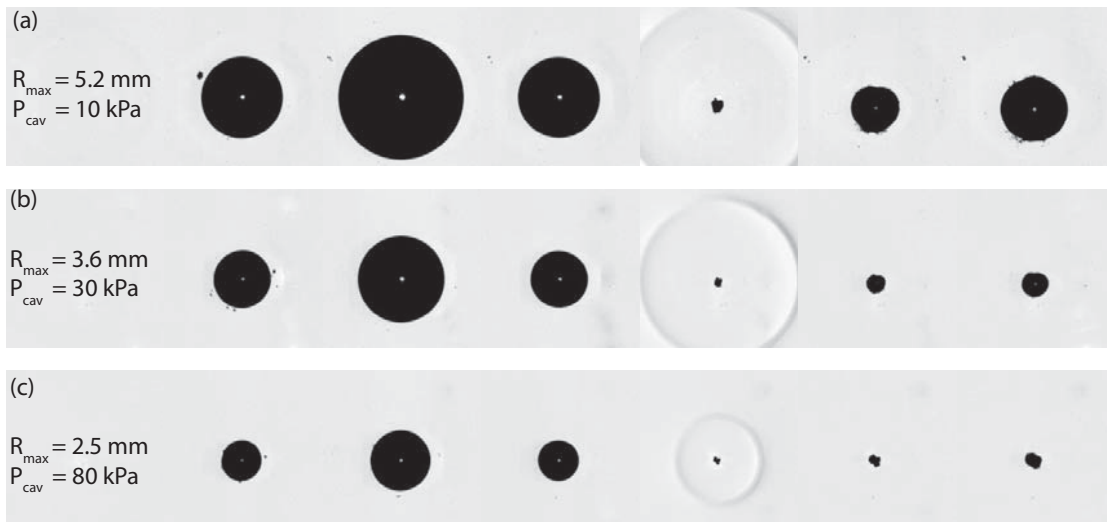
Figure 6.1: Three bubbles generated with the same laser energy, in microgravity, at three different pressures in the liquid p_∞.

Figure 6.2: Selected high-speed images of a cavitation bubble at two different water pressures. The images are scaled so that the bubble appears with the same normalized R_{max} on the figure. (a) $p_\infty = 30$Pa, $R_{reb}/R_{max} = 0.22$, (b) $p_\infty = 10$Pa, $R_{reb}/R_{max} = 0.57$. [29]

The variation of the normalized maximum radius of the rebound is a direct indication of how much energy of the initial bubble is transferred into the rebound at the collapse of the bubble. Indeed, we calculate the potential energy of a bubble as [37]

$$E_{pot} = \int_0^R 4\pi r^2 \Delta p \, dr = \frac{4\pi}{3} R^3 \Delta p, \tag{6.1}$$

where R is the bubble radius. In particular, we define the initial bubble energy E_0 and the rebound energy E_{reb} as

$$E_0 = \frac{4\pi}{3} R_{max}^3 \Delta p \quad \text{and} \quad E_{reb} = \frac{4\pi}{3} R_{reb}^3 \Delta p. \tag{6.2}$$

The relationship between R_{reb}/R_{max} and E_{reb}/E_0 writes

$$\frac{E_{reb}}{E_0} = \frac{\frac{4\pi}{3} R_{reb}^3 \Delta p}{\frac{4\pi}{3} R_{max}^3 \Delta p} = \left(\frac{R_{reb}}{R_{max}} \right)^3. \tag{6.3}$$

Figure 6.3 shows the normalized radius R/R_{max} for a representative selection of bubbles as a function of the normalized time t/τ_c, where τ_c is the bubble collapse time according to Rayleigh theory [7]: $\tau_c = 0.915 R_{max} \sqrt{\rho/\Delta p}$ with ρ being the density of the liquid and Δp being the "driving pressure", i.e. the difference between the static liquid pressure p_∞ and the pressure p_v of the condensable vapor inside the bubble. The value of p_v is calculated with the Antoine equation from the temperature of the water measured for each of the three flight days. The three temperatures are respectively 16.8 °C, 23.9 °C and 20.9 °C, corresponding to p_v of 1910 Pa, 2950 Pa and 2460 Pa. All the curves are remarkably superposed during the first collapse, and consistent with the Rayleigh theory (solid line in the figure). However, as already shown in Figs 6.1, 6.2, and 6.3, the dynamics of the rebound is very different depending on the pressure in the liquid p_∞. The high-speed movies reveal that for a given maximum radius R_{max}, the maximum radius of the rebound R_{reb} decreases with p_∞, as plotted in Fig. 6.4.

When looking at the results in term of energy, Fig. 6.5 reveals that E_{reb} scales linearly with E_0 for given liquid pressures p_∞. The least square linear regression on E_{reb} as a function of E_0 for each p_∞, gives respectively 1%, 2%, and 20% for 80, 30 and 10 kPa. In consequence, when p_∞ decreases, the fraction of energy going in the rebound bubble increases.
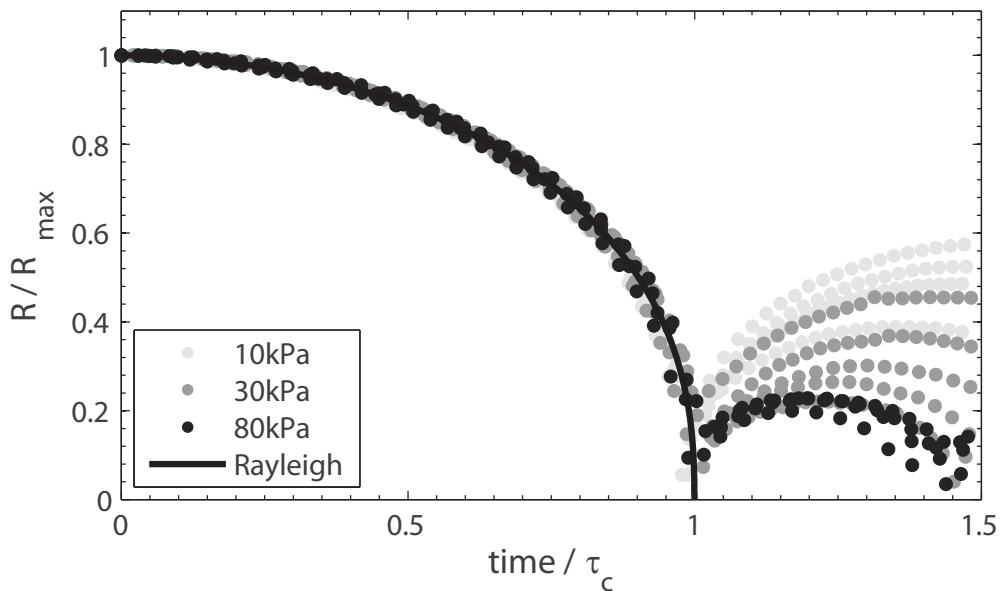
Figure 6.3: The normalized radius for a representative selection of bubbles as a function of the normalized time, for different pressure levels p_∞. The experimental data (dots) are consistent with the Rayleigh theory (solid black line). [29]
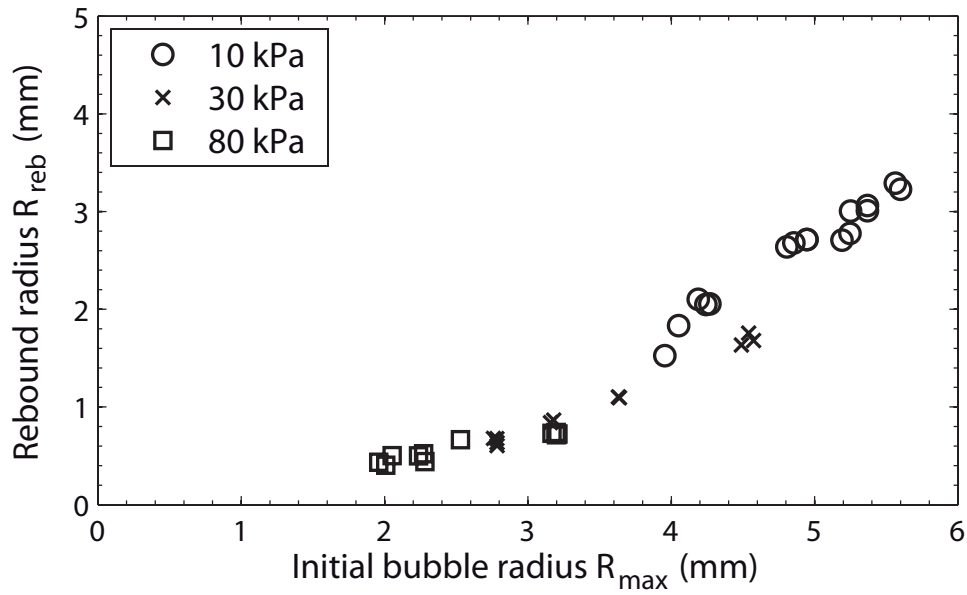
Figure 6.4: Measured maximum radius of the rebound bubble as a function of the maximum radius of the initial bubble, for different pressure levels p_∞.
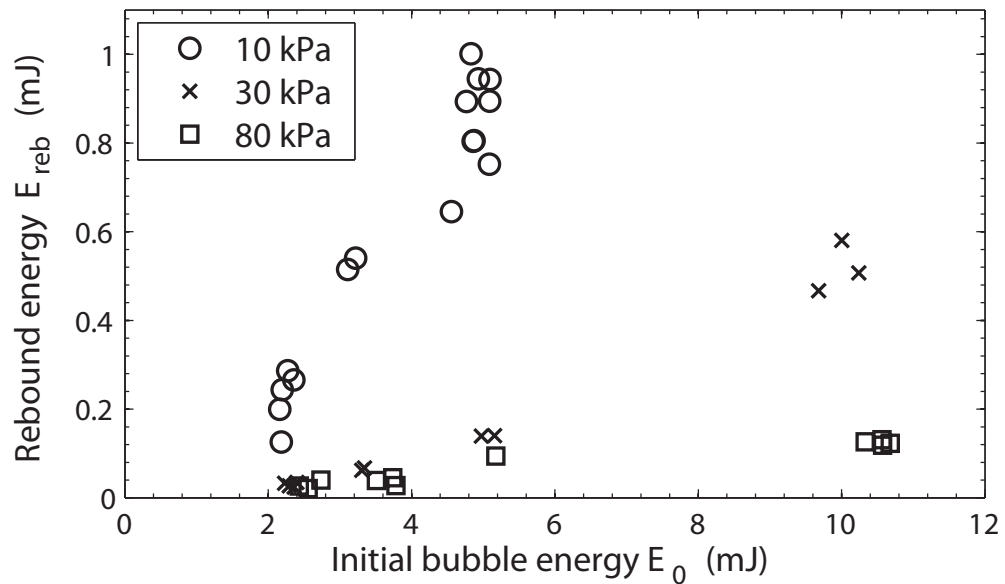
Figure 6.5: Measured potential energy of the rebound bubble as a function of the initial bubble energy, for different pressure levels p_∞. [29]

6.2.2 Shock wave energy

At the collapse of the cavitation bubble, a shock wave is released, dissipating a large part of the energy of the cavitation bubble. The energy carried away by the shock can be estimated from the pressure profile of the shock wave. Given a shock pressure profile $p(t)$, measured at a distance d from the bubble center, the shock energy is given by [46, 76]

$$E_{SW} = \frac{4\pi d^2}{\rho c} \int p(t)^2 \mathrm{d}t, \tag{6.4}$$

where ρ is the water density and c is the speed of sound in water. The difficulty is thus to measured accurately the pressure profile $p(t)$.

On our setup, a piezo-resistive dynamic pressure sensor (Unisensor) is used to monitor the shock waves that propagate through water. The sensor is fixed at the bottom of the vessel, below the bubble generation point. The sensor is connected to a oscilloscope (Lecroy) for the acquisition of the signal through an amplifier. A typical signal is shown in Fig. 6.6. We observe a first peak at the generation of the plasma by the laser (t = 0 ms). A second peak, corresponding to the collapse of the bubble is visible at t = 1.56 ms.

With this piezo-resistive dynamic pressure sensor, the duration of the shock transition, i.e., the characteristic time-scale of $p(t)$ (<100 ns), is much shorter than the characteristic response time (10 μs) of the pressure sensor. An accurate measurement of $p(t)$, leading to a direct calculation of the shock energy is not possible. Nevertheless, a rough estimation of the shock energy remains possible under the assumption of a linear response. Explicitly, if we define $h(t)$ as the sensor's impulse response, the response of the sensor $s(t)$, is expressed as $s(t) = h(t) * p(t)$, where '$*$' denotes the convolution. We assume that the pressure $p(t)$ has a universal shape in the sense that $p(t) = p_{max} \tilde{p}(t)$, where $\tilde{p}(t)$ is the same function for all bubbles. The signal can then be expressed as $s(t) = h(t) * p_{max} \tilde{p}(t)$, and hence $\int s(t)\mathrm{d}t = p_{max} \int h(t) * \tilde{p}(t)\mathrm{d}t \propto p_{max}$. In other words, p_{max} is proportional to the integrated response. Substituting into Eq. (6.4), we finally obtain

$$E_{SW} \propto \int p_{max}^2 \tilde{p}(t)^2 \mathrm{d}t \propto p_{max}^2 \propto \left(\int s(t)\mathrm{d}t \right)^2. \tag{6.5}$$

The constant of proportionality in Eq. (6.5), which is unknown, is estimated such that the shock energy E_{SW} equals the potential energy of the initial bubble E_0 in the extreme cases, where only a negligible rebound bubble is observed. The theoretical and experimental results presented further in this chapter justify a posteriori this procedure.
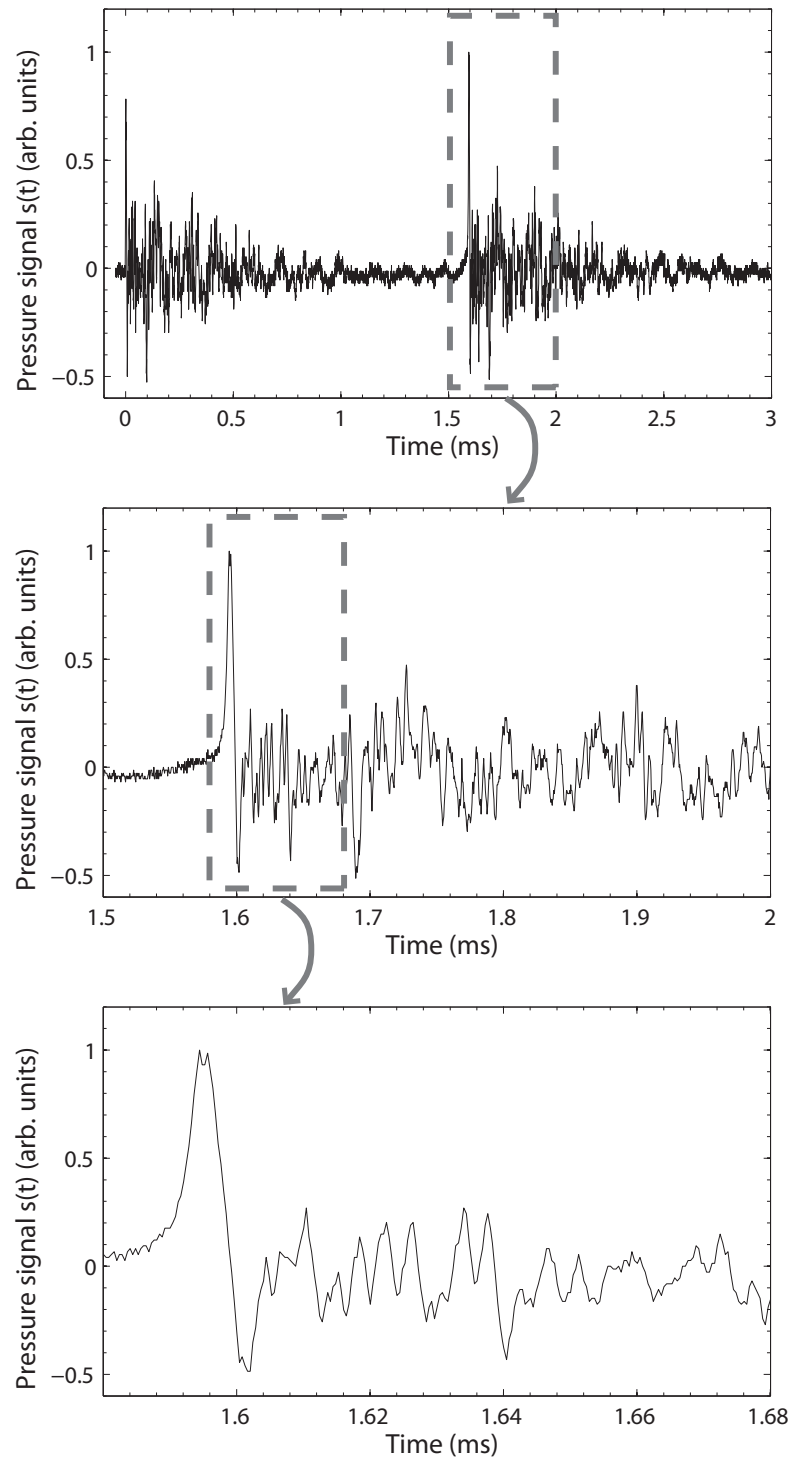
Figure 6.6: Typical signal recorded by the dynamic pressure sensor during bubble generation and oscillation.

The validity of this reasoning is tested with two different approaches, using the data collected during the parabolic flight campaign. First, the assumption $p(t) = p_{max} \tilde{p}(t)$ implies that $s(t)/max(s(t))$ is the same function of time for all measurements because $h(t)$ and $\tilde{p}(t)$ are time-dependent only. Figure 6.7 shows the first 24 μs of the normalized signal $s(t)/max(s(t))$ for all measurement (dotted grey curves) and the mean normalized signal (solid black curve). The mean standard deviation is 0.09. The solid grey curves on the figure represent the mean normalized signal $\pm$ the standard deviation. The standard deviation of the FWHM (full width at half maximum) of the first peak on the normalized signal (i.e. the shock) is 0.63 μs (for a time resolution of 0.4 μs). Those results show that all the normalized signals are reasonably similar. Therefore, we conclude that the use of the assumption $p(t) = p_{max} \tilde{p}(t)$ is suitable for the estimation of E_{SW}. In turn, this implies that $\left(\int s(t) \mathrm{d}t \right)^2 \propto p_{max}^2$.

Second, the validity of $p_{max}^2 \propto \left(\int s(t) \mathrm{d}t \right)^2$ is tested as follows. We have $\left(\int s(t) \mathrm{d}t \right)^2 = C_1 p_{max}^2$ where C_1 is a constant. We also have $\int s^2(t) \mathrm{d}t = C_2 p_{max}^2$ where C_2 is a constant. Dividing the former equation with the latter, we have

$$\left(\int s(t) \mathrm{d}t \right)^2 / \int s^2(t) \mathrm{d}t = C_1/C_2 = \text{const.} \tag{6.6}$$

Figure 6.8 shows this ratio of the integrals of the signal as a function of the potential energy E_0 for all bubbles. Despite a slight dependance on the potential energy of the bubble E_0, the ratio of the integrals is almost a constant: the average is 0.36 and the standard deviation is 0.02. Therefore, we conclude that the assumptions lead to a suitable estimation of E_{SW}.
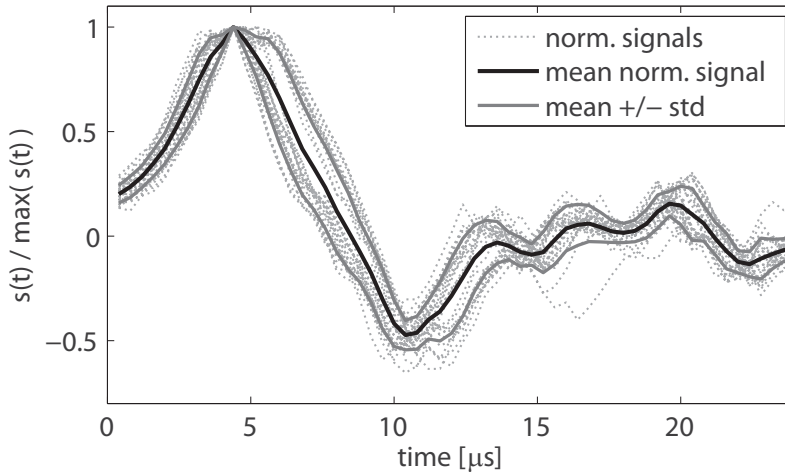
Figure 6.7: Superposition of all the normalized signals $s(t)/max(s(t))$ (dotted grey curves), the mean normalized signal (solid black curve) and the mean normalized signal $\pm$ the standard deviation (solid grey curve). [29]
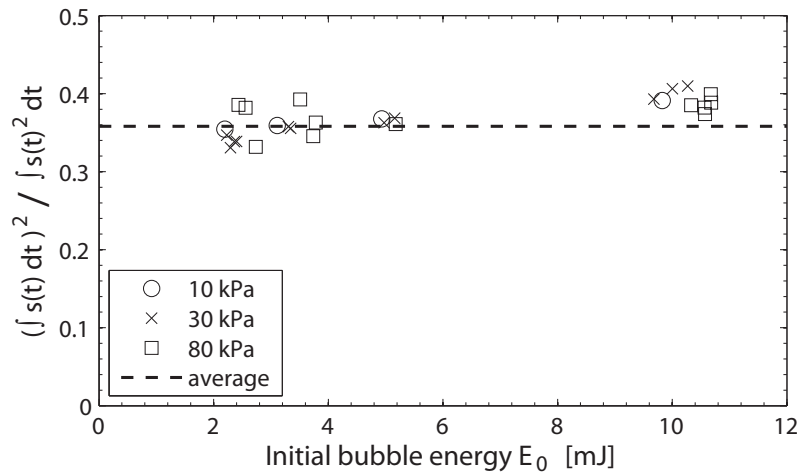
Figure 6.8: Confirmation of the validity of the assumptions for the estimation of E_{SW} : $(\int s(t)\mathrm{d}t)^2 / \int s^2(t)\mathrm{d}t \approx \mathrm{const.}$ [29]

We consider the energy carried away by the spherical shock produced at the first bubble collapse. Figure 6.9 presents the energy of the shock wave at the first collapse E_{sw} as a function of the initial potential energy of the bubble E_0. Unlike the rebound energy E_{reb}, we observe that E_{sw} scales linearly with E_0 and that the ratio E_{sw}/E_0 is close to 1. These results have two important implications: (1) The variation of the pressure on the water does not affect significantly the energy of the shock. (2) Almost all the potential energy of the bubble is transformed into shock energy at the collapse of the bubble. This means that our experiments all lie in a "shock-saturated" regime, where the shock absorbs most of the available energy ($E_{SW} \approx E_0$), and thus where the variation of the experimental conditions have insignificant effect on the energy of the shock.
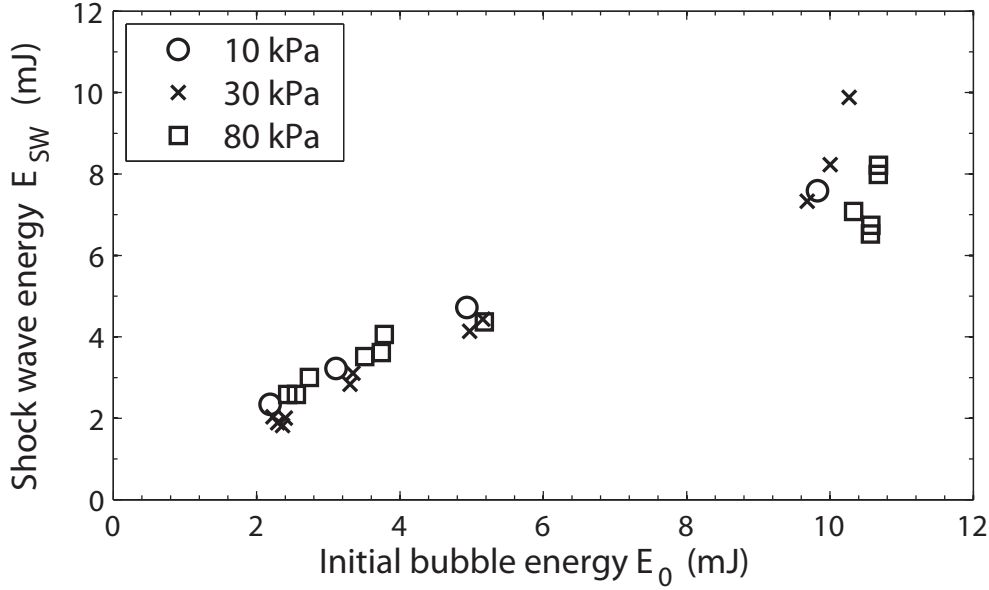
Figure 6.9: Estimated energy in the shock wave as a function of the initial bubble energy, for different pressure levels p_∞. [29]

6.3 Theoretical model for the spherical collapse

Hereafter, a theoretical model is developed to compute the energies of the rebound bubble and the shock wave as a function of various experimental parameters. The simplest model for the evolution of spherical cavitation bubbles, i.e. the Rayleigh equation, cannot produce rebound bubbles and shock waves. Indeed, to model rebounds we need to consider gas within the bubble, and to model shocks we need to consider liquid compressibility. The set of equations we develop here is based on the Keller-Miksis equation for the dynamics of the bubble, coupled with a adiabatic treatment of the gas inside the bubble.

To calculate the rebound motion it is necessary to include a non-condensable gas inside the bubble. We here assume that this gas is compressed and decompressed adiabatically, that is without heat transfer across the bubble surface. According to the adiabatic theory, the pressure $p_g(t)$ of this non-condensable gas is then given by

$$p_g = p_{g0} \left(\frac{R_{max}}{R} \right)^{3\gamma},$$ (6.7)

where p_{g0} is the pressure at the maximal initial bubble radius R_{max}, $R(t)$ is the evolving bubble radius, and γ is the adiabatic index also known as "heat capacity ratio."

To incorporate shock waves, we require a model for the bubble evolution in a compressible liquid. We here use the Keller-Miksis model [11], which is an extension of the Rayleigh equation

to compressible liquids, accurate to first order in the speed of sound c. As shown by Prosperetti [12] this model belongs to a more general class of first order models and can be rewritten as

$$\ddot{R} = \frac{(p_g - \Delta p)(1 + \tilde{v}) + R\dot{p}_g/c - (3 - \tilde{v})\dot{R}^2\rho/2}{(1 - \tilde{v})R\rho},$$

(6.8)

where $\tilde{v}(t) \equiv \dot{R}(t)/c$. Note that we deliberately neglect the effects of surface tension and viscosity for two reasons. First, these effects are quite irrelevant for the large bubbles in our experiment. Second, surface tension and viscosity are generally insignificant at the last stage of the bubble collapse, since inertial forces increase more rapidly than viscous forces and surface tension as $R(t) \to 0$. The latter can therefore be neglected to calculate rebounds and shocks.

The Eqs. (6.7) and (6.8), fitted with the initial conditions $R(0) = R_{max}$, $\dot{R}(0) = 0$, $p_g(0) = p_{g0}$, and $\dot{p}_g(0) = 0$, constitute a model for the collapse and the rebound of a spherical bubble, while including compression waves (shocks). We use the Runge-Kutta method to solve this model numerically. The radius $R(t)$ is calculated as the bubble first collapses and then rebounds until it reaches its maximal rebound radius R_{reb}.

Given a time-solution of Eqs. (6.7) and (6.8) we can then calculate various energies. The initial bubble energy E_0 and the energy of the rebound bubble E_{reb} are computed directly using Eq. (6.2). It is important to note that the temperature of the non-condensable gas changes during the adiabatic compression/decompression. The gas temperature at the rebound point is different from the initial temperature. Hence the internal energy $U = (4\pi/3)R^3 p_g/(\gamma - 1)$ of the non-condensable gas changes. We can calculate this energy change ΔU simply by subtracting the final value of U from the initial one,

$$\Delta U = \frac{4\pi}{3(\gamma - 1)}\left(p_{g0}R_{max}^3 - p_{g,reb}R_{reb}^3\right).$$

(6.9)

The adiabatic nature of the process implies that ΔU must be equal to the total work done by the liquid onto the non-condensable gas. This work can be calculated as

$$\Delta U = \int \delta W = -\int p_g dV = -\int 4\pi R^2 \dot{R}p_g dt,$$

(6.10)

where the time-integral runs from the initial bubble radius through the collapse point to the maximal rebound radius. To check the accuracy of our numerical solution we compute ΔU using both Eq. (6.9) and Eq. (6.10).

Given ΔU, the initial energy E_0, and the potential energy of the rebound E_{reb}, the compression energy of the shock wave E_{SW} can be computed from energy conservation as

$$E_{SW} = E_0 - E_{reb} - \Delta U.$$

(6.11)

Finally, we introduce the energy fractions

$$\epsilon_{reb} \equiv E_{reb}/E_0, \ \ \epsilon_{SW} \equiv E_{SW}/E_0, \ \ \epsilon_U \equiv \Delta U/E_0. \tag{6.12}$$

Eq. (6.11) implies the normalization:

$$\epsilon_{reb} + \epsilon_{SW} + \epsilon_U = 1. \tag{6.13}$$

6.4 Calculation of a non-dimensional parameter predicting the energy partition

How do ϵ_{reb}, ϵ_{SW}, and ϵ_U depend on the six model parameters R_{max}, Δp, p_{g0}, γ, ρ, and c? We first note that the four energies E_0, E_{reb}, E_{SW}, and ΔU all scale as R_{max}^3. This can be shown by rewriting the model as a function of the normalized radius $r(t) \equiv R(t)/R_{max}$. Therefore ϵ_{reb}, ϵ_{SW}, and ϵ_U are independent of R_{max}. To test the remaining five model parameters we ran $2.7 \cdot 10^5$ independent computations of ϵ_{reb}, ϵ_{SW}, and ϵ_U by taking logarithmically spaced parameters from the following intervals: $\Delta p \in [1, 100]$ kPa, $p_{g0} \in [0.1, 100]$ Pa, $\rho \in [500, 15000]$ kg m^{-3}, $c \in [1000, 2000]$ m s^{-1}, $\gamma \in [1.3, 1.5]$. By systematically studying the variation of ϵ_{reb}, ϵ_{SW}, and ϵ_U as a function of the five parameters, we can draw two main conclusions. First, the internal energy fraction is negligible because $\epsilon_U < 0.01$ in all situations. Second, all variations of ϵ_{reb} and ϵ_{SW} as a function of the five model parameters Δp, p_{g0}, γ, ρ, and c can be explained using a single non-dimensional parameter

$$\xi = \frac{\Delta p \gamma^6}{p_{g0}^{1/\gamma}(\rho c^2)^{1-1/\gamma}}. \tag{6.14}$$

In fact, Fig. (6.10) shows the $2.7 \cdot 10^5$ values of ϵ_{reb} and ϵ_{SW} as a function of ξ, revealing a tight correlation. The parameter ξ was found by first constructing the non-dimensional parameter $\Delta p (p_{g0})^a (\rho c^2)^{-a-1}$ from the four dimensional parameters Δp, p_{g0}, ρ, and c. The case where $a = 1$ is plotted in Fig. 6.11 (a). We note that the cloud of data points take the shape of a broad inverted "S". The computed results are then grouped depending on the value of γ. a is determined for each group as the value that maximizes the Pearson correlation coefficient for $\epsilon_{reb} \in [0.2, 0.8]$. We restrict ϵ_{reb} to the interval where a small variation in ξ leads to a large variation of ϵ_{reb}, thus where we want the relation to be the most univocal. The values of a obtained are correlated with γ as $a = 1/\gamma$ with an error of $\pm 10\%$. Figure 6.11 (b) plots the data points obtained using $a = 1/\gamma$. The points form smooth curves. However, each value of γ leads to a distinct curve, and the different curves are horizontally shifted. The final step is to introduce the factor γ^β to align the curves. $\beta = 6$ is then determined by maximizing the Pearson correlation coefficient on $\epsilon_{reb} \in [0.2, 0.8]$ for all values of γ. We finally obtain the tight and univocal relationship between ξ and ϵ_{reb} shown in Fig. 6.11 (c). Note that the construction of ξ is based on a phenomenologic approach. The relationship between ξ and the energy partition is valid for experimental conditions within the intervals given above.
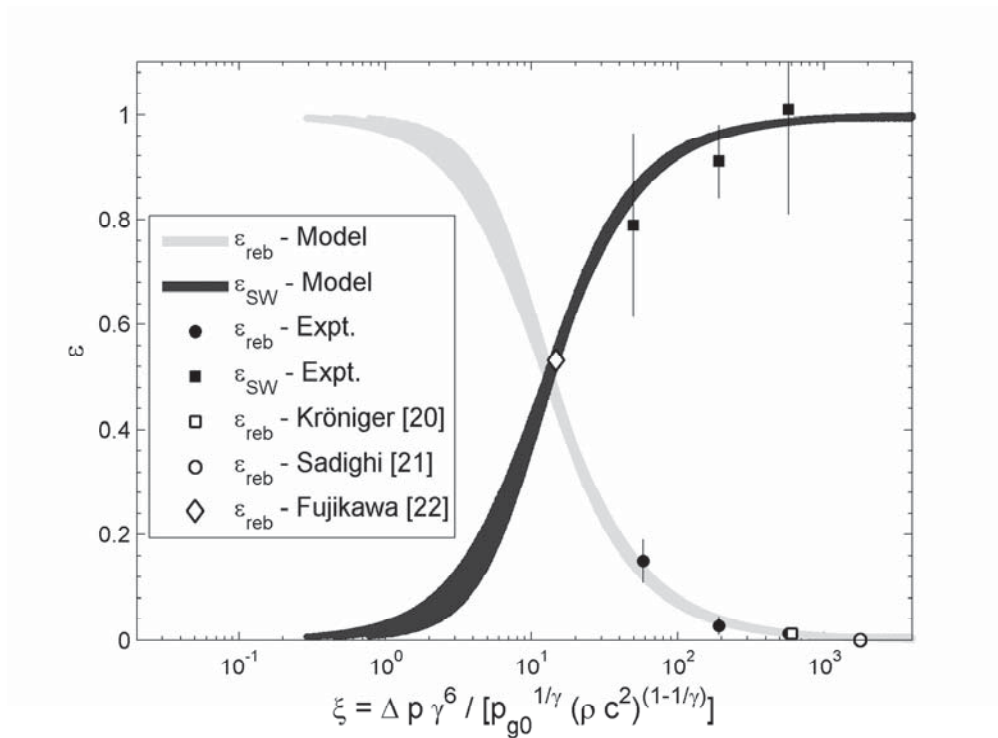
Figure 6.10: Fraction of energy in the rebound ϵ_{reb} and in the shock wave ϵ_{SW} as a function of the non-dimensional parameter ξ. The solid curves are the results from the theoretical model. The discrete black symbols are the values obtained experimentally, along with the measurement error bars. The white symbols are data extracted from the literature. [29]
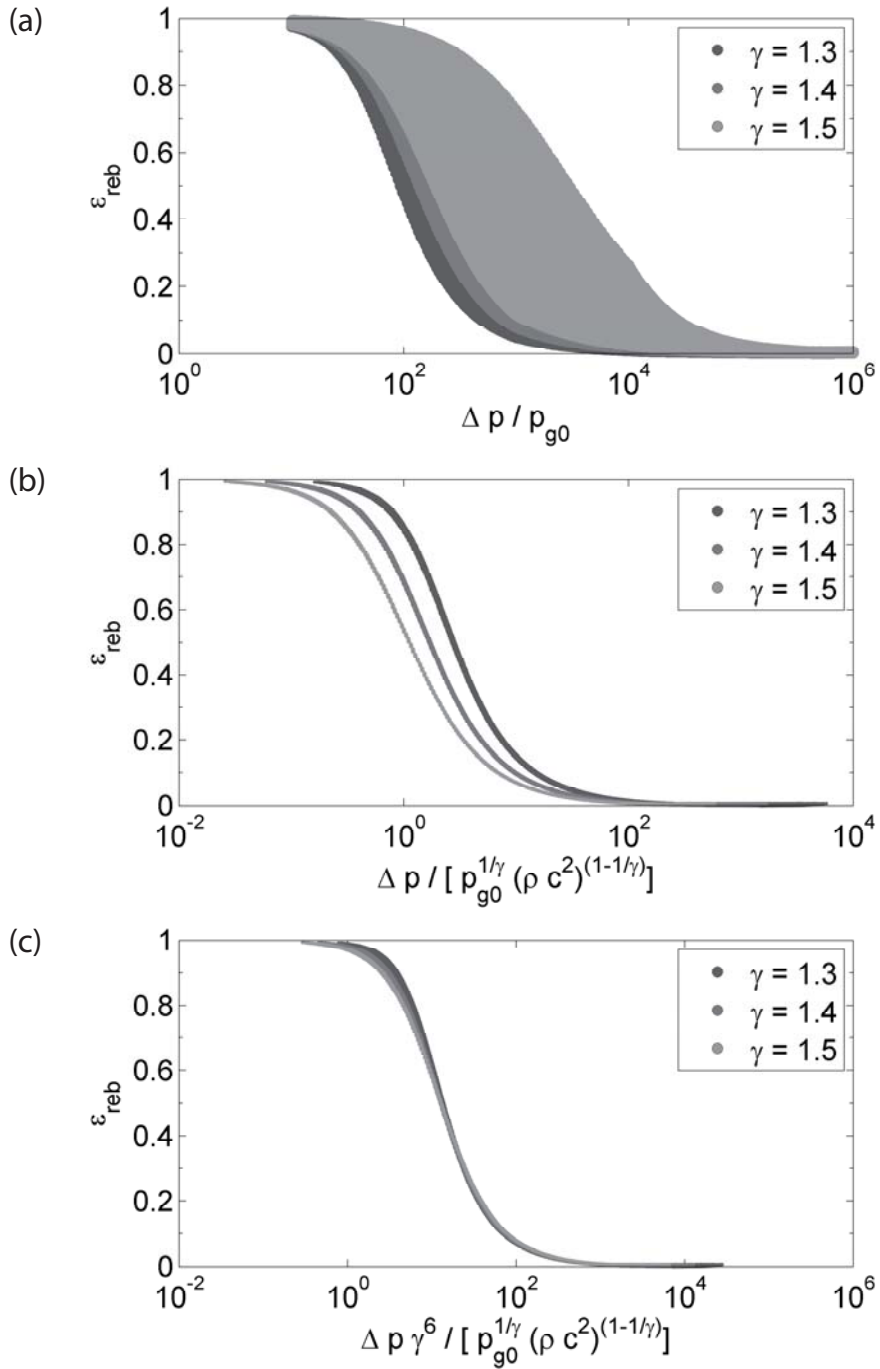
Figure 6.11: Construction of the non-dimensional parameter ξ. The fraction of energy transferred in the rebound, ϵ_{reb}, obtained from the $2.7 \cdot 10^5$ computations are plotted as a function of three different non-dimensional parameter. (a) ϵ_{reb} as a function of $\Delta p / p_{g0}$ shows the general inverted "S" shape of the data points. (b) The data points form distinct curves when ϵ_{reb} is plotted as a function of $\Delta p (p_{g0})^a (\rho c^2)^{-a-1}$, with $a = 1/\gamma$. (c) We finally obtain a tight and univocal relationship between when ϵ_{reb} is plotted as a function of ξ.

6.5   Experimental results for the collapse with a hydrostatic pressure gradient

The results shown so far are restricted to the case of a bubble collapsing spherically, in a liquid with no pressure gradient. However, in the case of hydraulic turbomachines, the bubble is subject to strong pressure gradient in the flowing liquids. It is then natural to wonder what is the effect of a pressure gradient on the partition of energy. Therefore, we compare the results in microgravity with the results of bubble collapsing in normal and hypergravity, i.e. in a liquid subject to a constant hydrostatic pressure gradient. We have already demonstrated (Ch. 5) that gravity can affect the collapse of a cavitation bubble in the form of the occurrence of a vapor jet (see Fig. 6.12). The volume of the vapor jet normalized to the maximum volume of the rebound was found to be proportional to the non-dimensional parameter $\zeta = |\nabla p| R_0 / \Delta p$, where ∇p is the hydrostatic pressure gradient. To investigate the effect of gravity on the energy partition, we performed the experiments presented in this chapter 6.2 with the same parameters at normal gravity ($1g$) and hypergravity ($1.8g$). The values of the non-dimensional parameter ζ were $\zeta \in [2.5 \cdot 10^{-3}, 7 \cdot 10^{-3}]$. Using the same methods, we measure the maximum radius of the rebound bubble, we calculate the energy in the rebound bubble, and we estimate the energy in the shock for each bubble generated. The radius of the rebound bubble as a function of the maximum radius, and its transposition in energy, is shown respectively in Figs. 6.13 and 6.14. The estimation of the shock energy as a function of the bubble initial energy is plotted in Fig. 6.15.
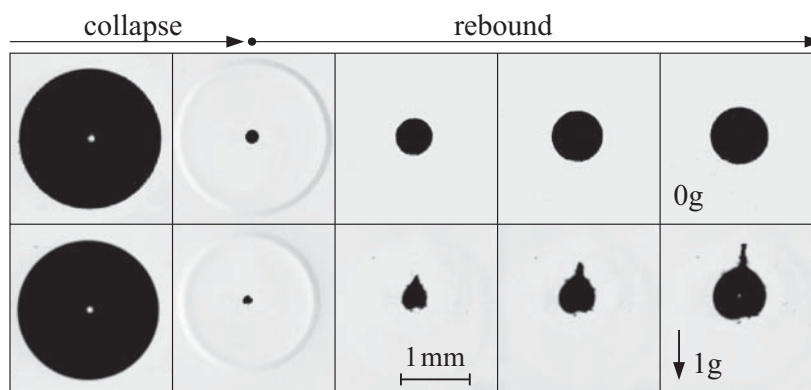
Figure 6.12: Collapse and rebound of a bubble in $0g$ (upper) and $1g$ (lower). Note the shock visible at the collapse, and the vapor jet on the rebound for $1g$ [41].
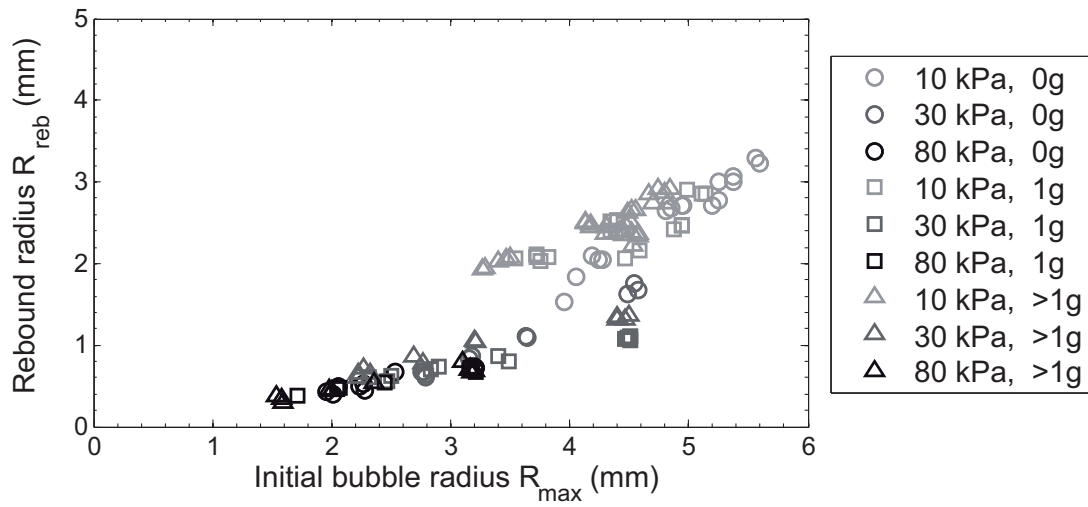
Figure 6.13: Measured maximum radius of the rebound bubble as a function of the maximum radius of the initial bubble, for different pressure levels p_∞ and different gravity levels.
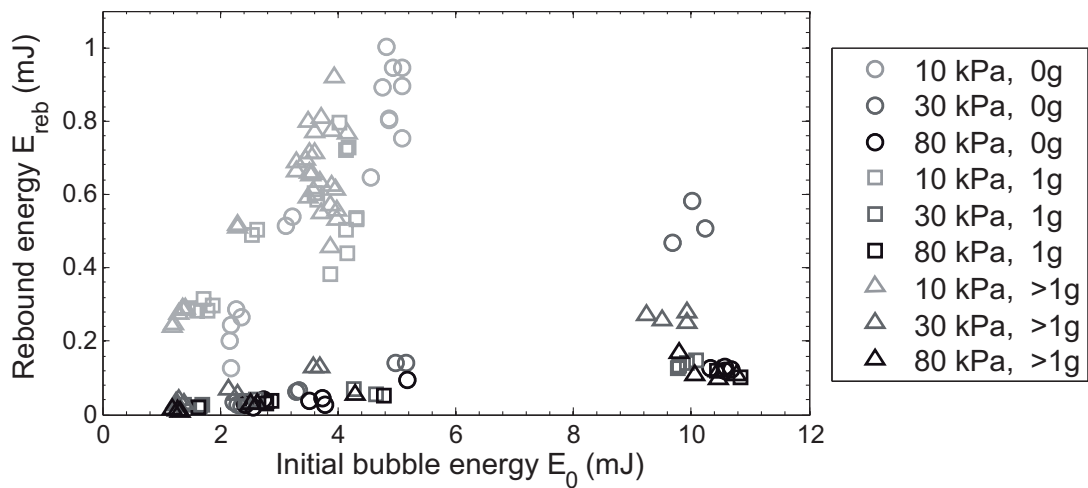
Figure 6.14: Measured potential energy of the rebound bubble as a function of the initial bubble energy, for different pressure levels p_∞ and different gravity levels.
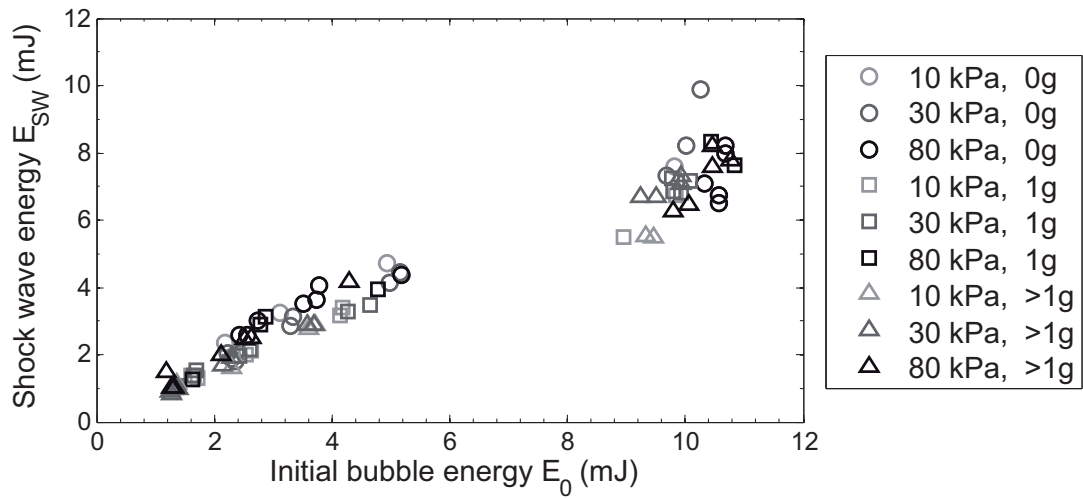
Figure 6.15: Estimated energy in the shock wave as a function of the initial bubble energy, for different pressure levels p_∞ and different gravity levels.

Unlike for the vapor jet, we do not observe a significant difference in the energy partition when the gravity changes. The relative difference between the values of ϵ_{reb} at $0g$ and at $\geq 1g$ are smaller than the standard deviations of the measurements at $0g$. We deduce that the energy transferred into the vapor jet is negligible compared to the energy in the rebound and in the shock. In consequence, the results draw in microgravity also apply to bubbles collapsing in a hydrostatic pressure gradient for $\zeta < 7 \cdot 10^{-3}$.

6.6 Discussion

6.6.1 Effect of gravity on the energy partition

The gravity does not affect significantly our experimental results on the energy partition between the rebound and the shock wave. However, this does not mean that gravity has no effect on the collapse channels. Indeed, we demonstrate the effect of gravity in the formation of the microjet at the collapse of the bubble in Ch. 5, and a previous study [48] concluded that the gravity has an effect on the energy radiated by luminescence. But the energies involved in those latter phenomena are negligible compared to the energies involved in the rebound or the shock wave. Therefore, if gravity affects the microjet or the luminescence, the impact on the rebound or the shock remains insignificant, which explains why we could not detect it by monitoring the rebound and the shock only.

6.6.2 Comparison between model predictions and experiment: Estimation of p_{g0}

The theoretical model allows us to explain why, according to our experimental results, the energy of the rebound depends on the pressure in the liquid while the energy of the shock wave seems to scale with the initial potential energy only. However, to compare the experimental results with the theoretical ones, we need a value for p_{g0} in addition to the measured Δp and R_{max} and the known ρ, c and γ. According to the theoretical model, p_{g0} is the pressure of the non-condensable gas in the bubble at the instant when the radius of the bubble is equal to R_{max}. Since p_{g0} is not directly measurable, we simply assume this pressure to be constant, and estimate its value using the theoretical model.

We estimated the value of p_{g0} by fitting the model to the experimental results. For each measurement, the value of p_{g0} leading to the observed R_{reb} is calculated with an iterative process. The results are averaged and we obtain $\overline{p_{g0}} = 7.0 \pm 3.5$ Pa. The relatively small variance a posteriori justifies the assumption of a constant value for p_{g0}. The experimental points are plotted in Fig. 6.10, where the values of ξ are calculated using $\overline{p_{g0}}$.

We observe that all our experimental data lies in a regime where $\epsilon_{SW} \approx 1$. So when ξ varies because of the change of Δp, the relative difference is important for ϵ_{reb} but not for ϵ_{SW}. As ϵ_{reb} and ϵ_{SW} represent the slopes of the curves in Fig. 6.5 and Fig. 6.9 respectively, the difference in p_∞ is significant for the rebound, but insignificant for the shock.

Both theoretically and experimentally, the relation $E_{reb} + E_{SW} = E_0$ is obtained. The results using the theoretical model show that ΔU in Eq.(6.11) is negligible. Furthermore, the luminescence energy E_{rad} can be roughly estimated using the model by integrating the thermal energy radiated by the bubble E_{rad}. Assuming black body radiation, E_{rad} is given by Stefan's Law: $E_{rad} = \int_{t_0}^{t_{reb}} \sigma 4\pi R^2 (T^4 - T_0^4) dt$, where $\sigma = 5.67 \ 10^{-8} \ \mathrm{Js^{-1} m^{-2} K^{-4}}$ is the Stefan constant, T is the temperature inside the bubble, and T_0 the temperature in the liquid. The result overestimates the reality because we use the temperature calculated with an adiabatic treatment, while the

radiation itself dissipate heat and thus lead to lower temperature than the one considered. We still find $E_{rad} < 0.1 \cdot E_{reb}$ for our experimental conditions, which justifies that the radiated energy is negligible compared to the rebound energy. Thus, neglecting both ΔU and E_{rad}, we have $E_{reb} + E_{SW} = E_0$. When adding the experimental data from Fig. 6.5 and Fig. 6.9, we also obtain $E_{reb} + E_{SW} = E_0$, within a scatter of $\pm 20\%$. This scatter is reasonable considering the uncertainty introduced with the rough estimation of E_{SW}.

6.6.3 Comparison with earlier work

The main issue with the treatment of the rebound is that the pressure of non-condensable gas p_{g0} is usually needed in the equation of motion. As p_{g0} is not measurable and its origin is not clear yet, it is difficult to estimate it and thus to validate a model. So in a concern of evaluating our theoretical model, we look at previous studies for comparison. In the work of Fujikawa et al. [77], Kröninger et al. [78] and Sadighi-Bonabi et al. [79] we found estimates of p_{g0} or enough information to obtain them. The data extracted from these articles are plotted in Fig. 6.10. We observe that despite the different treatments of the thermodynamics inside the bubble ([77] considered conductive heat transfer and condensation/evaporation, [78] used a Van der Waals equation and [79] considered hydrochemical reactions) our model reproduces reasonably well their results. Yet, the drawback of our model is that the temperature at the collapse is overestimated because of the neglected thermal transport. This could be improved by the addition of heat transfer or chemical reactions, but at the cost of the simplicity of the model.

Akhatov et al. [26] propose a mathematical model supported by experimental measurements of the rebound of a spherical cavitation bubble. Because of the difference in the model used (the pressure of non-condensable gas is derived from a phase transition equation), we could not derive a value for p_{g0} for quantitative comparison of our results. Nonetheless, qualitatively, the conclusions are the same. Akhatov et al. observed that the ratio between the radius of the rebound and the initial bubble is constant when only varying the initial radius of the bubble, which confirms the univocal relation between ξ and ϵ_{reb}. They also showed numerically that for given experimental conditions, when the concentration of the non-condensable gas in the bubble increases, the radius of the rebound bubble increases too. This also agrees with our conclusions. Indeed, the increase of the concentration of non-condensable gas means a smaller value of ξ which implies, according to the Fig. 6.10, an increase of ϵ_{reb} and thus of the rebound radius.

Note that in the studies cited here [26, 77, 78, 79] and plotted in Fig.6.10, the non-dimensional parameter ζ is $\ll 7 \cdot 10^{-3}$ (which is the the case with the largest microjet in our experiments). We found respectively $1.5 \cdot 10^{-4}$, $7.5 \cdot 10^{-5}$, $3.0 \cdot 10^{-6}$, and $1.4 \cdot 10^{-4}$. We thus consider that the comparison of our results in microgravity with these data in normal gravity is justified.

6.6.4 Importance of the non-condensable gas

The pressure of the non-condensable gas p_{g0} is the keystone in the understanding of the energy partition at the collapse of a cavitation bubble. A variation of the value of p_{g0} has a direct impact on the energy partition. As an example, we consider a bubble with an initial maximum radius of 5 mm, in a liquid at a uniform pressure 100 kPa, and calculate with our model the evolution of the radius as a function of time for three values of p_{g0}: 1, 10, and 100 Pa. As shown in Fig. 6.16, the maximum radius of the rebound bubble increases with the value of p_{g0}, and the fraction of energy in the rebound ϵ_{reb} is 0.2 %, 1.2 %, and 7.2 % respectively. Quantitative experimental investigation on the effect of the non-condensable gas on the energy partition is very difficult, because there is so far no mean for measuring the value of p_{g0} in the collapsing bubble. However, the effect of the non-condensable gas can be discussed through qualitative experimental observations, or quantitative result issued from theoretical investigations.
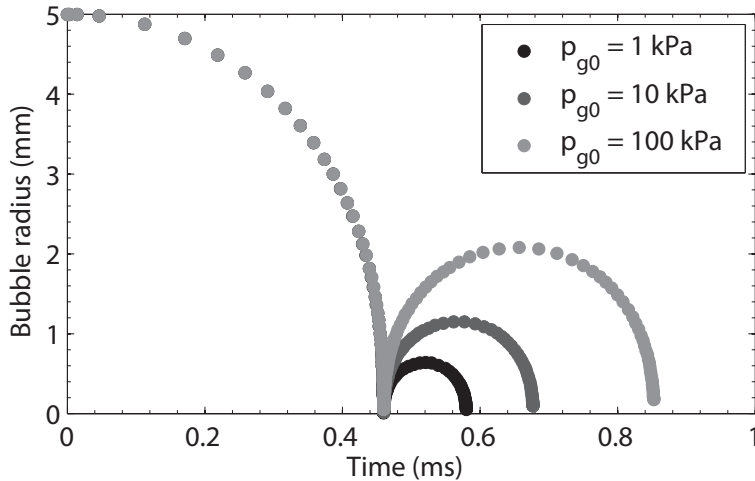
Figure 6.16: Evolution of the radius of the bubble as a function of time, calculated with our theoretical model. The initial radius is 5 mm, and the liquid pressure 100 kPa. The pressure of the non-condensable p_{g0} gas is set to 1, 10 and 100 kPa. The maximum radius of the rebound bubble increases with the value of p_{g0}.

The method for the generation of the bubble plays a major role in the bubble gas content. Indeed, when a bubble is induced with a laser or a spark, non-condensable gas is generated in the initial plasma [80, 26]. The amount of non-condensable gas varies significantly with the generation method. The spark method tends to produce more gas then the laser [27]. Therefore, we understand why the rebound of a spark bubble is larger than the rebound of a laser bubble. In the case of a spark bubble at atmospheric pressure, the energy fraction in the rebound is around $\epsilon_{reb} = 0.31$ [81], whereas in the laser case, we obtained around $\epsilon_{reb} = 0.01$.

After such a discussion on the importance of the non-condensable gas in the bubble, one

can reasonable wonder how can hydrodynamic cavitation bubbles rebound while there is no non-condensable gas generated. The subtlety in the collapse of cavitation bubble is that whether there is non-condensable gas or not in the bubble, vapor is trapped in the bubble at the very last stage of the collapse, and acts like non-condensable gas [57]. The presence of the vapor in the bubble bring another dimension to the problem. Indeed, the vapor pressure p_v varies with the temperature. With a higher temperature of the water, the values of p_v is larger. At the collapse, it would be as if more gas were trapped in the bubble compared to a lower temperature situation, which implies a larger rebound. An experiment has been run, generating bubbles of same size in water at three different temperature. The results, shown in Tab. 6.1, confirm the fact that, for a bubble of a given size at a given pressure in the liquid, the energy fraction in the rebound increases with the temperature. This issue is not treated further here, but still illustrates the complexity of the unresolved problem of the collapse of a cavitation bubble.

Temperature (°C):	4	18	40
R_{max} (mm):	4.2	4.2	4.2
R_{reb} (mm):	0.4	0.8	2.0
ϵ_{reb} (-):	0.1%	0.7%	11.1%

Table 6.1: The values of the maximum radius of the rebound bubble R_{reb}, and the fraction of energy transfered into the rebound ϵ_{reb} are given for the case of a bubble of maximum radius $R_{max} = 4.2$ mm collapsing in a liquid at three different temperatures.

Note that the question of how non-condensable gas affects the energy partition can be inverted. The question would become: What is the value of the non-condensable gas pressure p_{g0} for a given energy partition ? Indeed, similarly to what we did in this chapter, the pressure of non-condensable gas in the bubble can be estimated using the experimental conditions, the observations of the energy partition, namely ϵ_{reb} and ϵ_{SW}, and the theoretical model. This method would be the first method to estimate for experimental observation the pressure of the non-condensable gas inside a bubble. With a better understanding of the gas content at the collapse and the diffusion of gas during the growth and collapse of the bubble, we could imagine being able to determine the amount of non-condensable gas generated at the bubble initiation, and maybe even the concentration of dissolved gas in water. Unfortunately, the lack of understanding of the physics of the very last stage of the collapse still prevent us to develop completely this concept.

6.6.5 Implications of the results

For the first time, a systematic experimental and theoretical investigation of the rebound and shock energy at the collapse of a spherical cavitation bubble is presented. This led us to identify a single non-dimensional parameter ξ, which links the experimental conditions to the fraction of energy in the rebound bubble and in the shock wave. This finding has important

implications for many engineering applications. Indeed, it seems possible to manipulate the bubble dynamics to accomplish the desired task. In microfluidics, cavitation bubbles are used for micro-pumping. The bubble collapses on a solid surface pierce by a channel. The microjet developing at the collapse pushes the water through the channel [23]. The pump flow rate can be optimized by adjusting the size of the rebound and thus of the jet, through the experimental conditions. Conversly, the size of the channel can be optimized for the nominal experimental conditions. In chip cleaning, the intensity of the shock waves and microjets have to be controlled to remove the contaminants without damaging the surface of the chip [20]. The intensity of the shock could be adjusted by changing the pressure in the liquid. In water treatment [21] and other cavitation enhanced chemical reactions [56, 13, 14], the temperature inside the bubble at the collapse is determined by the dynamics of the bubble. It should be thus possible to optimize the processes through the experimental parameters.

The methodology presented here to estimate p_{g0} also opens new perspectives for understanding the origin of the non-condensable gas in the bubble at the collapse. So far the non-condensable gas has been assumed to be a combination of trapped vapor, laser breakdown products, and gas initially present in the water [26]. A method to verify this would be to systematically vary the experimental conditions and assess their effect on p_{g0}. Our model could then be used to extract the values of p_{g0} by fitting the experimental results with the theoretical ones. In the same line of thought, we could imagine estimating water properties, such as the concentration of dissolved gas and nuclei, solely based on observing the rebound of natural or artificially generated cavitation bubbles. Note, however, that such measurements would require a quantitative validation of our model.

7 Conclusions and perspectives

7.1 Conclusions

In this thesis, experiments on the influence of the pressure gradient on the collapse of a cavitation bubble are reported. The first experiment is performed in the cavitation tunnel, where the pressure gradient on the bubble is changing in both the direction and the intensity over the bubble collapse phase, similarly to what can happen in hydraulic machines. A new setup is then built to observe bubbles subject to a constant pressure gradient, whose intensity is varied from one measurement to the other. These experiments allow to develop theoretical models for the prediction of the phenomena occurring at the collapse of the bubble.

A preliminary case study is carried out in a flowing liquid over a Naca0009 hydrofoil in the EPFL High Speed Cavitation Tunnel. A single bubble is generated on demand with a laser focusing technique at various locations on the hydrofoil surface and upstream. The observations reveal a strong influence of the pressure gradient on the bubble collapse. We have shown how the micro jet may develop along the local pressure gradient in stream wise direction and not towards the solid surface as usually observed in still liquids. We have also shown how a cluster of micro bubbles behaves like a single bubble, exhibiting a microjet during its collapse.

To address the case of uniform pressure gradient effects on a single bubble in still liquid, we have developed an appropriate experimental setup where the gravity level may be varied from 0 to 2g. The setup was flown on parabolic flights, offering sequences of microgravity and hyper gravity phases lasting for about 20 s (ESA parabolic flight campaigns). The microgravity obtained during the parabolic flight is further exploited to investigate how the energy in the initial bubble is partitioned between the rebound and the shock at the collapse of perfectly spherical bubbles. To this end, a significant improvement of the optical arrangement in the laser focusing technique was achieved. The focusing lens, traditionally used, was replaced by a parabolic mirror placed in the liquid bulk. The resulting reduction of optical aberration combined with micro gravity conditions led to the generation of the most spherical bubble. The observation of the collapse phase reveals the occurrence of an upward micro jet for normal and hyper gravity induced pressure gradients. In microgravity, a perfectly spherical collapse

was observed. Since the hydrostatic pressure gradient is constant during the collapse, and its intensity is varied between measurements, we were able to develop a universal scaling law predicting the volume of the gravity induced vapor jet as a function of a non-dimensional parameter ζ, which depends on the pressure gradient, the maximum bubble radius and the surrounding pressure. A theoretical development, based on the concept of Kelvin impulse, supports the empirical scaling law.

Finally, we exploited the microgravity phases to investigate how the energy in the initial cavitation bubble is partitioned between the different collapse channels. The problem reduces to the partition between rebound and shock because the luminescence energy is negligible and no jet occurs in microgravity. We have found that most of the energy is transferred into the shock wave. However, the energy transferred in the rebound increases when the pressure in the liquid decreases. Although the gravity is known to affect the microjet and the luminescence, we did not observe a significant effect on the energy partition between rebound and the shock. Therefore, we expect these results to apply also to cavitation bubbles subject to moderate pressure gradient. A physical model for the energy partition is built, relying on a first-order approximation of the liquid compressibility and an adiabatic treatment of the non-condensable gas inside the bubble. This model allowed us to develop a non-dimensional parameter ξ which predicts the partition of the energy between the rebound and the shock wave. The theoretical results were in good agreement with the experimental ones. In both cases we found an increase of the energy in rebound bubble when the pressure in the liquid decreases. The theoretical model highlighted the crucial role of the non-condensable gas in the bubble. The maximum radius of rebound bubble increases with the pressure of the non-condensable gas.

7.2 Perspectives

The contributions presented in this thesis provide new inputs for the understanding of the effect of the pressure gradient on the collapse of a bubble, and insights into future work on the collapse of a bubble. This work could be carried on in three distinct ways: by extending the scaling law to cases of non-constant pressure gradients, by developing further the original approach of energy partition, and by investigating thoroughly the non-condensable gas inside the bubble.

Extension of the scaling law for the jet volume to non-constant pressure gradients

The scaling law for the volume of the jet is obtained in the case of a single bubble in still water, with a constant pressure gradient. The scaling law could be extended to cases of non constant pressure gradients. We could generate the bubble in an axisymmetric venturi tube, where the direction of the pressure gradient on the symmetry line is constant while the intensity varies with the position. We could go back to the case of the bubble around the hydrofoil, where both the direction and the intensity of the pressure gradient vary. If the pressure field for each case can be accurately calculated, we could investigate the dynamic effect of the pressure gradient variation on the collapse of the bubble.

Refinement of the energy partition approach

We present an original approach to investigate the collapse of the bubble, which consists in looking at how the energy in the initial bubble is partitioned between the different collapse channels, namely the rebound, the shock, the jet, and the luminescence. For our experimental conditions, most of the energy goes into the shock (around 80 to 99 %), a little in the rebound (up to 20 %), and a negligible amount in the jet and in the luminescence. Experiments can be carried out to extend the range of validity of the presented theory, by testing different experimental conditions from the ones we used.

The theoretical model could also be improved taking the jet and the luminescence into account. Although the energy involved in jet and luminescence seems negligible, the variation of the partition as a function of the experimental conditions should still be investigated. It would be of particular interest to measure from the luminescence the temperature inside the bubble at the collapse as a function of experimental parameters, such as the temperature and pressure in the liquid, or the gravity level.

The model we propose can be used in different applications including microchip cleaning, microfluidics, or sonochemistry, where the pressure in the liquid could be tuned to optimize the process. In addition, it would be interesting to test the erosion potential of bubbles depending on the energy partition. Bubbles of same potential energy can be generated close to solid boundaries for different conditions. The mass lost by erosion can be compared, and we may be able to identify which phenomenon, either the shock wave or the jet, is the most damaging.

The non-condensable gas

Our model confirms that the non-condensable gas inside the bubble is a key parameter in the collapse of cavitation bubbles. However, the origin of the non-condensable gas is still unclear. It is thought to be a combination of dissolved gas in the water, gas diffusing into the bubble, gas generated at the bubble initiation, and vapor trapped at the collapse. So far, measurements of the pressure of the non-condensable gas, or an analysis of its chemical composition has not proven to be possible. Observations of the rebound of the bubble in various cases could provide a better insight into the problem. One could compare the size of the rebound bubbles when they are generated by different energy deposition methods. Indeed, we already observed that spark bubbles lead to larger rebounds than laser bubbles, but a systematic investigation has not been conducted. We also observed that the rebound is strongly dependant on the temperature of the liquid. Again, a systematic investigation of the thermodynamics of the phenomenon could improve our understanding of the vapor trapped inside the bubble.
A better understanding of the composition of the gas inside the bubble is necessary to obtain reliable and flexible theoretical models to predict the dynamics of the cavitation bubble. With such a model, one could develop a method for estimating the non-condensable gas inside a collapsing bubble by measuring the energy in the rebound and in the shock wave, just as we did in this thesis.

A Appendix

A.1   Numerical simulation of the flow within the cavitation tunnel

The flow in the cavitation tunnel is calculated with a numerical simulation. This allows estimating the pressure at any location in the test section. In particular, we can define streamlines from the bubble generation locations, and extract the pressure, the pressure gradient, and the velocity along a streamline, which leads to the pressure and the pressure gradient experienced by the bubble as a function of time.

The calculation was performed with the commercial code ANSYS-CFX, which uses a finite difference method to solve the Navier-Stokes equations. The geometry is the same as the test section of the cavitation tunnel. We generated a mesh of 127,298 nodes for a 2D calculation. The boundary conditions are the following:

Top, bottom, and hydrofoil:	no slip wall
Sides:	symmetric boundary conditions (i.e. 2D calculation)
Inlet velocity and pressure:	15 m/s and 0.45 bars
Outlet:	average static pressure of 0.45 bars

We defined the fluid as water at a constant temperature of 20°C. The equations are solved with a high resolution advection scheme, and a SST turbulence model. This stationary computation stopped when the maximum residual was below 10^{-7}.

A.2   Verification of the static pressure measurements

A static pressure sensor (Phidget) is located at the exit of the vessel to measure the pressure above the liquid (p_{air}). The pressure sensor is calibrated by the manufacturer for measurements between 20 kPa and 250 kPa. However, during the experiment, we reach pressures below 20 kPa. Therefore, we verify the measurements of the static pressure by comparing with a reference piezo-resistive pressure sensor (Unisensor) of known characteristics. The reference pressure sensor is fixed on the lid of the vessel.

The pressure measured by the static sensor, p_{static}, is plotted as a function of the reference pressure, p_{ref} in Fig. A.1. We observe a non-linearity for pressures p_{ref} below 16 kPa. Therefore, we calculate a regression function to fit the pressure given by the static sensor p_{static} with the one given by the reference sensor p_{ref}. The regression curve is plotted on fig. A.1. :

$$p_{ref} = \frac{p_{static}}{1 + \left(\dfrac{a_1}{p_{static}}\right)^{a_2}} \qquad\qquad a_1 = 115\,\text{mbar}, \qquad \text{and} \qquad a_2 = 11. \qquad\qquad \text{(A.1)}$$

To check whether the static or the reference pressure sensor provides the correct measurement for pressure below 16 kPa, we used the data of the collapsing bubbles collected during the parabolic flight. Indeed, the pressure in the liquid can be derived from the Rayleigh-Plesset equation if the bubble collapse time and the bubble maximum radius is known, see Equ. A.2. The bubble collapse time is equal to the half of the bubble lifetime in the case of spherical collapse. The bubble lifetime can be measured (1) from the high-speed movies and (2) from the reference pressure measurements, where it corresponds to the time between the pressure peaks due to the shock at the generation and at the collapse. The maximum radius of the bubble can be measured on the high speed movies.

$$p_\infty = p_v + \rho \left(\frac{0.915 \quad R_{max}}{\tau_c}\right)^2 \qquad\qquad\qquad \text{(A.2)}$$

where p_∞ is the pressure in the liquid, p_v is the vapor pressure, ρ is the water density, R_{max} is the buble maximum radius, and τ_c is the bubble collapse time.

The pressure in the liquid is calculated with Equ. A.2 for all bubbles in the case of pressure lower than 20 kPa. The mean difference between the pressure calculated from the Rayleigh theory and the pressure given by the static sensor is: 2.75 kPa. The mean difference between the pressure calculated from the Rayleigh theory and the pressure given by the reference sensor is: 0.27 kPa. Therefore, we trust the measurement of the reference pressure sensor, and apply the correction to the measurement of the static pressure sensor.
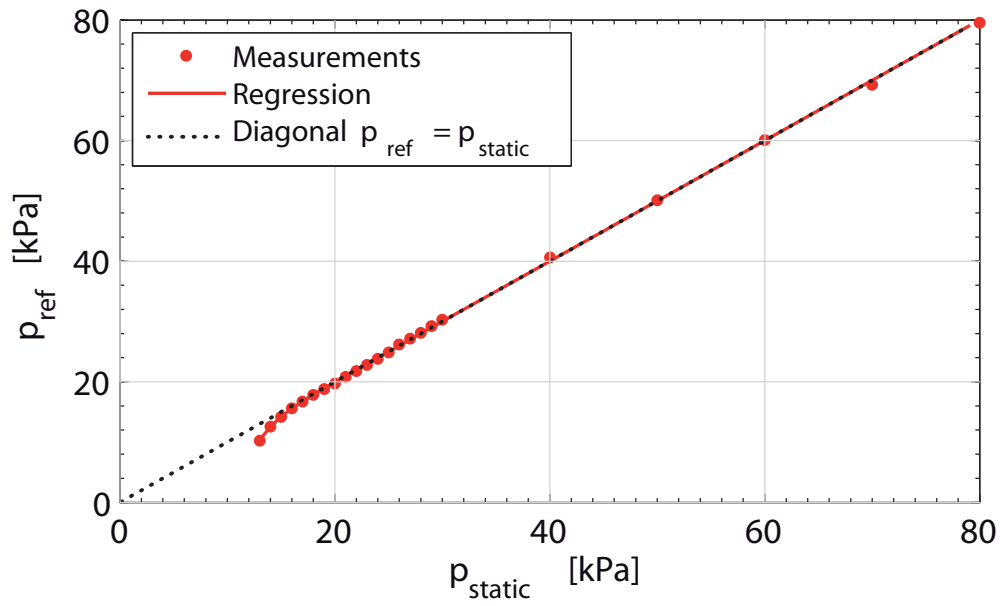
Figure A.1: Calibration of the pressure measured with the static pressure sensor p_{static}, using a reference piezo-resistive pressure sensor p_{ref}.

Bibliography

[1] C. Brennen, *Cavitation and Bubble Dynamics*, vol. 44 of *Oxford engineering science series*. Oxford University Press, New York., 1995.

[2] J. Franc and J. Michel, *Fundamentals of cavitation*, vol. 76. Springer, 2004.

[3] F. Young, *Cavitation.* McGraw-Hill Book Compagny (UK) Limited, 1989.

[4] D. Silverrad, "Propeller erosion," *Engineering*, vol. 33, 1912.

[5] J. Jakobsen and R. Keller Jr, "Liquid rocket engine turbopump inducers," 1971.

[6] T. Graf, H. Fischer, H. Reul, and G. Rau, "Cavitation potential of mechanical heart valve prostheses.," *The International Journal of Artificial Organs*, vol. 14, no. 3, p. 169, 1991.

[7] L. Rayleigh, "On the pressure developed in a liquid during the collapse of a spherical cavity," *Philosophical Magazine*, vol. 34, pp. 94–98, 1917.

[8] M. Plesset, "The dynamics of cavitation bubbles," *Journal of Applied Mechanics*, vol. 16, no. 3, pp. 227–282, 1949.

[9] L. Trilling, "The collapse and rebound of a gas bubble," *Journal of Applied Physics*, vol. 23, no. 1, pp. 14–17, 1952.

[10] J. Keller and I. Kolodner, "Damping of underwater explosion bubble oscillations," *Journal of Applied Physics*, vol. 27, no. 10, pp. 1152–1161, 1956.

[11] J. B. Keller and M. Miksis, "Bubble oscillations of large amplitude," *Journal of the Acoustical Society of America*, vol. 68, no. 2, pp. 628–633, 1980.

[12] A. Prosperetti, "The equation of bubble dynamics in a compressible liquid," *Physics of Fluids*, vol. 30, no. 11, pp. 3626–3628, 1987.

[13] K. Suslick, M. Mdleleni, and J. Ries, "Chemistry induced by hydrodynamic cavitation," *Journal of the American Chemical Society*, vol. 119, no. 39, pp. 9303–9304, 1997.

[14] K. Suslick, Y. Didenko, M. Fang, T. Hyeon, K. Kolbeck, W. McNamara, M. Mdleleni, M. Wong, K. Suslick, Y. Didenko, *et al.*, "Acoustic cavitation and its chemical consequences," *Philosophical Transactions of the Royal Society of London A*, vol. 357, no. 1751, pp. 335–353, 1999.

Bibliography

[15] G. Hauke, D. Fuster, and C. Dopazo, "Dynamics of a single cavitating and reacting bubble," *Physical Review E*, vol. 75, no. 6, 2007.

[16] Q. Wang, K. Yeo, B. Khoo, and K. Lam, "Strong interaction between a buoyancy bubble and a free surface," *Theoretical and Computational Fluid Dynamics*, vol. 8, no. 1, pp. 73–88, 1996.

[17] K. Lim, P. Quinto-Su, E. Klaseboer, B. Khoo, V. Venugopalan, and C.-D. Ohl, "Nonspherical laser-induced cavitation bubbles," *Physical Review E*, vol. 81, no. 1, 2010.

[18] A. Vogel, "Nonlinear absorption: Intraocular microsurgery and laser lithotripsy," *Physics in Medicine and Biology*, vol. 42, no. 5, pp. 895–912, 1997.

[19] B. Gerold, P. Glynne-Jones, C. McDougall, D. McGloin, S. Cochran, A. Melzer, and P. Prentice, "Directed jetting from collapsing cavities exposed to focused ultrasound," *Applied Physics Letters*, vol. 100, no. 2, pp. 024104–024104, 2012.

[20] G. Gale and A. Busnaina, "Removal of particulate contaminants using ultrasonics and megasonics: a review," *Particulate Science and Technology*, vol. 13, no. 3-4, pp. 197–211, 1995.

[21] K. Kalumuck and G. Chahine, "The use of cavitating jets to oxidize organic compounds in water," *Journal of Fluids Engineering*, vol. 122, no. 3, pp. 465–470, 2000.

[22] Z. Yin and A. Prosperetti, "A microfluidic 'blinking bubble' pump," *Journal of Micromechanics and Microengineering*, vol. 15, no. 3, pp. 643–651, 2005.

[23] R. Dijkink and C.-D. Ohl, "Laser-induced cavitation based micropump," *Lab on a Chip - Miniaturisation for Chemistry and Biology*, vol. 8, no. 10, pp. 1676–1681, 2008.

[24] T. B. Benjamin and A. T. Ellis, "The collapse of cavitation bubbles and the pressures thereby produced against solid boundaries," *Philosophical Transactions of the Royal Society A*, vol. 260, pp. 221–240, July 1966.

[25] R. Ivany, *Collapse of a Cavitation Bubble in Viscous, Compressible Liquid - Numerical and Experimental Analyses - Technical Report No. 15*. PhD thesis, Lausanne, 1965.

[26] I. Akhatov *et al.*, "Collapse and rebound of a laser-induced cavitation bubble," *Physics of Fluids*, vol. 13, no. 10, pp. 2805–2819, 2001.

[27] T. Sato, M. Tinguely, M. Oizumi, and M. Farhat, "Evidence for hydrogen generation in laser- or spark-induced cavitation bubbles," *Applied Physics Letters*, vol. 102, no. 7, p. 074105, 2013.

[28] R. Hickling and M. S. Plesset, "Collapse and rebound of a spherical bubble in water," *Physics of Fluids*, vol. 7, no. 1, pp. 7–14, 1964.

[29] M. Tinguely, D. Obreschkow, P. Kobel, N. Dorsaz, A. de Bosset, and M. Farhat, "Energy partition at the collapse of spherical cavitation bubbles," *Physical Review E*, vol. 86, no. 4, p. 046315, 2012.

[30] C. Brennen, "Fission of collapsing cavitation bubbles," *Journal of Fluid Mechanics*, no. 472, pp. 153–166, 2002.

[31] C. F. Delale and M. Tunc, "A bubble fission model for collapsing cavitation bubbles," *Physics of Fluids*, vol. 16, no. 11, pp. 4200–4203, 2004.

[32] Y. Tomita and A. Shima, "High-speed photographic observations of laser-induced cavitation bubbles in water," *Acta Acustica united with Acustica*, vol. 71, no. 3, pp. 161–171, 1990.

[33] O. Lindau and W. Lauterborn, "Cinematographic observation of the collapse and rebound of a laser-produced cavitation bubble near a wall," *Journal of Fluid Mechanics*, vol. 479, pp. 327–348, 2003.

[34] Y. Tomita, P. Robinson, R. Tong, and J. Blake, "Growth and collapse of cavitation bubbles near a curved rigid boundary," *Journal of Fluid Mechanics*, vol. 466, pp. 259–283, 2002.

[35] P. Gregorcic, R. Petkovsek, and J. Mozina, "Investigation of a cavitation bubble between a rigid boundary and a free surface," *Journal of Applied Physics*, vol. 102, no. 9, pp. 094904–094904, 2007.

[36] P. Robinson, J. Blake, T. Kodama, A. Shima, and Y. Tomita, "Interaction of cavitation bubbles with a free surface," *Journal of Applied Physics*, vol. 89, no. 12, pp. 8225–8237, 2001.

[37] D. Obreschkow, P. Kobel, N. Dorsaz, A. de Bosset, C. Nicollier, and M. Farhat, "Cavitation bubble collapse inside liquid spheres in microgravity," *Physical Review Letters*, vol. 97, no. 9, p. 094502, 2006.

[38] E. Robert, J. Lettry, M. Farhat, P. Monkewitz, and F. Avellan, "Cavitation bubble behavior inside a liquid jet," *Physics of Fluids*, vol. 19, no. 6, 2007.

[39] G. Chahine, "Experimental and asymptotic study of nonspherical bubble collapse," *Applied Scientific Research*, vol. 38, no. 1, pp. 187–197, 1982.

[40] E.-A. Brujan, K. Nahen, P. Schmidt, and A. Vogel, "Dynamics of laser-induced cavitation bubbles near an elastic boundary," *Journal of Fluid Mechanics*, vol. 433, pp. 251–281, 2001.

[41] D. Obreschkow, M. Tinguely, N. Dorsaz, P. Kobel, A. de Bosset, and M. Farhat, "Universal scaling law for jets of collapsing bubbles," *Physical Review Letters*, vol. 107, p. 204501, 2011.

Bibliography

[42] J. Dear and J. Field, "A study of the collapse of arrays of cavities," *Journal of Fluid Mechanics*, vol. 190, no. 409, p. 172, 1988.

[43] N. Bourne and J. Field, "Shock-induced collapse of single cavities in liquids," *Journal of Fluid Mechanics*, vol. 244, pp. 225–225, 1992.

[44] D. Obreschkow, N. Dorsaz, P. Kobel, A. de Bosset, M. Tinguely, J. Field, and M. Farhat, "Confined shocks inside isolated liquid volumes: A new path of erosion?," *Physics of Fluids Letters*, vol. 23, no. 10, p. 101702, 2011.

[45] J. Field, J. Camus, M. Tinguely, D. Obreschkow, and M. Farhat, "Cavitation in impacted drops and jets and the effect on erosion damage thresholds," *Wear*, 2012.

[46] A. Vogel, S. Busch, and U. Parlitz, "Shock wave emission and cavitation bubble generation by picosecond and nanosecond ical breakdown in water," *The Journal of the Acoustical Society of America*, vol. 100, no. 1, pp. 148–165, 1996.

[47] C. Ohl, O. Lindau, and W. Lauterborn, "Luminescence from spherically and aspherically collapsing laser induced bubbles," *Physical Review Letters*, vol. 80, no. 2, pp. 393–396, 1998.

[48] T. Matula, "Single-bubble sonoluminescence in microgravity," *Ultrasonics*, vol. 38, no. 1, pp. 559–565, 2000.

[49] C. Ohl, "Probing luminescence from nonspherical bubble collapse," *Physics of fluids*, vol. 14, p. 2700, 2002.

[50] E. Brujan and G. Williams, "Luminescence spectra of laser-induced cavitation bubbles near rigid boundaries," *Physical Review E*, vol. 72, no. 1, p. 016304, 2005.

[51] T. Leighton, M. Farhat, J. Field, and F. Avellan, "Cavitation luminescence from flow over a hydrofoil in a cavitation tunnel," *Journal of Fluid Mechanics*, vol. 480, no. 1, pp. 43–60, 2003.

[52] R. Ivany and H. F. G., "Cavitation bubble collapse in viscous, compressible liquids, numerical analysis," *Journal of Basic Engineering*, vol. 87, pp. 977–985, 1965.

[53] A. Prosperetti and A. Lezzi, "Bubble dynamics in a compressible liquid. part 1. first-order theory.," *Journal of Fluid Mechanics*, vol. 168, pp. 457–478, 1986.

[54] A. Lezzi and A. Prosperetti, "Bubble dynamics in a compressible liquid. part 2. second-order theory," *Journal of Fluid Mechanics*, vol. 185, pp. 289–321, 1987.

[55] J. R. Blake, "The kelvin impulse: application to cavitation bubble dynamics," *The ANZIAM Journal*, vol. 30, no. 02, pp. 127–146, 1988.

[56] K. S. Suslick, "Sonochemistry," *Science*, vol. 247, no. 4949, pp. 1439–1445, 1990.

[57] M. Brenner, S. Hilgenfeldt, and D. Lohse, "Single-bubble sonoluminescence," *Reviews of Modern Physics*, vol. 74, no. 2, pp. 425–484, 2002.

[58] X. Liu, Y. Hou, X. Liu, J. He, J. Lu, and X. Ni, "Oscillation characteristics of a laser-induced cavitation bubble in water at different temperatures," *Optik*, vol. 122, no. 14, pp. 1254–1257, 2011.

[59] C. Brennen, *Hydrodynamics of Pumps.* Oxford University Press., 1994.

[60] I. E. Commission, "Hydraulic turbines, storage pumps and pumps-turbines–model acceptance tests," *International Standard IEC*, vol. 60193, 1999.

[61] F. Guennoun, M. Farhat, Y. Ait Bouziad, F. Avellan, and F. Pereira, "Experimental Investigation of a Particular Traveling Bubble Cavitation," in *Proceedings of the 5th International Symposium on Cavitation CAV2003*, 2003.

[62] M. F. Guennoun. PhD thesis, Lausanne.

[63] S. Ceccio and C. Brennen, "Observations of the dynamics and acoustics of travelling bubble cavitation," *Journal of Fluid Mechanics*, vol. 233, no. 1, pp. 633–660, 1991.

[64] D. Kuhn, S. CHIZELLE, S. Ceccio, and C. Brennen, "Observations and scaling of travelling bubble cavitation," *Journal of Fluid Mechanics*, vol. 293, pp. 99–126, 1995.

[65] F. Avellan, P. Henry, and I. L. Ryhming, "A new high speed cavitation tunnel for cavitation studies in hydraulic machinery. ASME, Boston, December1987," in *Proceedings of International Cavitation Research Facilities and Techniques, ASME Winter Annual Meeting, Boston*, vol. 57, 1987.

[66] P. Ausoni, *Turbulent vortex shedding from a blunt trailing edge hydrofoil.* PhD thesis, STI, Lausanne, 2009.

[67] J. Blake and D. Gibson, "Cavitation bubbles near boundaries," *Annual Review of Fluid Mechanics*, vol. 19, pp. 99–123, 1987.

[68] M. Tsubota, Y. Tomita, A. Shima, and I. Kano, "Dynamics of laser-induced bubble in pressurized liquid nitrogen," *JSME International Journal, Series B: Fluids and Thermal Engineering*, vol. 39, no. 2, pp. 257–263, 1996.

[69] H. Lin, B. Storey, and A. Szeri, "Rayleigh-taylor instability of violently collapsing bubbles," *Physics of Fluids*, vol. 14, no. 8, pp. 2925–2928, 2002.

[70] P. Kobel, D. Obreschkow, N. Dorsaz, A. De Bosset, and M. Farhat, "Techniques for generating centimetric drops in microgravity and application to cavitation studies," *Experiments in Fluids*, vol. 47, pp. 39–48, 2009.

[71] D. Obreschkow, M. Tinguely, N. Dorsaz, P. Kobel, A. de Bosset, and M. Farhat, "The quest for the most spherical bubble - experimental setup and data overview," *Experiments in Fluids*, 2013. Submitted.

[72] A. Vogel *et al.*, "Energy balance of optical breakdown in water at nanosecond to femtosecond time scales," *Applied Physics B: Lasers and Optics*, vol. 68, no. 2, pp. 271–280, 1999.

[73] D. Obreschkow, M. Bruderer, and M. Farhat, "Analytical approximations for the collapse of an empty spherical bubble," *Physical Review E*, vol. 85, no. 6, p. 066303, 2012.

[74] G. Chahine, G. Frederick, C. Lambrecht, G. Harris, and H. Mair, "Spark-generated bubbles as laboratory-scale models of underwater explosions and their use for validation of simulation tools," in *Proceedings of the 66th Shock and Vibration Symposium*, pp. 265–277, Biloxi, MS, 1995.

[75] K. Bader, J. Mobley, C. Church, and D. Gaitan, "The effect of static pressure on the strength of inertial cavitation events," *Journal of the Acoustical Society of America*, vol. 132, no. 4, pp. 2286–2291, 2012.

[76] R. Cole, *Underwater Explosions.* Princeton University Press, 1948.

[77] S. Fujikawa and T. Akamatsu, "Effects of the non-equilibrium condensation of vapour on the pressure wave produced by the collapse of a bubble in a liquid," *Journal of Fluid Mechanics*, vol. 97, no. 3, pp. 481–612, 1980.

[78] D. Kröninger, K. Köhler, T. Kurz, and W. Lauterborn, "Particle tracking velocimetry of the flow field around a collapsing cavitation bubble," *Experiments in Fluids*, vol. 48, pp. 395–408, Sept. 2009.

[79] R. Sadighi-Bonabi, F. Razeghi, H. Ebrahimi, S. Fallahi, and E. Lotfi, "Quasiadiabatic approach for laser-induced single-bubble sonoluminescence," *Physical Review E*, vol. 85, p. 016302, Jan 2012.

[80] J. Blake, Y. Tomita, and R. Tong, "The art, craft and science of modelling jet impact in a collapsing cavitation bubble," *Applied Scientific Research*, vol. 58, pp. 77–90, 1997.

[81] S. Buogo and G. B. Cannelli, "Implosion of an underwater spark-generated bubble and acoustic energy evaluation using the rayleigh model," *The Journal of the Acoustical Society of America*, vol. 111, no. 6, pp. 2594–2600, 2002.

Marc Tinguely

Route de Beaumont 7, 1700 Fribourg, Switzerland
+41 78 883 97 23 / +41 26 424 91 12
marc.tinguely@gmail.com

EDUCATION

2009 – present (expect in 2/12)	**PhD** in Fluid Mechanics The effect of the pressure gradient on the collapse of cavitation bubbles	Ecole Polytechnique Fédérale de Lausanne (EPFL)
2006 – 2009	**Master** in Mechanical Engineering Domains: energy and fluid mechanics	EPFL
2006 - 2007	Including : **Exchange year**	University of Waterloo, Canada
2002 – 2006	**Bachelor** in Mechanical Engineering	EPFL

ACADEMIC EXPERIENCE

2009 – present	PhD Student **Experimental Investigation of the collapse of a cavitation bubble** Design and construction of a compact setup for laser-induced bubble generation in microgravity, used successfully for two ESA parabolic flight campaigns High speed imaging and image processing of the collapse of cavitation bubbles Modeling of the bubble collapse	EPFL - LMH, Lausanne
2007, 2008	Research assistant (2x 2months) **Numerical simulation of pool fire** (under supervision of Dr Cecile Devaud) Testing combustion model with ANSYS CFX Accuracy of parallel computing with FDS/Smokeview	University of Waterloo, Canada

AWARDS

Travel Grant for the 2009 APS DFD conference in Minneapolis, USA
Award for **best presentation** at the EDCM 2010 conference in Lausanne Switzerland

TECHNICAL SKILLS

Experimental: High speed imaging, high energy laser, pressure measurements
Computational: ANSYS CFX (*intermediate*), ANSYS ICEM (*basics*), FDS/Smokeview (*basics*)
Programming: Matlab (*expert*) , Labview (*basics*), C++(*basics*)
CAD: Catia (*intermediate*)
Teaching: supervision of semester projects, supervision of exercises ('Cavitation' course)

LANGUAGE

French	mother tongue
English	fluent (exchange year in Canada)
German	intermediate
Spanish	basics

PEER REVIEWED PUBLICATIONS

Energy partition at the collapse of spherical cavitation bubbles
M. Tinguely, D. Obreschkow, P. Kobel, N. Dorsaz, A. de Bosset, M. Farhat
Physical Review E, 86, 046315, 2012.

Evidence for hydrogen generation in laser- or spark-induced cavitation bubbles
T. Sato, M. Tinguely, M. Oizumi, M. Farhat
Applied Physics Letters, 102 (7), 074105, 2013.

The quest for the most spherical bubble - experimental setup and data overview
D. Obreschkow, M. Tinguely, N. Dorsaz, P. Kobel and A. De Bosset and M. Farhat
Experiments in Fluids, Submitted, 2013

Cavitation in impacted drops and jets and the effect on erosion damage thresholds
J. E. Field, J.-J. Camus, M. Tinguely, D. Obreschkow and M. Farhat
Wear, vol. 290-291, p. 154-160, 2012.

A Universal Scaling Law for Jets of Collapsing Bubbles
D. Obreschkow, M. Tinguely, N. Dorsaz, P. Kobel and A. De Bosset and M. Farhat
Physical Review Letters, 107 (20) 204501, 2011

Confined shocks inside isolated liquid volumes: A new path of erosion?
D. Obreschkow, N. Dorsaz, P. Kobel, A. De Bosset, M. Tinguely, J. E. Field and M. Farhat
Physics of Fluids, vol. 23, num. 10, p. 101702, 2011.